Spring 5-2017

Disorder in Cysteine-Rich Granulin-3 and Its Implication in Alzheimer Disease

Gaurav Ghag
University of Southern Mississippi

DISORDER IN CYSTEINE-RICH GRANULIN-3 AND ITS IMPLICATION IN ALZHEIMER DISEASE

by

Gaurav Ghag

A Dissertation
Submitted to the Graduate School
and the Department of Chemistry and Biochemistry
at The University of Southern Mississippi
in Partial Fulfillment of the Requirements
for the Degree of Doctor of Philosophy

Approved:

_____
Dr. Vijay Rangachari, Committee Chair
Associate Professor, Chemistry and Biochemistry

_____
Dr. Douglas Masterson, Committee Member
Associate Professor, Chemistry and Biochemistry

_____
Dr. Faqing Huang, Committee Member
Professor, Chemistry and Biochemistry

_____
Dr. Sarah E. Morgan, Committee Member
Professor, Polymers and High Performance Materials

_____
Dr. Philip Bates, Committee Member
Assistant Professor, Chemistry and Biochemistry

_____
Dr. Karen S. Coats
Dean of the Graduate School

May 2017

Published by the Graduate School

ABSTRACT

DISORDER IN CYSTEINE-RICH GRANULIN-3 AND

ITS IMPLICATION IN ALZHEIMER DISEASE

by Gaurav Ghag

May 2017

Granulins (GRNs) are a family of small, cysteine-rich proteins that are generated upon proteolytic cleavage of their precursor, progranulin (PGRN) during inflammation. All seven GRNs (1 – 7 or A – G) contain twelve conserved cysteines that form six intramolecular disulfide bonds, rendering this family of proteins unique. GRNs play multiple roles and are involved in a myriad of physiological as well as pathological processes. They are known to a play role in growth and embryonic development, wound healing, and signaling cascades as well as in tumorigenesis. They are also implicated in neurodegenerative diseases like frontotemporal dementia (FTD), Alzheimer disease (AD), and amyotrophic lateral sclerosis (ALS). Despite their manifold functions, there is a paucity in the information about the structure-function relationship of these proteins, especially, with the role of the twelve conserved cysteines and the disulfide linkages in determining their structure and the functions. In this study, the role of disulfide bonds is probed by comparing the structures of the fully reduced GRN-3 (rGRN-3) and native GRN-3. We report that monomeric rGRN-3 is an intrinsically disordered protein (IDP) at low concentrations and undergoes dimerization at higher concentrations to form a fuzzy complex. Interestingly, we show that rGRN-3 is also able to activate NF-κB in human neuroblastoma cells in a concentration-dependent manner. We also show that both *E. coli* and mammalian HEK cells are inefficient in forming correct disulfide linkages and are

incapable of generating monomeric native GRN-3 (GRN-3) exclusively, thus, predominately generating multimeric GRN-3 (mGRN-3) with scrambled inter-molecular bonds. We establish that GRN-3 has a more ordered structure as compared to that of mGRN-3 or rGRN-3, stabilized exclusively by the disulfide bonds which form a fulcrum imparting order to an otherwise disordered protein. We determined the potential involvement of GRN-3 in AD pathogenesis by showing that GRN-3 augments Aβ, the protein implicated in AD, aggregation in a concentration- and time-dependent manner and it interacts both with Aβ monomers and oligomers thereby providing a proof of concept for neuroinflammation triggered neurodegeneration.

ACKNOWLEDGMENTS

I would like to express my deepest and sincerest gratitude to my mentor, Dr. Vijay Rangachari or as he likes us to call him, Vijay. He has taught me several valuable lessons not only in science but also in life. I admire his enthusiasm for research and his zest to simply figuring out problems. As I embark on future endeavors, the most important lesson that I will carry forward is this passion for science and discovering things. I would like to thank him for his constant motivation, for believing in me and most importantly being patient with me.

I would also like to thank my committee members, Dr. Douglas Masterson, Dr. Faqing Huang, Dr. Sarah Morgan, and Dr. Philip Bates for their advice, suggestions, and guidance throughout my Ph.D. tenure.

I am very grateful to all my co-workers, current and past, especially, Dexter Dean and Amit Kumar. Both Dexter and Amit have been very helpful and fun to be with in the lab and more importantly outside lab, especially during happy hours. I would also like to thank Anukool Bhopatkar for carrying forward this project so I can be set free, and of course for being a good friend and a caring roommate. I would like to specially thank Kelly Hill and Randi Reed for being a major part of this project and most importantly for tolerating me, especially, Kelly who has been a constant source of fun in the lab and one of my best friends. I would also like to thank Chris Mullins, Ryan Campbell, Wisam Beauti, and Sam Gearhart.

I would like to thank Lauren Wolf and Dr. Mellisa Moss from Univ. of South Carolina for the amazing collaboration. I would also like to thank Cassandra Bates from Dr. Heinhorst's lab for providing me chemicals and other lab essential whenever I needed

them. I would like to thank Mrs. Tina Masterson who was an excellent teaching coordinator and very helpful during my teaching assistantship and to Ms. Sharon King for being extremely helpful all the time.

I would like to thank all my friends and family for their support and love and some of very wonderful memories.

DEDICATION

"To whom I owe the leaping delight" – T.S. Elliot.

I would like to dedicate this dissertation to my beautiful and loving wife, Jaspreet Kaur Jaggi. Without her support, motivation, understanding and somewhat intimidation, I wouldn't have been able to get here. Thank you, Jaspreet, for your endless, patient and sometimes impatient love.

TABLE OF CONTENTS

LIST OF ILLUSTRATIONS

LIST OF ABBREVIATIONS

AD	Alzheimer Disease
FTD	Frontotemporal Dementia
GRNs	Granulins
PGRN	Progranulin
TFE	Trifluoroethanol
TMAO	Triamethyl N-amine oxide
SDS	Sodium Dodecyl Dulfate
ANS	8-Anilino-1-Naphthalene Sulfonate
IDP	Intrinsically Disordered Protein
IUP	Intrinsically Unstructured Protein
Aβ	Amyloid-β
APP	Amyloid Precursor Protein
AUC	Analytical Ultracentrifugation
CD	Circular Dichroism
PBS	Phosphate Buffered Saline
Tris	Tris-(hydroxymethyl)-aminomethane base
PAGE	Polyacrylamide Gel Electrophoresis\
SEC	Size Exclusion Chromatography
rHPLC	Reverse Phase High Pressure Liquid Chromatography
ThT	Thioflavin-T
IAM	Iodoacetamide

CHAPTER I - INTRODUCTION

1.1 Alzheimer Disease

1.1.1 Overview – Biochemistry and Physiology

Alzheimer disease (AD), the most common and widely spread form of dementia, is a multifactorial neurodegenerative disorder characterized by the progressive impairment of memory, loss of cognition, altered behavior, and loss of social appropriateness[1] As per the Alzheimer association's 2016 report, an estimated of 5.4 million Americans of all ages have AD and it is the fifth leading cause of death in the nation. The pathology primarily arises due to the progressive neuronal death in the cortical and hippocampal regions of the brains, which are triggered by two hallmark lesions called the extracellular neuritic plaques composed primarily of a protein called amyloid-β (Aβ), and intracellular neurofibrillary tangles (NFTs) composed primarily of hyperphosphorylated tau[1-4] Both neuritic plaques and the neurofibrillary tangles are responsible for the death of the neurons, Aβ aggregates that form the major part of neuritic plaques are considered the prime neurotoxic agents in AD[5] Aβ peptides are generated by a sequential proteolysis of an ubiquitously expressed, transmembrane precursor protein called β-amyloid precursor protein (β-APP/APP) by aspartyl proteases β- and γ-secretases[6] γ-secretase can cleave APP at multiple positions generating several forms of Aβ ranging from 39 to 43 amino acids of which Aβ40 and Aβ42 are predominant and more prone to aggregation[7] Aβ is an intrinsically disordered protein (IDP) and lacks a well-defined 3D structure in its monomeric state[8] Like most IDPs, Aβ has an intrinsic propensity to aggregate into high-molecular-weight, filamentous fibrils, which deposit as senile plaques[8, 9] The process of aggregation is nucleation-dependent

and displays a classic sigmoidal growth curve with an initial lag phase, followed by rapid growth forming soluble low molecular weight oligomers which aggregate further forming the soluble high molecular weight protofibrils which undergo the processes elongation and lateral association to eventually form fibrils with cross β-sheet structure (Figure 1.1)[10-12]

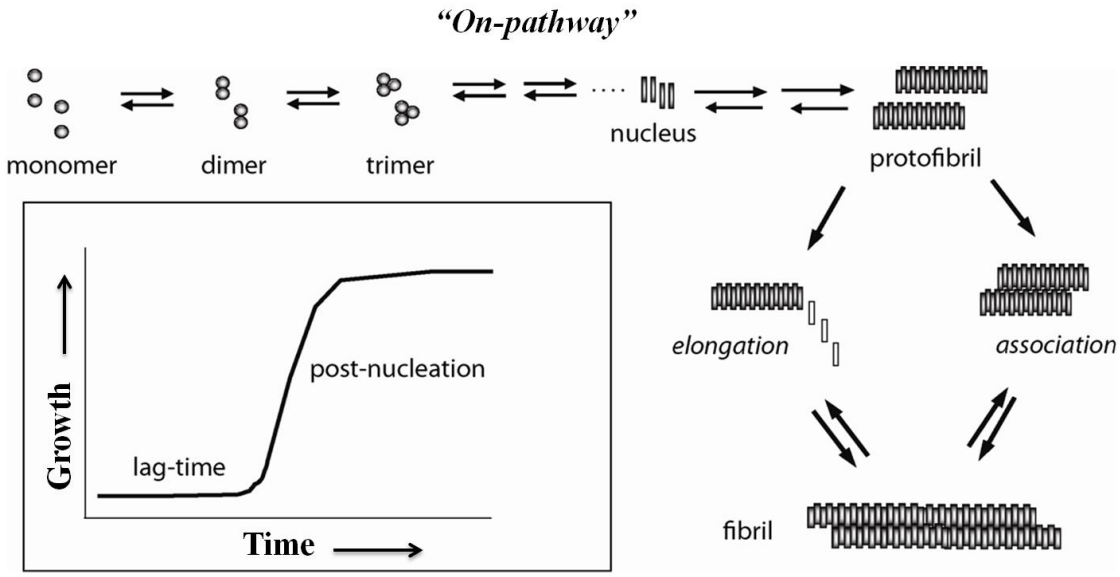

Figure 1.1 Schematic representation of Aβ aggregation.

Different species formed along the pathway. (Inset): Sigmoidal curve showing the lag-time and post-nucleation stages of aggregation.

Though based on the classical amyloid hypothesis, fibrils are considered primarily responsible for the neuronal death, cognitive decline and memory impairment has been shown to occur even in the early stages of AD before the deposition of amyloid plaques.[13-17] Thus, it has been shown that the low molecular weight soluble oligomers ranging from ~2 to 60mers are the primary neurotoxic species responsible for cognitive decline during early stages of AD.[14, 18] Consequently, several low molecular weight oligomers have been identified *in vivo* as well as *in vitro* as the perpetrators of AD pathology.[10, 19] Due to their increased significance in disease pathology, characterization

of structure-function relationships of these low molecular weight soluble oligomers is warranted to discern their precise role in disease progression. However, it is difficult to isolate and generate *in vivo* oligomers from physiological samples in adequate amounts to characterize them biophysically. Thus, considerable focus has been on generating and isolating exogenous oligomers that mimic the physiological ones.[20-22] Recently, our lab has generated and isolated *in vitro* oligomers called LFAOs (large fatty acid derived oligomers) in the presence of fatty acid interfaces.[23] LFAOs have been shown to undergo unique self-propagative replication by quantitatively converting more monomers into similar toxic oligomers.[24, 25] Moreover, these LFAOs (12-24mers) undergo prototypical prion-like propagation to form LFAO strain-specific fibrils via a three-step mechanism.[26]

1.1.2 Neuroinflammation as One of the Perpetrators of AD

Most cases of AD are idiopathic while some are familial and can be attributed to the rare autosomal dominant mutations in the genes for APP and presenilin (protein involved in processing of APP to Aβ).[27] However, the precise etiology of the disease is unknown and the complex nature of the disease makes it difficult to point out any single perpetrator of the disease. One of the predominant events that is observed in AD brains is the chronic activation of the innate immune responses and neuroinflammatory cascades.[28, 29] Deposition of Aβ plaques as well the soluble toxic oligomers of Aβ have been shown to activate microglia and astrocytes in the affected brains leading to the release of an array of proinflammatory neurotoxins like cytokines like tumor necrosis factor (TNF)-α, interleukin (IL)-6, interferon (IFN)-γ, etc., chemokines, reactive oxygen and nitrogen species, complement proteins and other proinflammatory proteins, and several proteolytic enzymes.[30, 31] In contrast, the activation of microglia upon an

inflammatory event is the key defense mechanism of the innate immune system of the brain[32], and activated microglia also facilitate in clearing the amyloid plaque load via endocytosis.[33-35] However, chronic activation of these microglial cells in AD causes them to get arrested in proinflammatory state thus impeding their neuroprotective phagocytic role.[36] Thus, neuroinflammation is one of the important drivers of the disease progression exacerbating neuronal loss. However, activation of inflammatory pathways before or during the disease onset may also account for as the cause of the disease. In this respect, few evidences corroborate the causative role of inflammation. Biochemical investigation and immunohistochemical studies have shown surge in the release of cytokines like IL-1, IL-6, and TNFα and other inflammatory proteins at the onset of AD[37], and clinical investigations have shown that individuals with prolonged use of non-steroidal anti-inflammatory drugs (NSAIDs) are at reduced risk of developing AD.[38, 39] Moreover, inflammation triggered by external factors like a traumatic brain injury such chronic concussions during contact sports or in war veterans, severe viral infections of the CNS, metabolic stress associated with other disease like diabetes, or even severe emotional stress due to life altering events also increase the risk of developing late-onset AD.[40-43]

The arrest of microglia in the proinflammatory diseased state and the studies that show dysfunctional clearance of amyloid plaques by diseased microglia[34, 44] warrant the systematic investigation of the molecular processes that occur as the downstream effect of such a condition and their role in the disease onset as well as progression, specifically, with respect to myriads of proinflammatory mediators released from activated microglia and their interaction with Aβ. It is well-documented that the chemically-activated microglia secrete several proinflammatory mediators that stimulate APP production and

its processing to Aβ peptides.[45, 46] Thus, these proinflammatory mediators could play a crucial role in the onset as well as the progression of AD by directly interacting with Aβ thereby modulating its aggregation leading to the formation of toxic aggregates/oligomers. These Aβ aggregates can, in turn, further activate more microglial cells causing release of more proinflammatory mediators thereby drastically increasing their local concentrations in CNS. This will further exacerbate the diseased state leading to a self-perpetuating and self-amplifying cyclical pathway as depicted schematically in Figure 1.2.

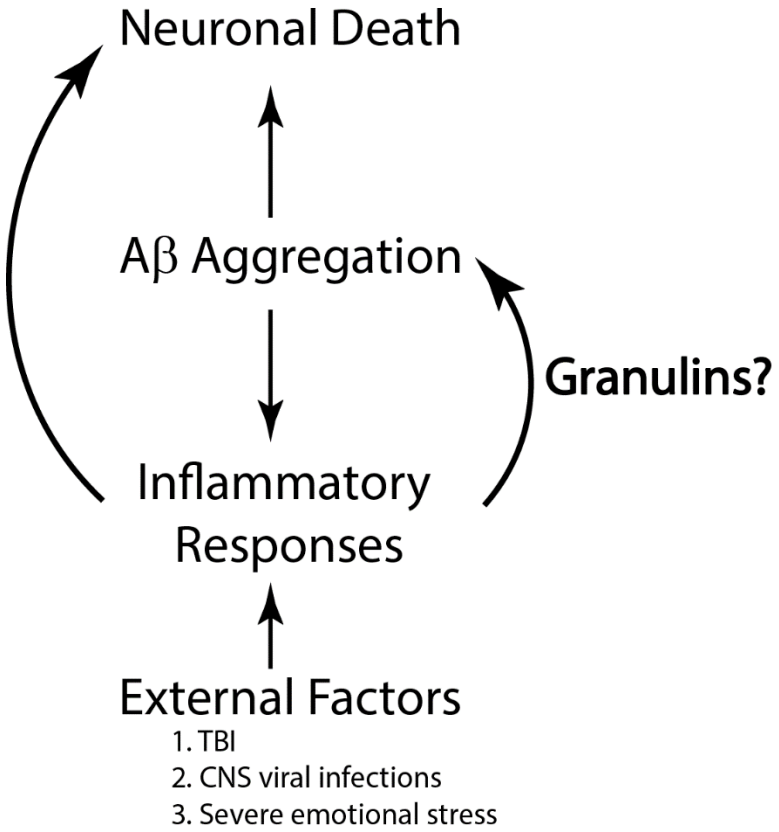

Figure 1.2 Role of neuroinflammation triggered by TBI in AD pathogenesis

Of all the proinflammatory mediators implicated in AD onset, this research focuses on a family of unique proinflammatory proteins called Granulins, specifically

Granulin-B. These proteins have been already implicated in other neurodegenerative diseases like frontotemporal dementia (FTD), and amyotrophic lateral sclerosis (ALS) as well in AD. The ensuing sections detail the structure-function relationship of Granulins, specifically, Granulin 3 also referred as Granulin-B and elaborate their implications in AD and other neurodegenerative diseases.

1.2 Progranulin and Granulins – Overview

1.2.1 Progranulin

Progranulin (PGRN) or granulin-epithelin precursor, proepithelin, PC-cell derived growth factor, and acrogranulin is a 68.5 kDa secretory growth factor with pleiotropic roles in physiological as well as pathological processes.[47-51] The gene for PGRN is located on chromosome 17q21.32 in humans[52] and chromosome 11 in mouse.[53] PGRN is highly conserved in plants, insects, worms, fish, and mammals including humans.[54-57] Moreover, PGRN is expressed ubiquitously throughout the human body including the epithelial cells of intestinal crypt, skin, and reproductive organs[58, 59], immune system organs like spleen and lymph nodes and in the innate immune system cells[59], and in central nervous system both in the neurons and the neuroinflammatory cells like microglia.[60-62] The expression of PGRN is well distributed in the neurons in the different regions like the neocortex, hippocampus, Purkinje cells of the cerebellum, and in the motor neurons.[59-62] However, more recently the augmented secretion of PGRN from the microglial cells activated due to an external or internal traumatic injury or insult to the brain have come to bear significance with respect to the neuroinflammatory role of PGRN and GRNs in neurodegenerative diseases like Alzheimer disease and Parkinson's disease.[63] In this context, several reports have shown an increased secretion of PGRNs

and GRNs from the activated microglia in mouse models of spinal cord injury[64, 65], traumatic brain injury[66], Alzheimer disease[63], and multiple sclerosis.[67]

PGRN is a heavily glycosylated protein[68] with 593 amino acids and consists of seven and a half tandem repeats of cysteine-rich motifs (1 – 7 and P) called Granulins (GRNs) or Epithelins (Figure 1.3).[47, 49, 52, 69, 70] Each of the seven GRN motifs consists of twelve conserved cysteines that form six intra-molecular disulfide bonds as indicated for GRN-3 in Figure 1.3.[71] The GRN motifs are released by the proteolytic digestion of PGRN by an array of proteases like neutrophil elastase[72], proteinase 3 (a neutrophil protease)[73], MMP-12 (matrix metalloproteinase 12; macrophage elastase)[74], MMP-14[75], and ADAMTS-7 (a disintegrin and metalloproteinase with thrombospondin motifs)[76] during an inflammatory event by cleaving in the linker regions between the GRN domains.[72] The cleavage sites have been mapped for all the GRNs to the linker regions except for GRNs 2, 3, and 4.[72]

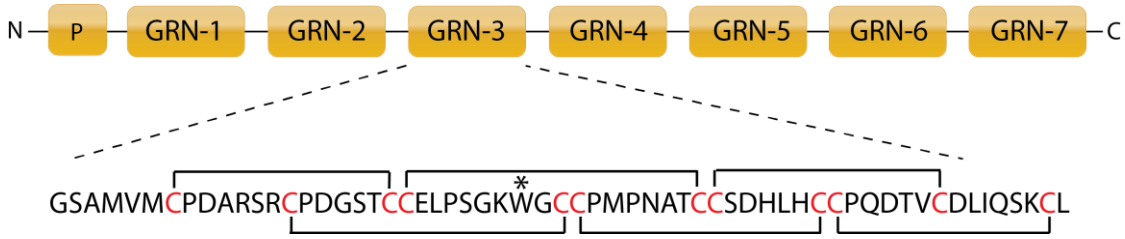

Figure 1.3 The domain structure of PGRN.

The numbers/letters in the boxes represent the granulins (1 – 7 or A – G & P) and amino acid sequence of GRN-3 is shown below with conserved cysteines in red and putative disulfide bonds.[77] The scissors represent the sites at which the proteases cleave PGRN, asterisk represents that the sites have not been identified yet.

1.2.2 Granulins

Granulins (GRNs) or epithelins were first isolated from the human inflammatory cells extracts and from the rat bone marrow.[69] Initially, individual GRNs were isolated

from several sources and molecular cloning and northern blot analysis showed that the GRNs were expressed as a precursor protein called PGRN by a single gene.[49] Four of the seven GRNs, GRNs A or 4, B or 3, C or 5, and D or 6 were isolated from the human leukocyte granule extract[69], whereas the fifth GRN, GRN-F or 2 was isolated from urine.[78] All seven GRNs (GRNs 1 – 7) are about ~6 kDa in size and all, but GRN-1 or GRN-G, are characterized by presence of twelve conserved cysteines; four pairs towards the center of the protein flanked by two single cysteines at both N- and C-termini; GRN-1 has only 10 conserved cysteines.[49, 52] These cysteines from six intra-molecular disulfide bonds with a putative interlocking pattern depicted in Figure 1.3. Microsequencing of full-length human and rat GRN-4 (GRN-A), purified from bone marrow extracts, confirmed that the two proteins are highly homologous as well as partial N-terminal sequencing of GRNs 3 (GRN-B), 5 (GRN-C), and 6 (GRN-D) confirmed that they are closely related to human GRN-4.[79] In fact, the sequence comparison of all seven GRNs from humans reveals 37 – 60% homology as depicted in Figure 1.4. Perhaps, the evolutionarily conserved cysteines residues among all the GRNs play a significant role in determining the structure and function of the proteins.

```
GRN-1 MGGPC-QVDAHCSAGHSCIFTVSGTSSCCPFPEAVACGDGHHCCPRGFHCSADGRSCF
GRN-2 MAIQCPDSQFECPDFSTCCVMVDGSWGCCPMPQASCCEDRVHCCPHGAFCDLVHTRCI
GRN-3 -MVMCPDARSRCPDGSTCCELPSGKYGCCPMPNATCCSDHLHCCPQDTVCDLIQSKCL
GRN-4 MDVKC-DMEVSCPDGYTCCRLQSGAWGCCPFTQAVCCEDHIHCCPAGFTCDTQKGTCE
GRN-5 -MVPC-DNVSSCPSSDTCCQLTSGEWGCCPIPEAVCCSDHQHCCPQGYTCVAE-GQCQ
GRN-6 -MIGC-DQHTSCPVGQTCCPSLGGSWACCQLPHAVCCEDRQHCCPAGYTCNVKARSCE
GRN-7 MDVEC-GEGHFCHDNQTCCRDNRQGWACCPYRQGVCCADRRHCCPAGFRCAARGTKCL
      ....C.D....CP...TCC....G.W.CCP....VCC.D..HCCP.G..C......C.
```

Figure 1.4 The sequence alignment of human GRNs.

The conserved amino acid residues are highlighted and the sequence in the box is the consensus sequence. Dashes have been introduced to align the cysteines.

1.3 Structure and Functions of Progranulin and Granulins

1.3.1 Progranulin

Most of the research in the past has been focused on understanding the functions of PGRN but not much is known about the structure of PGRN except for its domain architecture, which is depicted in Figure 1.3 and elaborated in section *1.2.1*. The functions of PGRN can be categorized as growth-factor-like activities, immune modulation, and neurotrophic effects. Additionally, PGRN has been implicated in the progression of tumor in the brain as well as in the periphery[80] and has been implicated in neurodegenerative diseases like Frontotemporal Dementia (FTD), Alzheimer Disease (AD), Parkinson's Disease (PD), and Amyotrophic Lateral Sclerosis (ALS).[81] The detailed role of PGRN and GRNs in neurodegenerative diseases like FTD and AD will be discussed later (see section *1.4*). The growth-factor-like activities of PGRN are manifested as early as during embryonic development; PGRN has been detected in both male and female reproductive cells.[59, 82, 83] A glycoprotein called acrogranulin present in the acrosomes of guinea pig sperms has been found to be guinea pig equivalent of PGRN based on structural characterization.[47, 84] The expression of PGRN is highest in the trophectodermal cells of the blastocysts[84], which form the fetal compartment of the placenta. They are the first lineage that are committed to become epithelial cell line reiterating the growth-factor-like role played by PGRN in epithelia. Needless to say, PGRN is a growth-factor for trophectodermal cells promoting cavitation and blastocoel expansion, indispensable steps during development of the zygote.[82] Moreover, post-implantation expression of PGRN has been shown to be critical for the prenatal sexual differentiation of the rat brains[85], thus reinforcing the trophic role of PGRN in CNS as

early as during embryonic development. The trophic effects of PGRN in neurons are characterized by their ability to promote survival of cortical and motor neurons[86] and neurite outgrowth[87], in culture. Additionally, PGRN functions as chemoattractant for microglia and stimulate the endocytosis of Aβ peptides implicated in Alzheimer disease[88] and also protects the brain against deposition of Aβ peptides.[89]

The role of PGRN in tissue repair and inflammation, both in periphery and in the brain, is complex. After an injury, human and murine skin show an elevated expression of PGRN in wound fibroblasts and endothelial cells which remained elevated above the baseline for at least 10 days after the injury.[90] Several inflammatory cells expressed PGRN at higher levels as they get wounded.[90] Extraneous application of PGRN to cutaneous wounds in rats has shown to increase the accumulation of blood vessels and fibroblasts in the wound.[90] More significantly, increasing evidence implicate a critical role of PGRN in neuroinflammation. As stated before, PGRN is mainly expressed in activated microglia[62] in response to trauma such as spinal cord injury[65] or axotomy.[60] Moreover, the elevated expression of PGRN is observed in activated microglia in FTD and AD.[63] PGRN is known to bind to the receptors for the tumor necrosis factor α (TNF-α)[91] and inhibit the downstream TNF-α signal transduction.[72] PGRN also inhibits the ability of TNF-α to promote spreading and degranulation of neutrophils and their respiratory bursts.[72, 73] Thus, PGRN is known to have anti-inflammatory activities. This activity is enhanced in the presence of secretory leukocyte protease inhibitor (SLPI) which functions to protect the proteolysis of PGRN into individual GRN peptides by serine proteases.[72] This is significant as activated microglia that secrete PGRN, also secrete the several proteases that cleave PGRN and without the SLPI protein, PGRN is

prone to get cleaved into GRN peptides that, interestingly, have opposite activities as detailed in the next section (see *1.3.2*).[72] Thus, in an inflamed environment, the ratio of intact anti-inflammatory PGRN to the proinflammatory GRN peptides is determined by the ratio of SLPI and elastases which could play a critical role in determining the role of PGRN/GRNs in neuroinflammatory pathways involved in neurodegenerative diseases.

1.3.2 Granulins

Even though there is not much sequence homology between GRNs and other growth factors, similarities between the tertiary structure of mammalian GRNs and that of epithelial cell-specific transforming growth factor (TGFe) are quite striking.[79] Additionally, GRNs have structural subdomains that closely resemble – 1) the cysteine-rich epidermal growth factor (EGF) like domains, that contain six cysteines that form three disulfide bonds, present in epidermal growth factor (EGF), and transforming growth factor-α (TGFα; Figure 1.5A).[92-94], and the kringle domains, which are disordered domains stabilized by six disulfide bonds, present in several proteins like the hepatocyte growth factor[95, 96], proteases involved in blood clotting such as prothrombin, and plasminogen[97], apolipoprotein[98], and tissue plasminogen activator[99]. The secondary structure of carp-GRN 1 (cGRN1) and human GRNs 4, 5, and 2 has been solved using 2D-NMR.[71, 100] The 2D-NMR structure of cGRN1 revealed a unique structure of 4 stacked β-hairpins stabilized by six intra-hairpins (intra-molecular) disulfide bonds with the peptide backbone forming a left-handed helix giving an overall twisted ladder-like structure (Figure 1.5B). Similarly, there of the seven human GRNs, GRNs 4, 5, and 2 were shown to form the N-terminal stack of β-hairpins with the cross-linked disulfide bonds as observed for the N-terminal region of cGRN1.[71, 100, 101] Out of the two N-

terminal β-hairpins, the second was found to be most stable as a single amino acid substitutions did not alter its stability.[100] The C-terminal domain, on the contrary, was found to be disordered.[100]

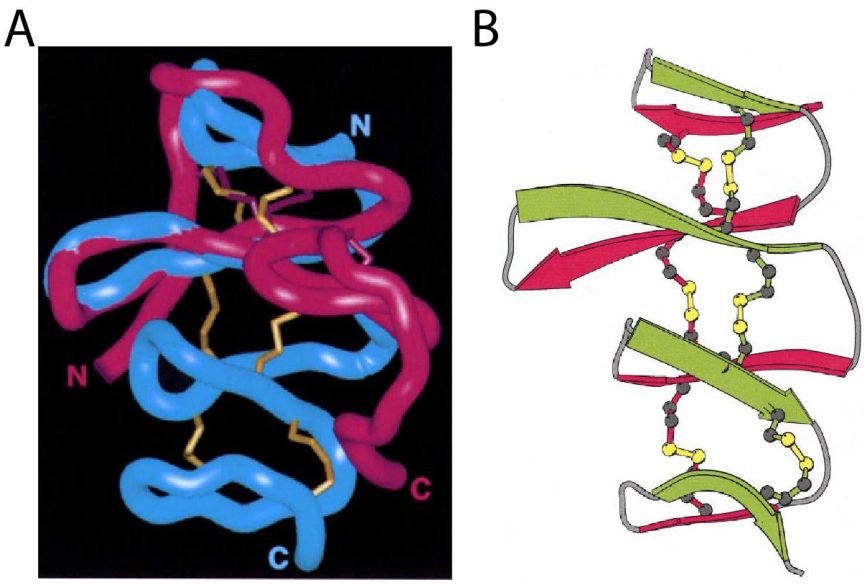

Figure 1.5 Structural domain comparison of GRN-4.

A, Comparison of Grn domain and murine EGF domain showing the structural overlap; B, The MOLSCRIPT representation of the cGrn1 structure showing the unique fold with four stacked β-hairpins connected by six disulfide bonds.[71]

In fact, only 28 of the 57 residues of cGRN1 were found to be part of the β-hairpins fold, whereas the rest of the residues were unstructured[71] and this analysis can be extended to human GRNs as well as only N-terminal was shown to have well-defined structure. The structure of the rest of the human GRNs could not be elucidated as they were either a heterogeneous mixture of several disulfide bond isoforms or completely lacked structure.[100] For instance, purified GRN6 consisted of two molecular species and yielded confusing NMR spectra, whereas GRN-3, GRN-7, and GRN-1 completely lacked any structure.[100] Furthermore, it is not known if GRN-3 and GRN-7 attained any stable structure within PGRN.[100] Thus, though the N-terminal domain of human GRN4, 5, and 2

was found to be similar to that of cGRN1, all having a well-defined stacked β-hairpin structure, there is still ambiguity about the structure of other GRNs, and so is the uncertainty about the disulfide pairing.[100] It is noteworthy that several hydrophobic and turn stabilizing amino acid residues present in cGRN1 are absent in human GRNs, which could contribute to the plasticity and disorderness observed among the latter.[100, 102]

Nevertheless, human GRNs have been implicated in several physiological and pathological processes although it remains uncertain if these multiple functions are mediated by individual GRNs or PGRN or both. The lack of clear knowledge about the functions of GRNs has been exacerbated by the difficulty in obtaining the proteins in homogenous forms *in vitro* due to the difficulty posed by the high degree of disulfide bonds in the protein. Despite these difficulties, some studies have revealed important roles human GRNs take part in. GRN-6 was shown to be mitogenic for glioma cells, although its structure was only partially characterized.[103] GRN-3 was found to inhibit the growth and proliferation of epithelial cells lines, A549 and SW-13 while inducing excessive amount of interleukine-8 (IL-8) secretion[72] Both GRN-4 and GRN-3 could not inhibit the TNFα induced respiratory burst and the release of proteinases by neutrophils.[72] These studies establish that GRN-3 is proinflammatory, which and implicate a proinflammatory nature of GRN-4.

1.4 Implications in Neurodegenerative Disorders

1.4.1 PGRN and GRNs in AD

As mentioned in section *1.1.2*, mediators released by activated microglia arrested in the diseased proinflammatory state may play a crucial role in the onset and the progression of AD pathology. Cytokines have been shown to overexpress in AD and are

known to trigger plaque formation and neuronal degradation.[104] PGRNs and GRNs could play a critical role in this regard by directly interaction with Aβ and triggering its aggregation. PGRNs and GRNs been implicated in other neurodegenerative diseases like FTD (detailed in section *1.4.2*) and ALS. Indeed, several polymorphisms of *PGRN* have been linked to sporadic AD and haplotypes have been identified that contribute to the increased risk of AD.[105, 106] PGRN and GRNs have also found to colocalize with Aβ plaques at postmortem examinations of brains of the patients with AD.[88] In another study, similar results were observed in a transgenic mouse model of AD.[107] Moreover, the activated microglial cells that are associated with the Aβ plaques[63] over-express PGRN as well as the proteolytic enzymes that cleave PGRN into proinflammatory GRNs.[108] This increased expression in microglia may play a pivotal role in the response to brain injury, neuroinflammation, and neurodegeneration. Though PGRN is anti-inflammatory and has neuroprotective role, the precise roles of the proinflammatory GRNs remain elusive.

1.4.2 Involvement in Frontotemporal Dementia (FTD)

Frontotemporal dementia is the second most common form of presenile dementia after AD and accounts for 5-10 % of all dementia.[109] The clinical manifestations in FTD include abnormalities of personality, behavior and/or prominent language impairment, such as progressive non-fluent aphasia or semantic dementia.[110] Certain severe patients also exhibit traits of Parkinson's disease or motor neuron disease (MND).[111] FTD involves prominent neuronal loss and atrophy of the frontal and temporal lobes.[109] The pathology of the disease varies with few cases showing hyperphosphorylated tau and α-synuclein (α-syn) positive aggregates in neurons and gliomas[112], whereas a majority of cases of FTD show neuritis or neuronal cytoplasmic inclusions (NCI) in superficial layers

of the neocortex and hippocampus that are immunoreactive for ubiquitin but not for tau or α-syn.[113, 114] Interestingly, FTD patients show familial inheritance in 20-50% cases and the most common pattern of inheritance is autosomal dominant.[115-117] Mutations in *PGRN*, located on chromosome 17q21 in humans resulting in null alleles, were shown to be one of the main causes of familial form of FTD[81] with a frequency of 5-10% among all familial cases.[87, 118] The pathology in these cases include the accumulation of ubiquitinated TDP-43 (Tar DNA binding protein) aggregates in the frontal and temporal cortices[81, 119, 120]. These null mutations in *PGRN* result in the premature transcription termination and formation of immature mRNAs, which get degraded by the process of nonsense-mediated decay (NMD).[81] This results in a condition called haploinsufficiency resulting in lower than normal level of PGRN in CSF, blood, and in unaffected regions of the brain.[121-124] However, the exact molecular mechanisms that link haploinsufficiency of PGRN to ubiquitin-positive TDP-43 inclusions in FTD are not known. Interestingly, TDP-43 accumulation is also seen in other neurodegenerative diseases like non-*PGRN* FTD, ALS, and AD.[125] In addition to the null mutations that lead to haploinsufficiency of PGRN, a few missense mutations, mapped to be present in GRN-3 sequence of *PGRN*, have also been implicated in FTD[126, 127]. However, if these mutations alter the structure of GRN-3 and/or PGRN is not known but molecular modeling studies have indicated that the P43L mutation in the GRN-3 sequence can have a destabilizing effect on the putative β-hairpin structure of GRN-3.[126] The discovery of the mutations in the *PGRN* involved in FTD and its loss of function thereof led to the hypothesis that restoring the normal levels of PGRN could serve as an excellent therapeutic strategy. Indeed, several studies have shown that the effects of PGRN deficiency could be rescued by heterologous expression

of PGRN.[87, 128, 129] This corroborates the proposed theory that restoring PGRN expression could reverse the effects caused by its deficiency and serve as a potential therapy in FTD.

1.5 Rationale for the Study

One of the remarkable characteristics of PGRN and its cleaved peptides, GRNs, is that they are involved in multiple biological processes. As elaborated in the previous sections (see sections *1.2 and 1.3*), both PGRN and GRNs play crucial roles in plethora of physiological as well as pathological functions. Addition to this list is their role in tumorigenesis and cancer development.[90] However, even though PGRN and/or GRNs are involved in myriads of processes, the overarching question about the precise roles played by the precursor protein, PGRN and those by the peptide products, GRNs, especially in central nervous system (CNS) is still unanswered. Clearly, PGRN and GRNs have opposite cellular activities: while PGRN is known to be anti-inflammatory and has been shown to be neuroprotective and support neuronal growth[86, 87], GRNs are predicted to be proinflammatory, especially GRN-3.[72]

Several clinical evidences point towards critical roles of GRNs in AD (detailed in section *1.4.1*). However, the underlying reasons for the multifunctional roles of GRNs are not known. However, one could explain the reason for multifunctional roles by the potential structural plasticity that will allow GRNs to interact with multiple partners culminating in numerous biological activities. Such a plasticity is a well-known trait of intrinsically disordered proteins (IDPs), which lack a well-defined 3D structure in their native state, exhibit structural malleability.[130] Perhaps, the observed lack of structure for GRN-3, GRN7, and GRN1 and the disordered C-termini in GRNs 4, 2, and 5[100] could account for certain degree of intrinsic disorder among GRNs and thus explain the

multifunctional roles associated with them. Additionally, according to the 2D-NMR structure of GRN4, 31 of the 58 residues were found to be unstructured.[100] However, further detailed structural-function studies are warranted to corroborate this claim especially with respect to understanding the role played by the disulfide bonds in dictating the structure and hence functions of GRNs. This research aims at understanding the structure-function relationship of one of the seven GRNs, GRN-3. The rationale behind choosing GRN-3 is:

1. Two of missense mutations implicated in FTD are in GRN-3 sequence[126] and
2. It is the only GRN for which direct experimental evidence for pro-inflammatory nature exists.[72]

The overarching hypothesis of this study is that ***disulfide bonds play a critical role in determining the structure of GRN-3 with potential implications on its multitude of functions, especially with respect to its role in neurodegenerative diseases.*** The broad questions that are being asked here are:

1. Is there a disorder within the structure of GRN-3 and what is the precise role of disulfide bonds in dictating this structural stability and/or plasticity?
2. What is the role of GRN-3 in AD? Does GRN-3 interact with Aβ peptide to modulate the latter's aggregation and neuronal toxicity?

The ensuing chapters attempt to answer these questions. In Chapter II, we investigate the role of disulfide bonds in the structure of GRN-3, first by completely abrogating the disulfide bonds (section 2.2), and second by studying the structure-function of GRN-3 with intra- as well as intermolecular disulfide bonds (section 2.5). In

Chapter III, we investigate the molecular interactions GRN-3 with Aβ to discern its role in Aβ aggregation and consequently AD pathogenesis.

CHAPTER II - ROLE OF DISULFIDE BONDS IN GRN-3

2.1 Hypothesis and Rationale

Disulfide bonds play an important role in determining the structure and the function of proteins, especially the secretory proteins that function in the extracellular matrix.[131] They are known to impart stability by decreasing the conformational entropy of the unfolded proteins.[132] Additionally, they maintain the integrity of the proteins by inducing structural rigidity thereby protecting them against the oxidants and proteolytic enzymes in the extracellular matrix.[131] The role of disulfide bonds in fostering structural rigidity has been studies in several globular proteins[133-136], antibodies[137-139], and growth factors containing the cysteine-rich kringle domains.[95, 140] Though rigid in nature, disulfide bonds can undergo cleavages/exchanges in secretory proteins like thrombospondin-1, plasmin, CD4, etc. in order to assist in their functions[131, 141-143]. Furthermore, disulfide bonds play an important role in maintaining homeostasis during oxidative stress, one example being glutathione.[144]

Granulins are highly cysteine-rich, secretory proteins each forming six intra-molecular disulfide bonds (12 cysteines). Moreover, the cysteines are highly conserved in all the seven GRNs (Figure 1.4) possibly forming same disulfide linkages as predicted for GRN4 based on its NMR structure.[100] These evidences advocate a critical role of disulfide bonds in dictating the structure and possibly the functions of GRNs. ***We hypothesize that the structure of GRN-3 is mainly dictated by the six intra-molecular bonds.***

2.2 Investigations on Fully Reduced GRN-3 (rGRN-3)

The role of the twelve conserved cysteines in determining the structure and perhaps the function of GRN-3 was determined by studying the effect of loss of disulfide bonds on its structure and functions. The following sections detail the results obtained by investigating rGRN-3.

2.3 Results

2.3.1 *In silico* Analysis Reveals rGRN-3 to be Disordered

As disulfide bonds are known to facilitate structural stability and rigidity in proteins, abrogating them completely can potentially render the protein unstructured. Therefore, to test whether rGRN-3 is disordered, we employed *in silico* prediction software called Predictor of Naturally Disordered Regions (PONDR) (www.pondr.com). PONDR uses several prediction algorithms such as VLXT[145], VLS2B[146], VL3[147], and a meta-predictor called PONDR-Fit[148] to compute the disorder propensity of amino acids assigning a disorder disposition score to proteins. Each of these tools assign the disorder score by employing artificial neural networks trained on different datasets.[148] PONDR VLXT uses three neural networks, one each for the terminal regions of the proteins and one for the internal region, trained on datasets of X-ray and NMR-derived protein structures. However, the shortcoming of PONDR VLXT is that it may be incapable of predicting long disordered segments in the proteins.[148] PONDR VL3 uses ten neural networks that are trained using sequence profiles and can accurately predict longer disordered sequences by majority voting. PONDR VLS2B uses neural networks that can accurately predict both short and long disordered sequences and are trained on sequence profiles as well as sequence alignments from PSI-BLAST (position-specific iterated

BLAST) and secondary structure predictors PHD and PSI-pred.[146] As mentioned earlier, PONDR Fit is a meta-predictor and is constructed by combining the prediction algorithms of other meta-predictors like PONDR VLXT, PONDR VLS2, and PONDT VL3 along with other predictors like FoldIndex, IUPred, and TopID.[148] PONDR analyses of rGRN-3 revealed that rGRN-3 is completely disordered according to VLS2B and VL3 prediction with a disorder disposition score of >0.6 (Figure 2.1B, blue and red lines) whereas PONDR Fit and VLXT predicted that only 60 and 30% of rGRN-3 is disordered with a disorder disposition score of >0.5, respectively (Figure 2.1B, green and grey lines). Thus, PONDR analyses of rGRN-3 showed disparity in the predictions. This disparity could arise due to following reasons:

1. PONDR VLXT uses a training data set consisted of only 15 cysteine-containing proteins and the cysteine content in these protein is very low (0.5-20%) that are present both in reduced and oxidized form.[145] This makes it less accurate in predicting the disordered disposition of GRN-3 with cysteine content of nearly 20%
2. VL3 and VLS2B could be more accurate in predicting disordered disposition of rGRN-3 than VLXT as they are more accurate in predicting larger disordered regions with >30 amino acids

Therefore, to test if the disparity in prediction is due to the presence of twelve cysteines in rGRN-3, same tools were used to predict the disorder disposition of GRN-3 with cysteines replaced with alanine (alaGRN-3) and serine (serGRN-3). As expected, both VLXT and PONDR Fit, as well as VL3 and VSL2B, predicted disorder for more

than 90% of the protein sequence with a disorder disposition of >0.5 (Figures 2.1C and D).

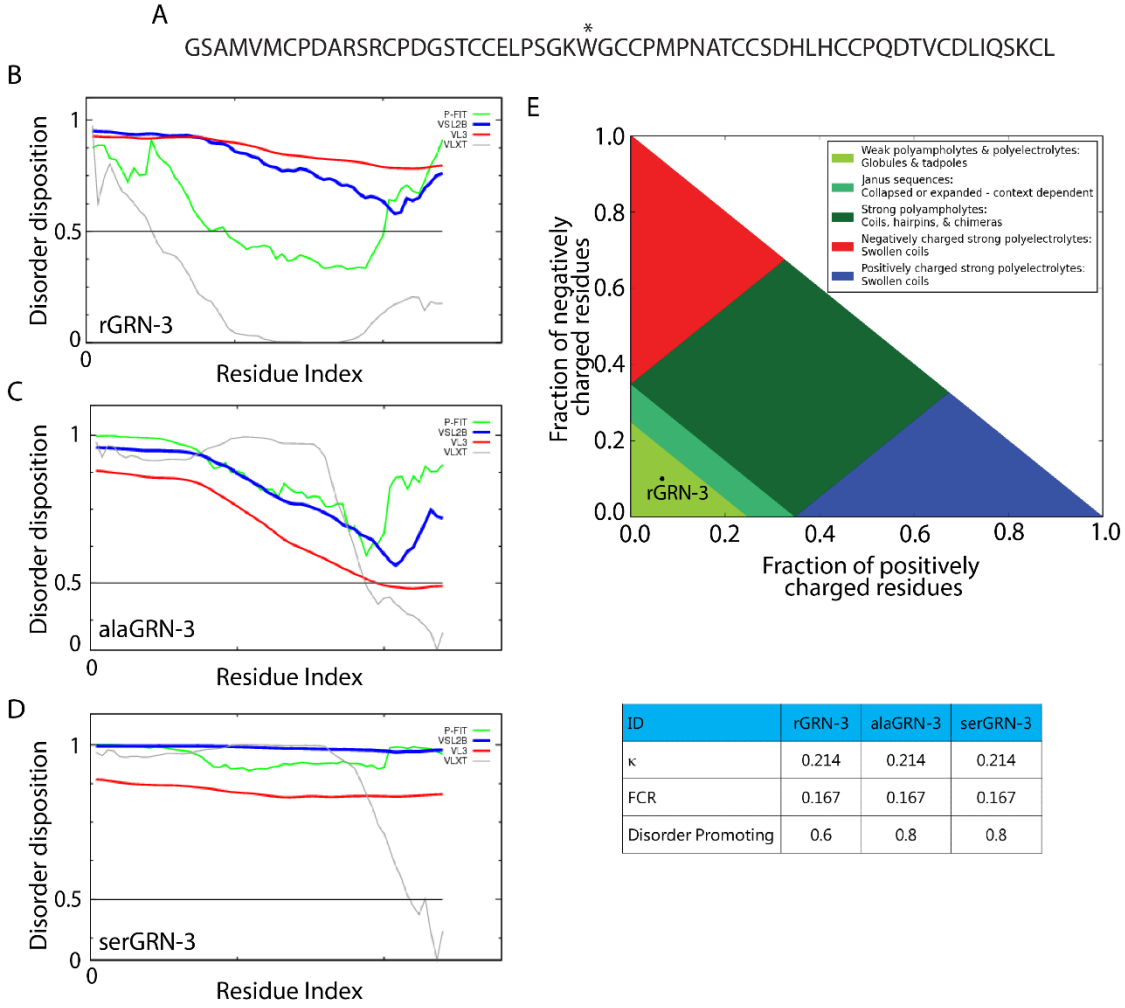

ID	rGRN-3	alaGRN-3	serGRN-3
κ	0.214	0.214	0.214
FCR	0.167	0.167	0.167
Disorder Promoting	0.6	0.8	0.8

Figure 2.1 *In silico* analysis of intrinsic disorder of rGRN-3, alaGRN-3, and serGRN-3.

A Primary sequence of rGRN-3. The * at position 28 indicates the Y to W substitution made to facilitate spectroscopic analyses. B, C, and D, PONDR (predictor of naturally disordered regions) analyses of rGRN-3, alaGRN-3, and serGRN-3, respectively using VLXT (grey), VSL2B (blue), VL3 (red) and PONDR-Fit (green) predictors. E, CIDER analysis of rGRN-3, alaGRN-3, and serGRN-3 using the diagram of states (plot of positively charged residues vs. fraction of negatively charged residues). CIDER analyses compute low a low kappa (κ) value of 0.214, low FCR (fraction of charged residues) value of 0.167, and disorder-promoting value of 0.6 for rGRN-3 and 0.8 for alaGRN-3 and serGRN-3, respectively.

Though cysteines are considered to be order-promoting amino acids, the disparity observed in case of rGRN-3 indicates the lack of attributes of the amino acid (oxidized

vs. reduced) in disorder predicting software. Further, rGRN-3 and the alaGRN-3 and serGRN-3 were analyzed using another bioinformatic tool called CIDER or Classification of Intrinsically Disordered Ensemble Region[149] and found that rGRN-3 as well as alaGRN-3 and serGRN-3 (Figure 2.1E, black dot) fall in the region 1 (Figure 2.1E, light green) of the diagram of states (plot of fraction of positively charged residues vs. the fraction of negatively charged residues) indicating that the proteins are weak polyampholytes or polyelectrolytes with globular random coils. Aβ42, an IDP implicated in AD, also falls in the same region (data not shown). Based on the CIDER analyses, the κ value (indicator of charged amino acid mixing within a sequence) and FCR (fraction of charged residue) value for rGRN-3, alaGRN-3, and serGRN-3 were 0.214 and 0.167, respectively (Figure 2.1E, Table). Additionally, the disorder-promoting score as per CIDER analyses for rGRN-3 was 0.6 while that for ala- and serGRN-3 was 0.8 further implicating that rGRN-3 and its ala and ser mutants are unstructured.

2.3.2 rGRN-3 Shows Potential to Dimerize via Non-Covalent Interactions

In order to facilitate spectroscopic characterization of rGRN-3, a Y24W substitution was introduced in the sequence (Figure 2.1A, *). This substitution can be considered inert and will probably not alter the native structure of GRN-3 as W is conserved at this position in all GRNs except for GRN-3 and GRN-1. This Y24WGRN-3, denoted as rGRN-3, was expressed recombinantly in *E. coli* SHuffle^{TM} cells (NEB labs) as a thioredoxin fusion protein as both the thioredoxin tag and the SHuffle cells promote disulfide bond formation in the cytoplasm. The overall purification strategy to yield rGRN-3 has been summarized in Figure 2.2. Briefly, after Ni^{2+}-NTA affinity purification of trxA-GRN-3, it was reduced with molar excess of TCEP-HCl (Tris (2-carboxyethyl)

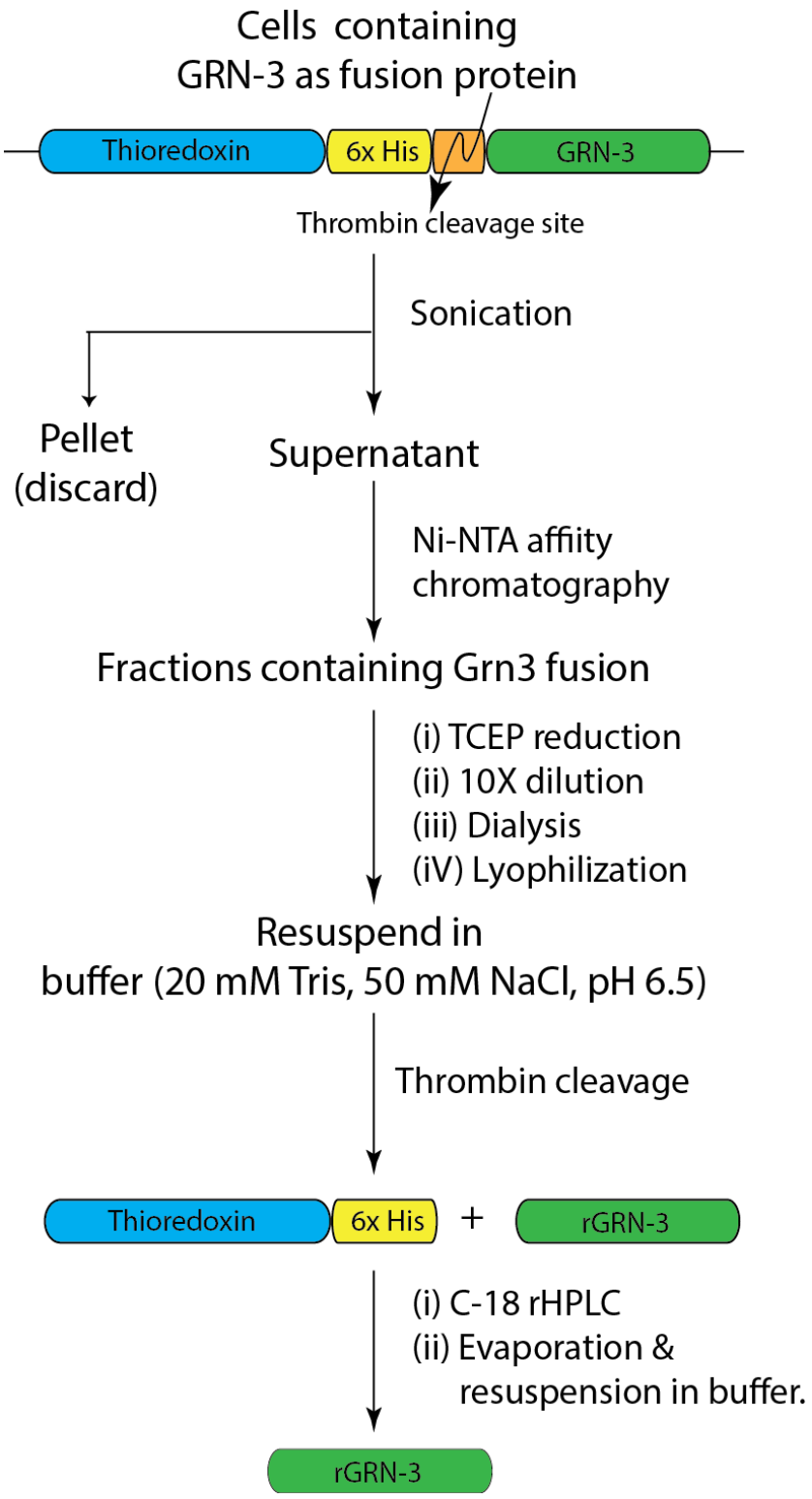

Figure 2.2 Schematic of rGRN-3 Purification.

phosphine hydrochloride) which is a strong reducing agent and reduces all the disulfide bonds. The reduced eluate was diluted to 10-20 times in volume using appropriate buffer and dialyzed to gradually remove imidazole and TCEP. However, surprisingly, even after dialyzing TCEP, the protein remained reduced for 5-6 h at room temperature (described in detail later in the chapter). The concentration of the protein was estimated spectrophotometrically using the calculated molar extinction coefficient of 6250 $M^{-1}cm^{-1}$ at 280 nm[150]. HPLC fractionation of thrombin-cleaved thioredoxin fused rGRN-3 resulted in the elution of rGRN-3 in fractions 10 and 11 (Figure 2.3A, arrow). The other peak seen on the HPLC profile is of thioredoxin. rGRN-3 when analyzed using SDS-PAGE under reducing and non-reducing conditions revealed a single band at about ~6.3 kDa under both the conditions (Figure 2.4B, lanes 1 and 2) corresponding to the monomeric rGRN-3 as the monoisotopic mass of monomeric rGRN-3 is 6367.39 Da as computed using the Compute PI/Mw tool at expasy.org. The MALDI-ToF analysis of purified rGRN-3 showed a major peak at an m/z value of 6367.72 Da corresponding to its monomeric molecular weight. Further, when analyzed using SDS-PAGE without the heat treatment under non-reducing condition, a diffuse band was observed at around ~13 kDa, corresponding to the dimeric mass of rGRN-3, in addition to monomeric rGRN-3 (Figure 2.4B; lane 3*).* Since, the proteins electrophorese as a single monomeric band under reducing and non-reducing conditions formation of intermolecular disulfide bonds can be ruled out, implicating that the dimerization must be predominantly due to non-covalent interactions. In support of this claim, indeed, a peak at m/z of 12735.3 Da corresponding to dimeric rGRN-3 was also observed in MALDI-ToF spectrum (Figure 2.4C).

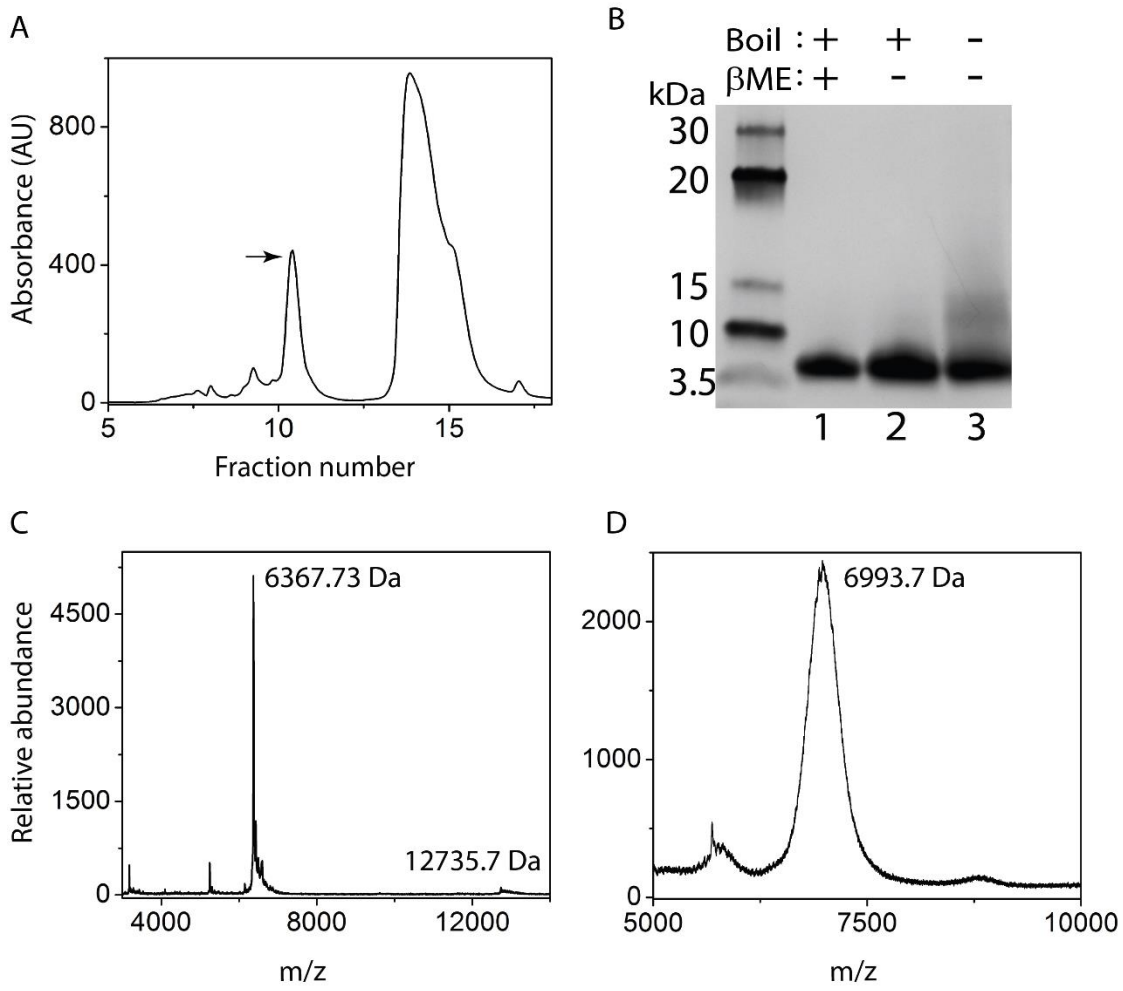

Figure 2.3 Characterization of Recombinant rGRN-3.

A, HPLC profile of rGRN-3 purification after thrombin cleavage. The peak marked with an arrow indicates the fraction corresponding to the rGRN-3. The other peak is of thioredoxin. B, SDS-PAGE analysis of the rGRN-3 fraction marked with an arrow on the HPLC profile. Lane 1 is rGRN-3 reduced using 2-mercaptoethanol (β-ME) and boiled; Lane 2 is non-reduced and boiled rGRN-3 sample; Lane 3 is non-reduced and not boiled rGRN-3 sample. C, MALDI-ToF analysis of rGRN-3 indicating a m/z of 6367.39 Da, corresponding to monomeric mass (theoretical MW 6367.4 Da) and a second peak with m/z of 12735.7 Da corresponding to dimeric rGRN-3. D, Alkylation of rGRN-3 with iodoacetamide, showing a signal at 6993.7 Da indicating presence of 10.7 (~11) free thiols (reduced cysteines). The results are representative of three or more consistent repeats.

In order to confirm that the protein is indeed reduced, Ellman's assay and alkylation using iodoacetamide were carried out. Ellman's assay performed on freshly purified rGRN-3 samples indicated >95% of the cysteines were in the reduced form. Further

iodoacetamide alkylation unambiguously confirmed that the protein was indeed reduced, as the treatment yielded a single peak with m/z value of 6993.7 equivalent to 10.7 (~11) cysteines being present as free sulfhydryls (Figure 2.3D). Thus, the percentage of free cysteines as calculated using Ellman's results was in good agreement with those obtained via alkylation confirming that over 90% of the rGRN-3 was present in a reduced form. In order to assess the extent of re-oxidation of disulfide bonds, Ellman's assay was performed on rGRN-3 sample incubate at room temperature for 6 h, the timeframe within which most of the experiments were performed. The assay revealed that 95 % of cysteines remained reduced within the timeframe (Figure 2.4A).

A

Ellman's Assay

Time	Blank (AU)	rGRN-3 (AU)	% free sulfhydryls
0 hr	0.1942	0.4797	95 %
6 hr	0.1677	0.4691	99 %
7 d	0.1769	0.7794	99 %

B

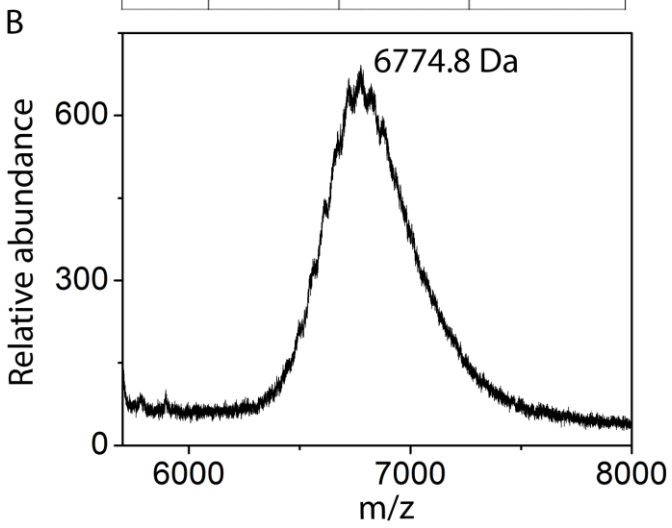

Figure 2.4 Re-oxidation of rGRN-3.

A, Ellman's assay results on potential re-oxidation of rGRN-3 within the experimental window and after incubation for 7 days at 4 °C. B, rGRN-3 was alkylated using iodoacetamide after incubation at 4 °C for 20 days, showing a signal corresponding to 6774.8 Da indicating presence of seven free sulfhydryls.

Furthermore, even after incubation of the protein up to 7 days at 4 °C showed no change in oxidation content based on the Ellman's analysis (Figure 2.4A). Only after 20 days at 4 °C, four out of twelve cysteines of rGRN-3 re-oxidized based on iodoacetamide alkylation (Figure 2.4B).

2.3.3 rGRN-3 is Intrinsically Disordered at Low Concentrations

Several experimental evidences were gathered to validate the disordered structure of rGRN-3 as predicted by PONDR analysis. The secondary structure of rGRN-3 at different protein concentrations was analyzed using far-UV circular dichroism (CD) spectroscopy. rGRN-3 was observed to be predominantly disordered between concentrations of 10 and 100 μM as indicated by the canonical random coil CD spectrum exhibiting a minimum at λ = 200 nm observed for disordered proteins (Figure 2.5A). Concentrations below 10 μM also exhibited random coil structure (Figure 2.6A). The degree of disorder was inversely proportional to protein concentration as the rGRN-3 concentration increased above 100 μM, a decrease in the ellipticity at 200 nm (indicative of random coil) and a consequent increase in negative ellipticity at 222 nm, indicative of α-helical structure was observed (Figure 2.5A). This inverse proportionality became more distinct at concentration 300 μM and above, exhibiting a distinct negative ellipticity at 225 nm (Figure 2.5A; *inset*) suggesting a transformation towards α-helical structure (222 nm) with contributions from turns and loops (230 nm). The spectra above 800 μM indicated a sharp negative minimum at 230 nm, suggesting presence of loops and turns, however, the spectrum was partly obscured by fluctuations associated with high voltage at low wavelengths (Figure 2.6B). When subjected to zonal fractionation by size exclusion chromatography (SEC), rGRN-3 eluted at fractions three times higher than its

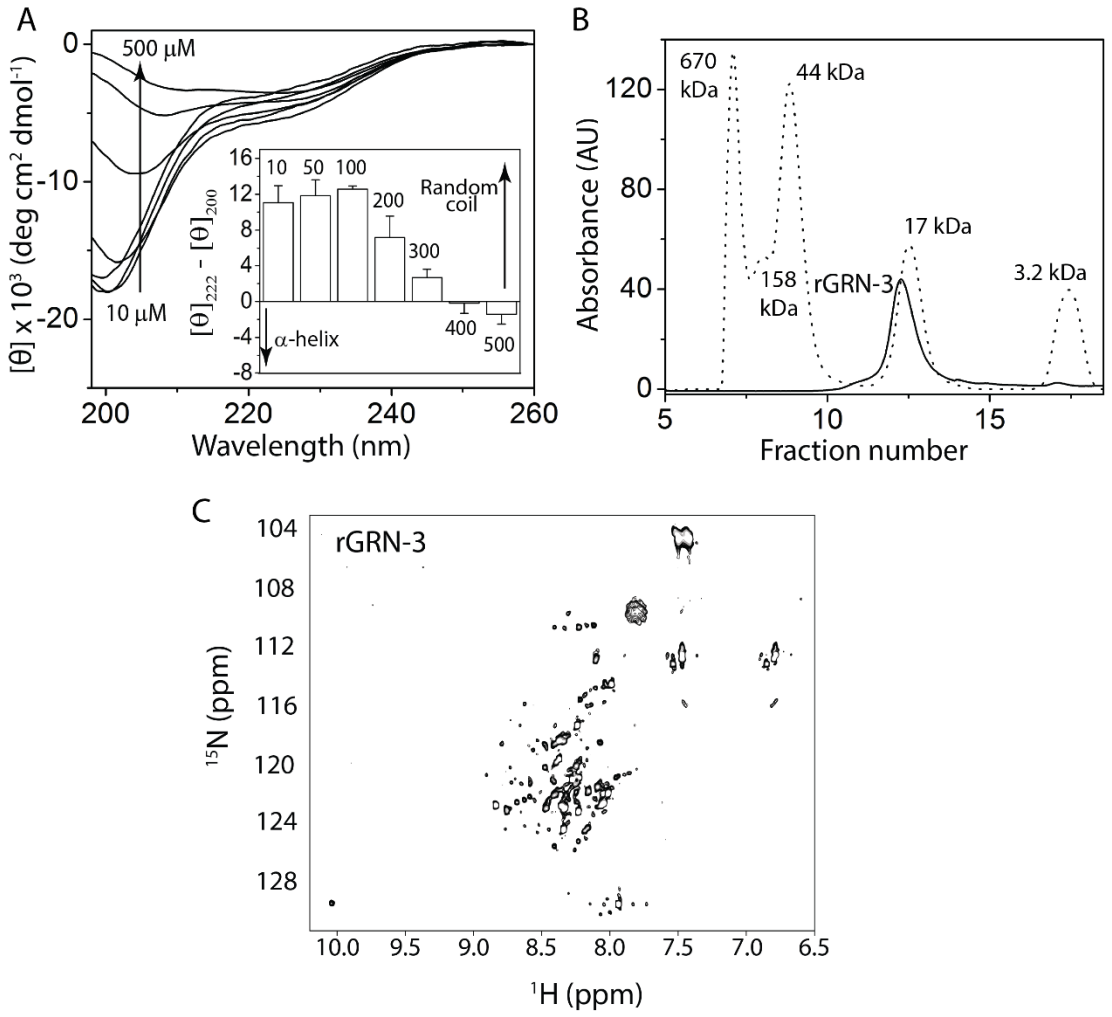

Figure 2.5 rGRN-3 is an IDP.

A, Concentration-dependent conformational changes in rGRN-3 observed by far-UV CD. (*Inset*) Spectra as a difference in the molar ellipticities at 222 nm (helix) and 200 nm (random coil). B, Fractionation of rGRN-3 using a Superdex^{TM} 75 size exclusion column (solid line) compared to that of gel filtration standards (dotted line) – 1-bovine thyroglobulin (670 kDa), 2-bovine γ-globulin (158 kDa), 3-chicken ovalbumin (44 kDa), 4-horse myoglobin (17 kDa), and 5-vitamin B_{12} (1.35 kDa). C, ^{1}H-^{15}N SoFast HMQC NMR spectrum of rGRN-3.

monomeric molecular weight when compared to the globular protein standards (BioRad) (Figure 2.5B, dotted line). Several IDPs typically exhibit a 2-3 fold increase in molecular weight during SEC fractionation due to the increased hydration sphere around the unfolded structure[151] further confirming the disordered structure of rGRN-3. To obtain unambiguous evidence for the disordered structure of rGRN-3, ^{1}H-^{15}N HMQC NMR was

performed. In ^{1}H-^{15}N HMQC, the resonances of the backbone amide nitrogen of each residue (with the exception of prolines) can be correlated to the resonance of amide protons and the amide bonds along with the side chain amide nitrogens give signals.[152] The ^{1}H-^{15}N HMQC spectrum of rGRN-3 showed lack of dispersion for the resonances on the proton dimension; most of the proton resonances were seen between 8.0 and 8.5 ppm for ^{1}H, however, the resonances were well-dispersed between 104 and 128 ppm on ^{15}N (Figure 2.5C). This difference in the spectral dispersion in the proton and nitrogen dimensions is indicative of structural disorder.[152] Moreover, most of the resonances in the proton dimension were overlapping and showed significant line broadening confirming that rGRN-3 is an IDP.

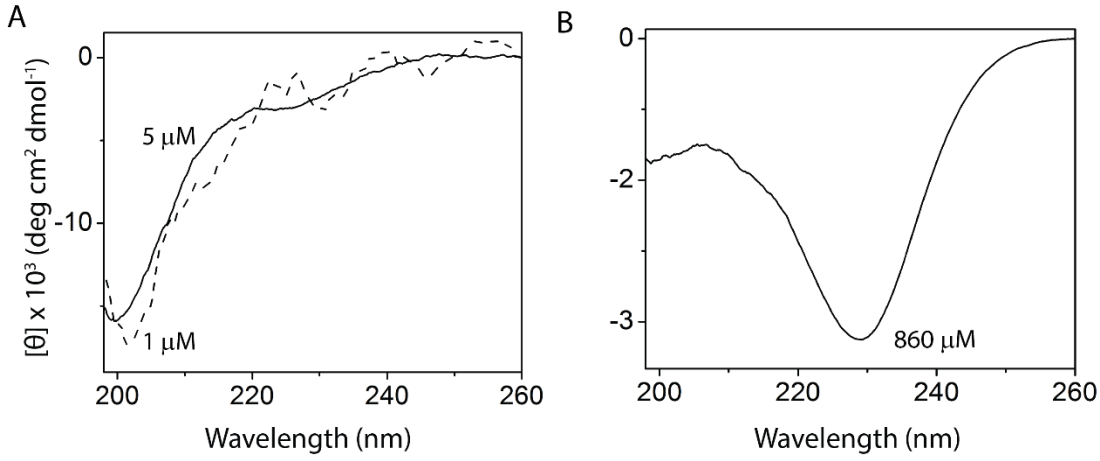

Figure 2.6 Far-UV CD spectra of rGRN-3 at low and high concentrations.

A, 1 μM (dashed line) and 5 μM (continuous line), and B, 860 μM.

To further confirm the intrinsic disorder of rGRN-3, the effect of osmolytes like trifluoroethanol (TFE) and trimethylamine N-oxide (TMAO) on the structure of rGRN-3 was assessed. TFE is a known α-helix inducer while TMAO facilitates formation of folded structures in proteins.[153] The far-UV CD spectra of rGRN-3 obtained in the presence of increasing concentrations of TFE showed that TFE induced α-helical

conformation within rGRN-3 at concentrations as low as 20-30% TFE (Figure 2.7A). The mid-point of this transition (equivalent to the melting point during protein unfolding) was low, ~16 ± 5% TFE (Figure 2.7A, *inset*), which provides further evidence that rGRN-3 is intrinsically disordered as typically disordered proteins tend to have low transition mid-point. Similarly, TMAO also induced significant conformational changes in rGRN-3 (Figure 2.7B). As the TMAO concentrations increased, significant loss of random coil structure was observed (decrease in negative minimum at 198 nm) and at higher concentrations, a negative minimum at around 216 nm and a positive maximum at 198nm were observed, indicative of β-sheet conformation (Figure 2.7B). These changes were predominantly observed at 198 nm where the negative minimum became a positive maximum with increasing TMAO concentrations. Collectively, these results indicate that rGRN-3 is an intrinsically disordered protein as predicted by *in silico* analyses.

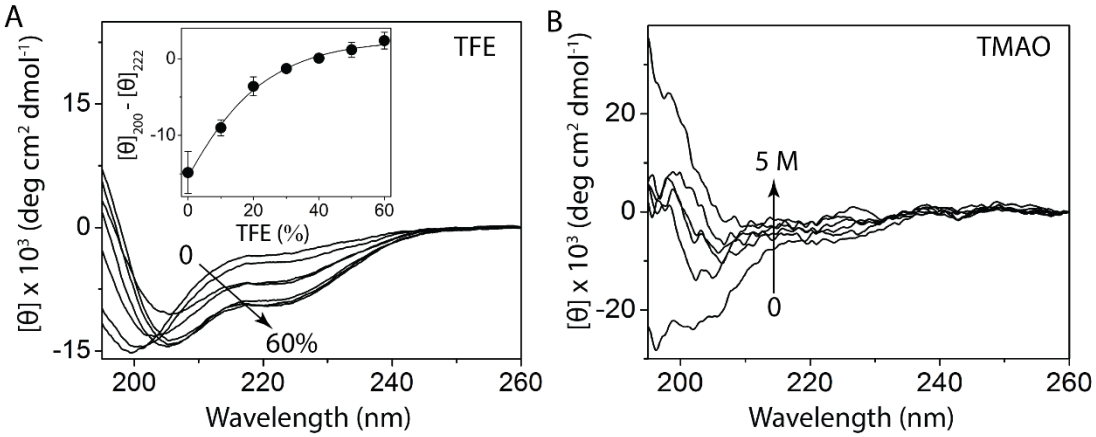

Figure 2.7 Effect of osmolytes on rGRN-3 structure.

A, Far UV CD spectra of rGRN-3 in the presence of increasing concentrations of TFE. (*Inset*) The difference in the ellipticities between 208 and 222 nm (helix) plotted against the percentage of TFE. The data was fitted with Boltzmann's sigmoidal equation to obtain a melting concentration of 16 ± 5% TFE. B, Far UV CD spectra of rGRN-3 in presence of increasing concentrations of trimethylamine N-oxide (TMAO).

2.3.4 rGRN-3 Dimerizes to Form a Fuzzy Complex

The SDS-PAGE analysis of rGRN-3 under non-reducing condition without the heat treatment alluded to the fact that rGRN-3 forms non-covalent dimers (Figure 2.3B). To obtain further evidence that rGRN-3 dimerizes via non-covalent interactions, electrophoretic, spectroscopic, and sedimentation analyses were performed. The electrophoresis of 100 μM rGRN-3 under non-denaturing and non-reducing conditions using a 25 mM Tris running buffer, pH 8.8 revealed a diffuse band corresponding to dimeric (D; 12.6 kDa) as well as monomeric (M; 6.3 kDa) (Figure 2.8A; *inset*). The electrophoresis of Aβ42 under identical conditions yielded three distinct bands corresponding to monomer (M; 4.5 kDa), dimer (D; 9 kDa), and trimer (T; 13.5 kDa) (Figure 2.8A; *inset*). Both rGRN-3 and Aβ42 have very similar pIs; 5.33 and 5.31, respectively, and hence their electrophoretic mobility is comparable provided all the other conditions are maintain constant. Further, sedimentation velocity analysis of rGRN-3 again at 100 μM by analytical ultracentrifugation (AUC) showed two peaks; a major peak at 1.5 S, which was deconvoluted to 13.1 kDa corresponding to dimeric rGRN-3 and a minor peak at 0.4 S, which was deconvoluted to 4.5 kDa, indicative of monomeric rGRN-3 (Figure 2.8A). Dimerization was also probed spectroscopically using ANS and tryptophan fluorescence. ANS or 8-anilino naphthalene sulfonic acid binds specifically to solvent-exposed hydrophobic surfaces on proteins. In the ANS fluorescence assay, the concentration of rGRN-3 was varied from 1 to 25 μM keeping the ANS concentration constant at 500 μM (Figure 2.8B; *inset*). When the normalized ANS fluorescence emission, monitored at 512 nm, was plotted against rGRN-3 concentration, an

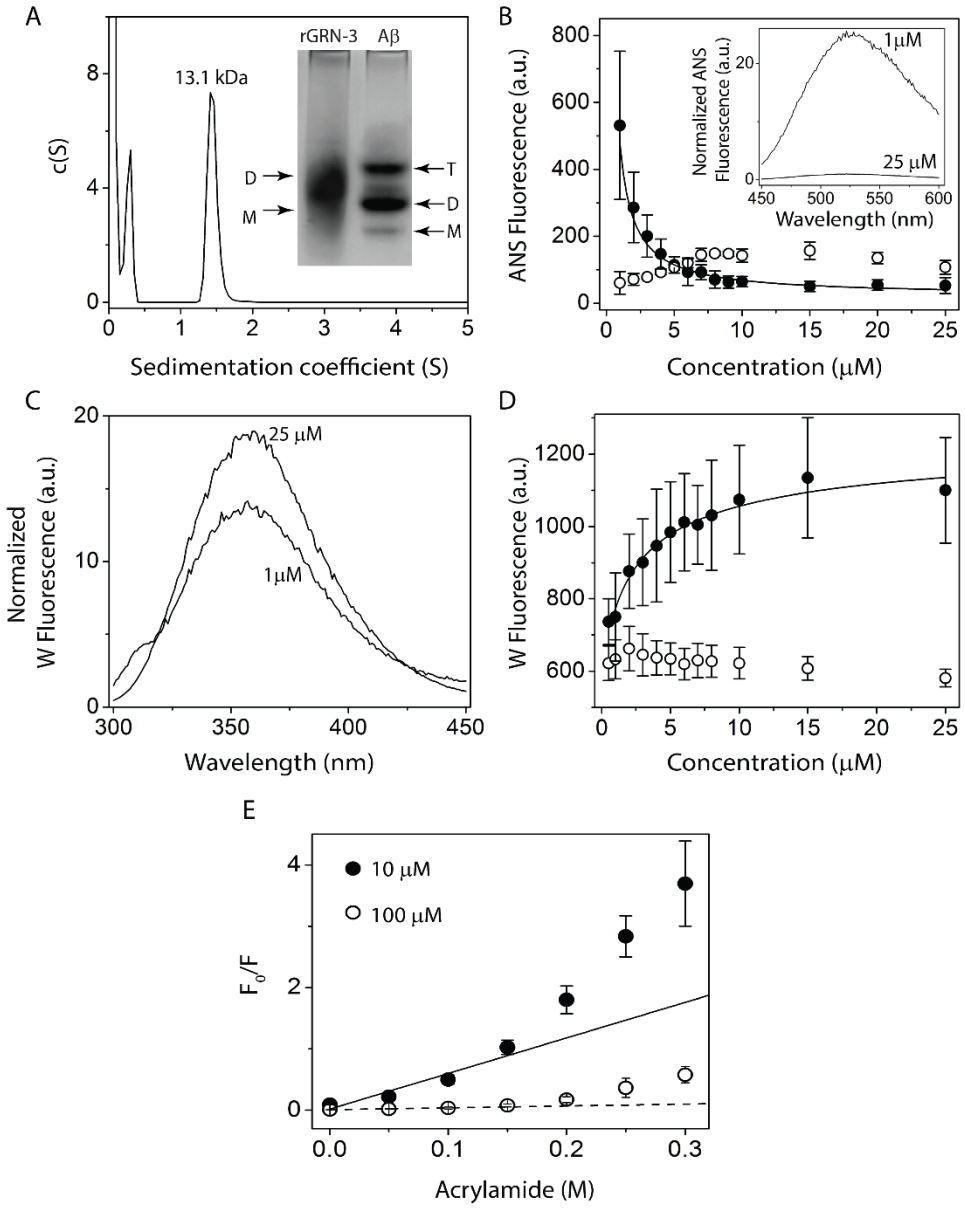

Figure 2.8 Dimerization of rGRN-3.

A, Molecular size distribution of rGRN-3 at 100 μM obtained by sedimentation velocity indicates a predominant dimer (MW 13.1 kDa). (*Inset*) Native PAGE analysis of rGRN-3 at 100 μM run on a 14% gel indicates a diffuse dimeric band corresponding to ~13 kDa, based on the Aβ sample electrophoresed in parallel for which monomer (M; 4.5 kDa), dimer (D; 9.0 kDa), and trimer (T; 13.5 kDa) are observed. B, *and* D, rGRN-3 (●) concentration-dependent ANS binding and intrinsic tryptophan fluorescence, respectively. The normalized fluorescence was plotted against protein concentration, and data was fitted (solid line) to a monomer-dimer model as described in SI. Bovine serum albumin (BSA) (○) was used as a negative control. (*Inset*) B, Representative normalized ANS fluorescence scans of 25 μM and 1 μM rGRN-3. C, Representative normalized tryptophan fluorescence scans of 25 μM and 1 μM rGRN-3. E, Normalized Stern-Volmer plots for 10 (●) and 100 (○) μM rGRN-3 using acrylamide as the quenching agent.

exponential decay curve was obtained with increasing rGRN-3 concentration (Figure 2.8B; ●). This exponential decrease with increasing concentration suggested that lower concentrations of rGRN-3 contain more solvent-exposed hydrophobic binding surfaces and as the concentration increased, the available hydrophobic surfaces for ANS binding decreased, likely due to the involvement of these hydrophobic surfaces in dimerization, rendering them unavailable to ANS to bind. The normalized data was fitted to the following monomer-dimer model:

$$F = \frac{2}{M} * \left\{ F_0 - \left(F_0 - F_f\right) * \left(\frac{(4M + K_d) \pm \sqrt{(4M + K_d)^2 - 16M^2}}{8} \right) \right\}$$

Based on this model, an apparent dissociation constant, K_d^{app} of 0.24 ± 0.02 μM was calculated. As a negative control, ANS binding to BSA, which is known to undergo weak dimerization was monitored. BSA showed an increase in normalized ANS fluorescence intensity with an increase in protein concentration (Figure 2.8B; ○). In addition to ANS fluorescence, the intrinsic fluorescence emission arising from solvent exposure of the single tryptophan residue (Y24W) within rGRN-3 was monitored as a function of protein concentration. The protein was serially diluted using 20 mM Tris, pH 6.5, containing 0.01% NaN_3 and the W fluorescence was monitored for each dilution. At low rGRN-3 concentrations, the λmax for tryptophan emission was observed at 355 nm which is typical for a solvent exposed W residue in an IDP. At high rGRN-3 concentration, a slight blue shift (to 352 nm) in the λmax of W residue was observed (Figure 2.8C), indicative of a small change in the hydrophobic environment around the tryptophan residue possibly due to dimerization. Further, the normalized fluorescence showed an exponential increase with increasing rGRN-3 concentration (Figure 2.8D; ●), suggesting

a distinct conformational change around the tryptophan residue, similar to that observed previously for human interferon γ.[154] Fitting the data with the same monomer-dimer model as used in case of ANS binding, yielded an apparent K_d^{app} of 0.9 ± 0.17 μM, comparable to the value obtained from ANS binding data. Again BSA, as a negative control, showed relatively weak transitions in normalized fluorescence intensity, indicating very weak dimerization (Figure 2.8D; ○). To provide further evidence to support conformation changes occurring around the tryptophan reside due dimerization of rGRN-3, solvent accessibility of tryptophan at low and high rGRN-3 concentrations was investigated by Stern-Volmer analysis.[155] The assay involved monitoring the tryptophan fluorescence in the presence of increasing concentration of a fluorescence quencher like acrylamide. A significant deviation from linearity was observed at both low (10 μM, Figure 2.8E; ●) and high concentrations (100 μM, Figure 2.8E; ○). The upward curvature of the fluorescence intensities was indicative of both static and dynamic quenching mechanisms due to tryptophan being solvent exposed. Further, the deviation of the normalized fluorescence intensity was more distinct at lower rGRN-3 concertation as compared to higher rGRN-3 concentrations indicating that the tryptophan is more solvent exposed at lower concentration when the protein is monomeric as against at higher concentration when rGRN-3 is predominantly dimeric. The quenching experiments at concentrations below 10 μM could not be performed as intensities dropped below detection limits. However, since 10 and 100 μM rGRN-3 would contain significant monomer and dimer populations, respectively, the data provides a reliable insight into solvent exposure surrounding the tryptophan residue.

The secondary structure and the NMR analyses of rGRN-3 indicate that rGRN-3 exists as an IDP within the concentration range of 10-100 μM (Figure 2.5A and C), concentration at which is exhibits monomer-dimer dynamic. Thus, rGRN-3 associates to form dimers without a net gain in the overall structure. Typically, when IDPs self-associate or associate with their binding partner, they undergo a disorder to order transition. However, an increasing number of IDPs have been shown to self-associate without undergoing disorder to order transition; they remain disordered and form fuzzy complexes.[156 157-160] Thus, rGRN-3 forms a fuzzy complex containing intrinsically disordered, homogenous dimers. Collectively, these data indicate that rGRN-3 displays following concentration-dependent changes:

1. < 1 μM – intrinsically disordered, monomeric,
2. 50-100 μM - intrinsically disordered, dimeric, and
3. 300 μM – partially α-helical/turns.

2.3.5 Low Concentrations of rGRN-3 Activate NF-κB in SH-SY5Y Human Neuroblastoma Cells

Native GRN-3 has been shown to be pro-inflammatory.[72] However, several secretory proteins that are rich in disulfide bonds undergo disulfide cleavages or exchanges to perform their functions.[131] Though rare, rGRN-3 can likely be present in rare circumstances such as cellular stress or during the breakdown of protein folding machinery and may elicit inflammatory response. Therefore, the ability of rGRN-3 to activate NF-κB a generic marker for neuroinflammation, was assessed in SY-SH5Y human neuroblastoma cells. These experiments were conducted by our collaborator, Dr. Melissa Moss's lab at the University of South Carolina. In this assay, the

immunocytochemistry was coupled with an antibody specific for an epitope that is accessible on the p65 or RelA subunit of NF-κB only when NF-κB is present in an unbound state. When NF-κB is bound to inhibitor of κB (IκB), it remains inactive in the cytoplasm. An inflammatory stimulus will trigger the phosphorylation, ubiquitination, and degradation of IκB and subsequent release of NF-κB leading to its activation and nuclear translocation.[161-163] Thus, the primary antibody employed in these immunocytochemistry studies is specific for the activated form of NF-κB.

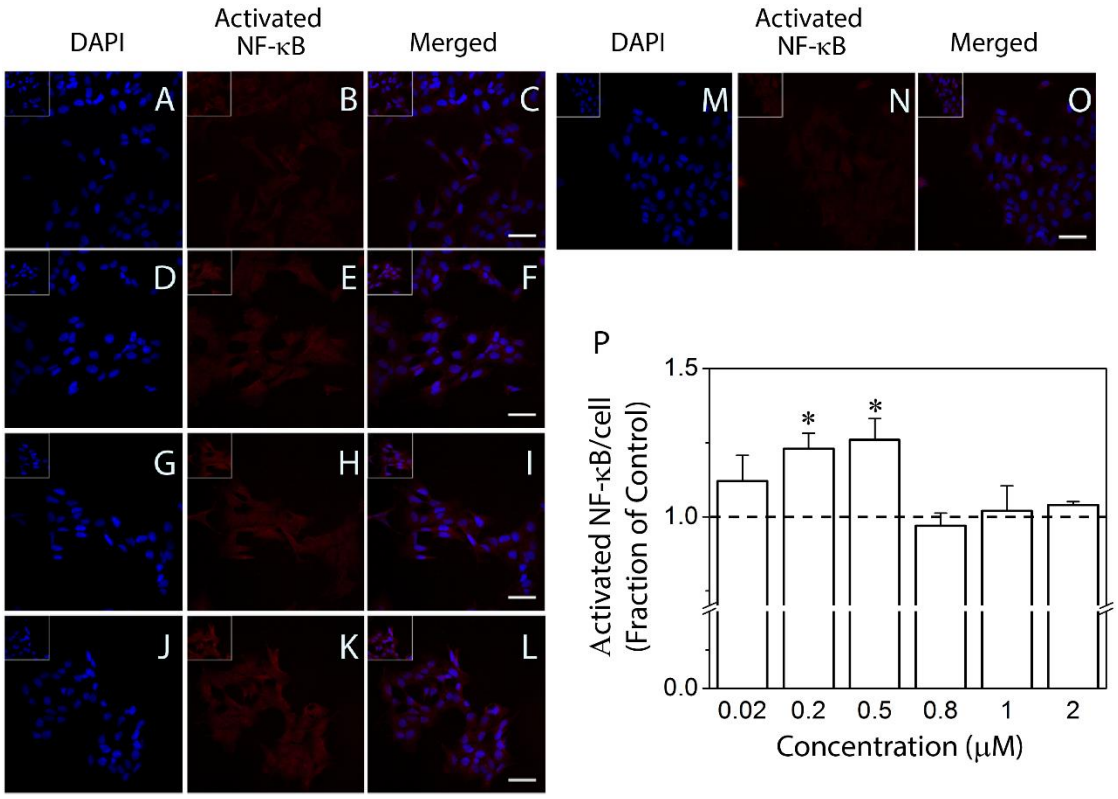

Figure 2.9 Effect of rGRN-3 on NF-κB activation in SH-SY5Y cells.

SH-SY5Y cells were incubated alone (control, A – C) or in the presence of 0.02 (D – F), 0.2 (G – I), 0.5 (J – L), 0.8 (not shown), 1 (not shown), or 2 μM (M – O) rGRN-3. Immunofluorescence staining was performed for the activated form of NF-κB (red) in conjunction with nuclear DAPI (blue) staining. Scale bars = 50 μm. Inserts located in top left corners represent 1.5x magnification. *P*, Activated NF-κB staining intensity per cell was analyzed using a custom MATLAB routine as described in the Experimental Procedures. Results are reported relative to the control. Error bars indicate SEM, n = 3-4. *$p < 0.05$, relative to the control.

SH-SY5Y cells treated with the negative control displayed low NF-κB activation (Figure 2.9A-C). When cells were exposed for 60 minutes to medium containing 0.02 μM rGRN-3, a slight increase in NF-κB activation was observed (Figure 2.9D-F). However, image analysis employed to quantify activated NF-κB staining per cell revealed that this increase did not reach significance (Figure 2.9P). In contrast, SH-SY5Y cells treated with medium containing 0.2 μM or 0.5 μM rGRN-3 demonstrated a significant increase in NF-κB activation when compared to the control (Figure 2.9G-L, P). Thus, at rGRN-3 concentrations of 0.5 μM or lower, a dose-dependent increase in rGRN-3 activation of NF-κB was observed. Treatment of SH-SY5Y cells with higher rGRN-3 concentrations of 0.8 μM, 1 μM, and 2 μM (Figure 2.9M-O, P), however, failed to elicit any increase in NF-κB activation. This latter result indicates that the dose-dependent increase in rGRN-3 activation of NF-κB does not extend to concentrations 0.8 μM and above.

2.4 Discussion and Conclusions

The objective of this study was to determine the role of the six intra-molecular disulfide bonds in dictating the structure of GRN-3 by studying the effect of the abrogation of these disulfide bonds on GRN-3 structure. The advantage of this approach over making cysteines mutants is that any changes in the structure would primarily be due the removal of disulfide bonds and not due introduction of other amino acids in the primary sequence. However, the challenge with this approach is to maintain the cysteines in the reduced form as sulfhydryls can inherently oxidize to form disulfide linkages. The purification strategy adopted yielded reduced GRN-3 that was resistant to spontaneous

oxidation in the timeframe of all the experiments as shown by Ellman's and alkylation results (Refer section *2.5.2*; Figure 2.4).

This study established that rGRN-3 is an IDP at low concentrations, as predicted by the PONDR and CIDER analyses. This results suggests that abrogation of disulfide bonds renders the protein unstructured and that these disulfide linkages are the sole driving force dictating the structure of the protein. This finding is significant as it answers the overarching question regarding the role of disulfide linkages in determining the structure of GRNs and can be extrapolated to all the other six GRNs as the cysteines and putatively even the disulfide bonding pattern is conserved among all the GRNs. Interestingly, the intrinsically disordered rGRN-3 exhibits concentration-dependent structural changes and exists as non-covalent dimers at higher concentrations. Moreover, it dimerizes without any gain in the secondary structure forming fuzzy complexes, a characteristic exhibited by an increasing number of IDPs.[159, 164] Thus, the results obtained in this study implicate that the structure of native, oxidized GRN-3 is predominantly dictated by the six intra-molecular disulfide bonds and not the inherent property of amino acids to form secondary and tertiary structures.

Interestingly, removal of disulfide bonds doesn't affect the pro-inflammatory nature of GRN-3 as the data presented shows that rGRN-3 is capable of activating NF-κB, a generic pro-inflammatory marker, in a dose-dependent manner in the SH-SY5Y human neuroblastoma cells. Moreover, the NF-κB activation is attenuated at higher concentration indicating that monomeric rGRN-3 has higher pro-inflammatory activity as compared to dimeric rGRN-3. The concentration (0.5 – 0.8 μM) at which rGRN-3 maximally activates NF- κB overlaps with the monomer-dimer dynamics of rGRN-3 and

is in close agreement with the apparent dissociation constant (K_d^{app}) for rGRN-3 dimerization (0.2-0.9 μM). Although, physiologically this pro-inflammatory nature of rGRN-3 may not hold much relevance but in certain rare situations such as metabolic or oxidative stress or during breakdown of folding machinery, GRN-3 may undergo disulfide cleavage and exists in the reduced form. Moreover, since rGRN-3 is an IDP that are evolutionary adapted to have pleiotropic functions[165], the presence of rGRN-3 in the extracellular matrix may be physiologically relevant in certain conditions.

Thus, the overall conclusions from this study are that rGRN-3 is an IDP at low concentrations implicating that the disulfide bonds are the sole driving force for maintaining the structure of GRN-3. Investigating the structure-function relationship of the native GRN-3 is, therefore, imperative to finding evidence in support of our hypothesis I. The ensuing sections will provide answers to these questions.

2.5 Investigations on Native GRN-3

The abrogation of the disulfide bonds in GRN-3 renders the protein disordered, as detailed in the previous chapter. These results corroborate with the proposed hypothesis that the reduction of the disulfide bonds results in complete loss of structure of GRN-3 and implicates that the disulfide bonds could be the main driver for the structural integrity of GRN-3. However, rGRN-3 provides an indirect evidence for the role of disulfide bonds in driving the structure of GRN-3. Therefore, to understand the role of played by disulfide bonds in dictating the structure of GRN-3 and its functions, it is imperative to characterize the structure and the function of the native GRN-3 with completely oxidized six intra-molecular disulfide bonds. The subsequent sections present the biophysical and biochemical characterization of the native GRN-3.

2.6 Results

2.6.1 Recombinant Expression of GRN-3 in *E. coli* Show Significant Disulfide Bond Scrambled Multimers

GRN-3 was expressed recombinantly in *E. coli* SHuffle™ cells (NEB, Ipswich, MA) as a thioredoxin fusion protein (GRN-3-trxA) as previously reported[166]. This fusion construct and cells were chosen for two distinct advantages: SHuffle™ cells are engineered to constitutively express protein disulfide bond isomerase (DsbC) in the cytoplasm which facilitates the correct disulfide bond formation and prevents disulfide bond scrambling[167] and the cells also carry the knockout mutations of the thioredoxin and glutathione reductase genes (*ΔtrxB, Δgor*) which help maintain an oxidative environment in the cytoplasm conducive to disulfide bond formation. Furthermore, to facilitate the spectroscopic characterization of GRN-3, a Y24W substitution was introduced in the sequence (Figure 2.10A). This substitution is conservative as all GRNs except GRN-3 and GRN-1 have a conserved Y at this position. After nickel affinity purification and thioredoxin cleavage by thrombin, GRN-3 was fractionated using a C18 reverse phase HPLC column. The sample fractionated in multiple fractions between 47 to 68, which indicates the presence of many isoforms in the protein (Figure 2.10B, dashed box, and Figure 2.10C). The cleaved thioredoxin (trxA) eluted at later fractions at ~90. Distinct and some well-resolved peaks were observed for fractions between 47 to 68 (Figure 2.10C). To confirm the purity, the molecular mass and disulfide bond integrity of the protein in the fractions between 47 and 68, SDS-PAGE analysis was conducted under both reducing and non-reducing conditions. As expected, a single band at about 6.3 kDa

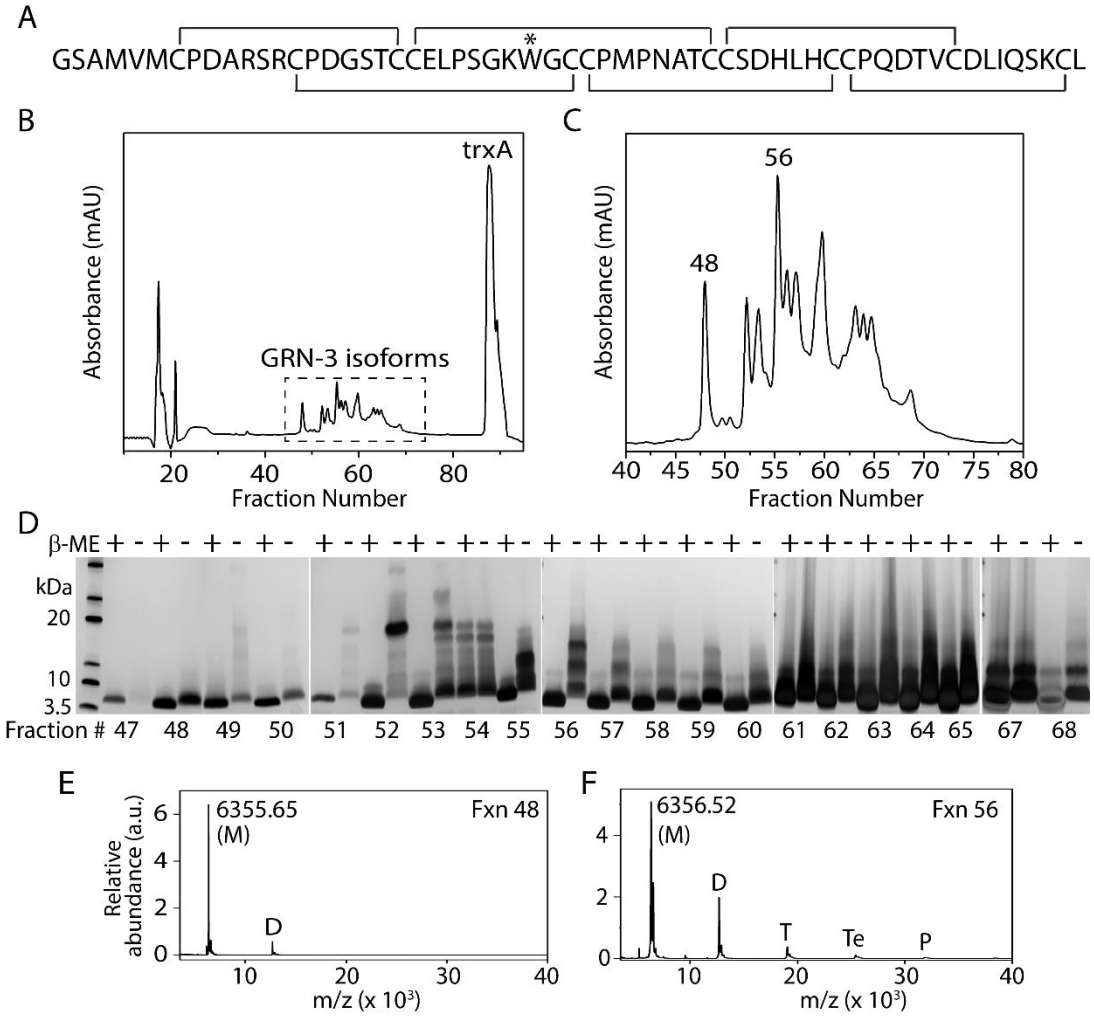

Figure 2.10 Characterization of GRN-3.

A, Primary amino acid sequence of GRN-3 with putative disulfide bonding pattern. The * represents the Y28W mutation. B, HPLC fractionation of GRN-3 after thrombin cleavage. The peaks corresponding to the different disulfide bond isoforms of GRN-3 are marked with a dashed box. C, Zoomed image of the different disulfide bond GRN-3 isoforms showing distinctly resolved isoforms. Two of the fractions have been labeled for representation purposes. This HPLC profile is representative of three or more consistent repeats. D, SDS-PAGE analysis of the HPLC fractions 47 to 65, 67, & 68 under reducing (βME +) and non-reducing (βME -) conditions. The numbers indicated below the gels are the corresponding fraction numbers. Of all the fractions, fraction 48 shows a single band under reducing and non-reducing conditions corresponding to the GRN-3 monomer (Mw = 6.3 kDa) whereas fraction 56 shows a single band corresponding to GRN-3 monomeric and bands corresponding to the GRN-3 monomer, dimer, and trimer. E, & F, MALDI-ToF spectra of fractions 48 showing a predominant signal corresponding to GRN-3 monomer (M) and a relatively minor peak corresponding to the dimer (D) and fraction 56 showing signals corresponding to the monomer (M), dimer (D), trimer (T), tetramer (Te), and Pentamer (P).

was observed under reducing conditions in all the fractions corresponding to the average mass of monomeric GRN-3 (Figure 2.10D, lanes β-ME +). In addition to monomeric band, bands corresponding to dimeric (~12.7 kDa) and/or trimeric (~19.1 kDa) GRN-3 were also observed for all the fractions, expect for fraction 48, under non-reducing condition (Figure 2.10D, lanes β-ME -), indicating that these fractions primarily contain intermolecularly disulfide-bonded multimers. Fraction 48 is the only one that indicated monomeric protein containing intra-molecular disulfide bonds. Although a faint smear could be observed for fraction 48 under non-reducing condition, the percentage of a dimer is negligible as compared to the other fractions. MALDI-ToF mass spectrometric analysis of fraction 48 showed a predominant signal at m/z value of 6355.65 Da (M), which corresponds to the molecular weight of monomeric GRN-3 along with a relatively minor signal corresponding to dimeric GRN-3 (D) indicating presence of less than 10% of dimeric GRN-3 (Figure 2.10E). In contrast, the mass spectrum of fraction 56 showed signals at m/z values of corresponding to monomer or 6356.52 Da (M) along with those corresponding to a dimer (D), trimer (T), tetramer (Te), and a pentamer (P) (Figure 2.10F). Similar multimeric peaks were observed in all the fractions between 49 and 68 (Figure 2.11A). To further confirm the integrity of disulfide bonds, Ellman's assay and alkylation assay using iodoacetamide were performed. Freshly purified GRN-3 and mGRN-3 samples indicated that <5% of the cysteines were in the reduced form, respectively, by Ellman's assay. The iodoacetamide alkylation confirmed that only 1 – 2 cysteines were present as free sulfhydryls (Figure 2.11B). Fraction 56 was chosen as mGRN-3 for further analyses as it showed highest concentration among all other

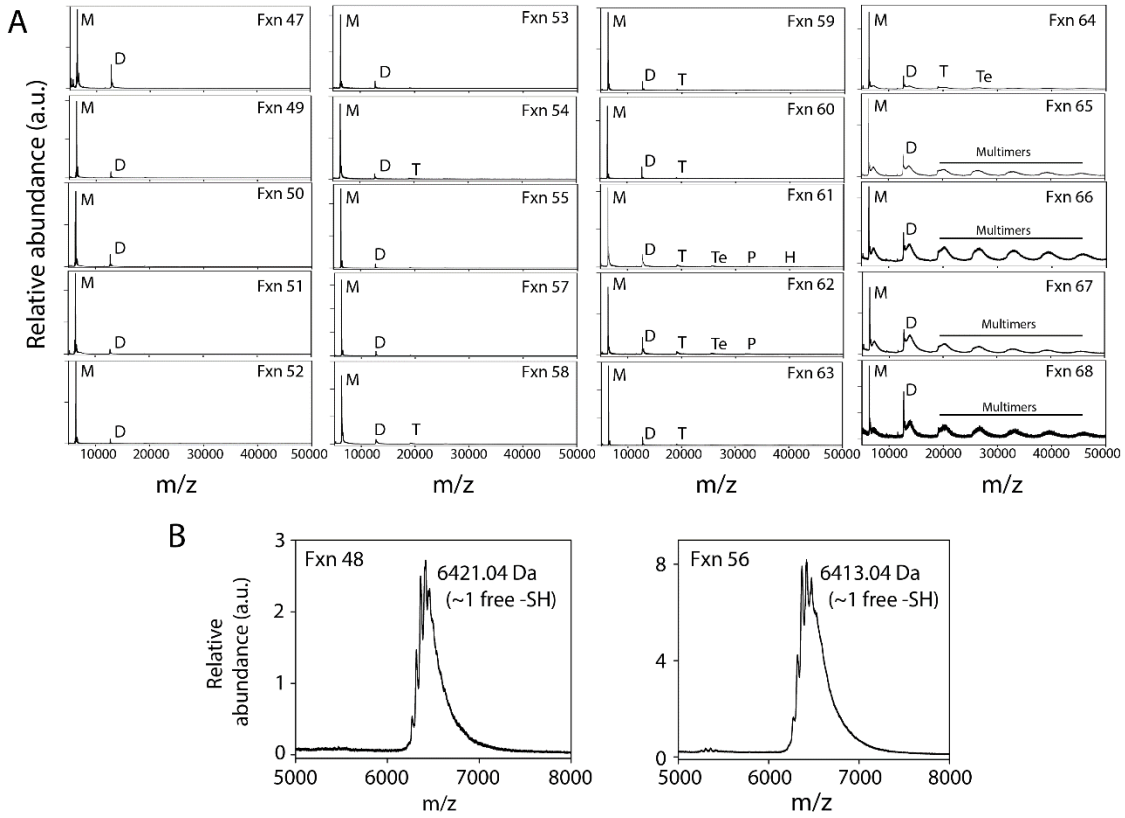

Figure 2.11 MALDI-ToF of fractions 47-68 and Alkylation of Fractions 48 and 56.

A, MALDI-ToF spectra of fractions 47 to 68 (other than 48 and 56) showing multimers. B, Iodoacetamide alkylation of fraction 48 and 56 showing ~1 free sulfhydryls each indicating presence of one free cysteine.

multimeric fractions. Thus, from the SDS-PAGE and MALDI-ToF analyses, it was apparent that the native GRN-3 elutes exclusively at fraction 48. Quantitation of fraction 48 as compared to overall GRN-3 expression between fractions 47 to 68 showed that the monomer only accounted for 5% of the total protein expressed. Despite the presence of thioredoxin and oxidized environment provided by the SHuffle^{TM} cells, *E. coli* seems to be incapable of generating correct disulfide bonded protein, likely due to the high cysteine content as well as the placement of cysteines (multiple adjacent positions) in GRN-3 (Figure 2.10A).

2.6.2 GRN-3 Expressed in Human Embryonic Kidney (HEK) Cells Also Form Multimers with Intermolecular Disulfide Bonds.

We reasoned that the inability of *E. coli* to express GRN-3 with correct intra-molecular disulfide bonds could be due to the ineffectiveness of rudimentary post-translational processing machinery in *E. coli* that is incapable of generating correct disulfide bonds for a protein with high cysteine content. Therefore, to address this, GRN-3 was expressed and purified from human embryonic kidney (HEK) cells to assess if the mammalian post-translational machinery will assist in the formation of intramolecularly disulfide bonded, monomeric GRN-3. Expression and the purification of GRN-3 from HEK cells, referred to as hGRN-3 henceforth was performed in our collaborator, Dr. Thomas Kukar's lab at Emory university. hGRN-3 was subjected to SDS-PAGE and MALDI-ToF analyses similar to those generated in *E. coli*. SDS-PAGE, under reducing conditions, showed a distinct band at ~ 12 kDa corresponding to monomeric hGRN-3 along with a smear between 15 and 20 kDa (Figure 2.12A, lane 1). The smear may reflect the glycosylated form of the protein. In the absence of heat treatment, the sample did not show much change in the banding pattern suggesting the bands observed arise due to covalent interactions, that is, inter-molecular disulfide bonds (Figure 2.12A, lane 3). hGRN-3 sample electrophoresed under non-reducing conditions both with and without heat treatment largely showed a faint band corresponding to monomeric (single arrow), predominant band corresponding to dimeric (double arrow), and another faint band corresponding to trimeric (triple arrow) hGRN-3, which was absent in the reduced samples (Figure 2.12A, lanes 2 and 4). Thus, the SDS-PAGE analysis suggests that

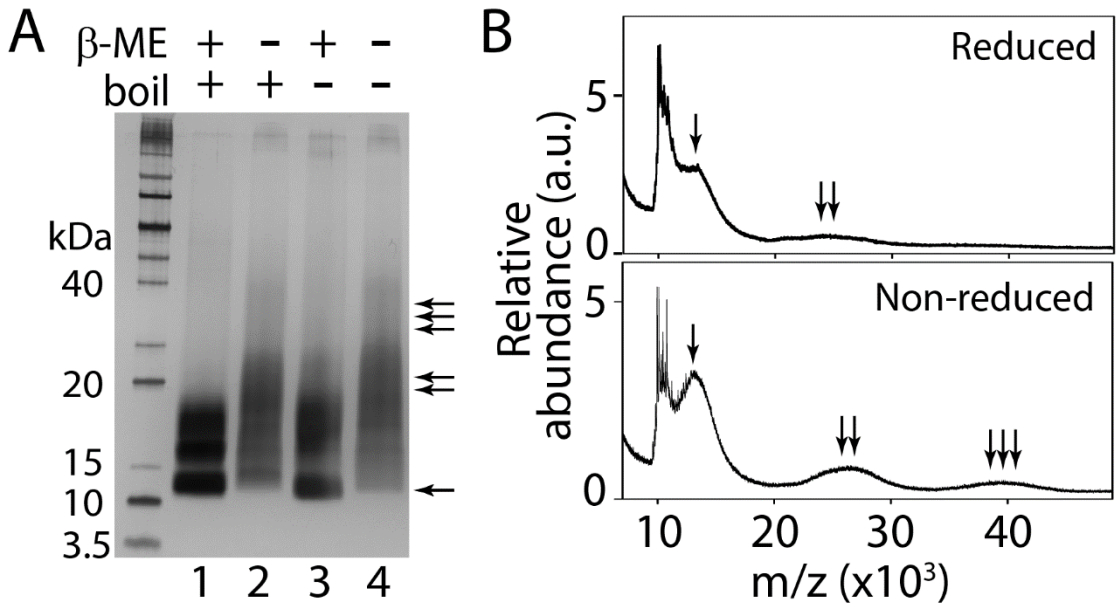

Figure 2.12 Characterization of hGRN-3 expressed and purified from human embryonic kidney (HEK) cells.

A, SDS-PAGE of hGRN-3 under reduced and non-reduced and boiled (lanes 1 and 2, respectively) and reduced and non-reduced and not boiled (lanes 3 and 4, respectively). The presence of monomer, dimers, and trimers in lanes 2 are marked with single, double, and triple arrows, respectively. B, MALDI-ToF spectra of hGRN-3 showing signals corresponding to monomeric hGRN-3 (single arrow), dimeric hGRN-3 (double arrows), and trimeric hGRN-3 (triple arrows and that of reduced hGRN-3 showing predominant signal corresponding to monomeric hGRN-3 (single arrow) and a relatively minor peak corresponding to dimeric hGRN-3 (double arrows). The results are indicative of three consistent repeats.

hGRN-3 forms multimers arising from intermolecular disulfide bonds. Similarly, the MALDI-ToF spectrum of hGRN-3 under reducing conditions showed the presence of a predominant monomeric peak (Figure 2.12B, single arrow) along with a relatively minor dimeric peak (Figure 2.12B, double arrow). In contrast, under non-reducing conditions, distinct signals corresponding to dimers (Figure 2.12B, double arrow) and trimers (Figure 2.12B, triple arrow) in addition to the monomeric signal (Figure 2.12B, single arrow) were observed. The possibility of multimers arising from non-covalent interactions is eliminated by the presence of identical banding pattern between heat-treated and untreated samples. These data unambiguously indicate that hGRN-3 expressed in

mammalian cells also forms multimers with inter-molecular disulfide bonds. Thus, these results along with the results from expression in *E. coli* show that irrespective of cell type, the post-translational machinery seems to inefficient in generating homogenous disulfide bonds in GRN-3. The only thing that may vary between GRN-3 from *E. coli* and hGRN-3 from HEK cells is the extent of multimers present. Since the GRN-3 expressed and purified from the HEK cells was largely similar to that from E. coli, and due to the limitation in the amount of protein produced in HEK cells for biophysical analyses, *E. coli* expressed protein was used primarily for further analyses.

2.6.3 GRN-3 is More Ordered than mGRN-3 and rGRN-3

To discern the role of disulfide bonds in determining the structure of GRN-3, we used ^{1}H-^{15}N heteronuclear multiple quantum coherence (HMQC) NMR and CD spectroscopy to probe the structure of GRN-3 and compared it with that of mGRN-3 and rGRN-3. The HMQC spectrum of GRN-3 showed well-resolved resonances with good spectral dispersion between 6.8 & 9.5 ppm and 104 & 130 ppm on the ^{1}H dimension and $1^{5}N$ dimensions, respectively (Figure 2.13A, GRN-3). The resonances for all the backbone amides and side chain amide nitrogens, except for the 6 proline residues, present in the GRN-3 sequence (Figure 2.10A) could be accounted. The broad signals observed at 7.4 and 7.8 ppm on the ^{1}H scale and at 104 and 109 ppm on the ^{15}N scale, respectively can potentially be attributed to the two arginine and lysine residues.[168-170] The peaks at 7.0 and 129 ppm are negative peaks arising from potential contaminants. The well spread-out spectral dispersion in both the proton and the nitrogen dimensions indicate a well-defined structure for GRN-3 and though the HMQC data is not sufficient to discern its structure, the overall spectrum resembles that of a β-sheet containing

protein. The spectrum of mGRN-3, on the other hand, was less dispersed as compared to that of GRN-3 in the proton dimension, however, majority of the residues displayed well-resolved resonances (Figure 2.13A, mGRN-3). Nevertheless, some overlapping resonances were observed between 8 and 8.5 ppm suggesting that mGRN-3 has a partly folded structure with certain parts resembling a collapsed molten globule containing the hydrophobic residues. Perhaps, the scrambling of disulfide bonds forming intermolecular links causes the protein to resemble a molten globule type structure. The NMR results of GRN-3 and mGRN-3 and those of rGRN-3, which is completely disordered (detailed in section *2.2.3*), indicate that disulfide bonds play a crucial and major part in determining the structure of GRN-3.

To further bolster the NMR data the samples were analyzed by far-UV CD spectroscopy. Surprisingly, the far-UV circular dichroism (CD) spectroscopy of GRN-3 showed the protein to be largely disordered as indicated by the canonical random coil CD spectrum with a strong minimum at 198 nm and a weak minimum at 225 nm commonly observed for disordered proteins (Figure 2.13B, solid line). A near identical CD spectrum was observed for rGRN-3 (Figure 2.13B, short dash) as previously reported.[166] This is an interesting observation considering the high cysteine content (20%) within the protein. mGRN-3 displayed a spectrum which is typical of a poly proline type II (PPII) helix with a minimum at 201 nm and a less intense maximum at ~230 nm (Figure 2.13B, dash).[171, 172] It is increasingly common to observe PPII conformational for IDPs[173-176], due to similar arrangement of amide dipoles within their geometries.[177] The observations are more evident from the residual spectra of GRN-3 (Figure 2.13C, solid line) and mGRN-3 (Figure 2.13C, dashed line) obtained after subtracting the rGRN-3 spectrum. The dotted

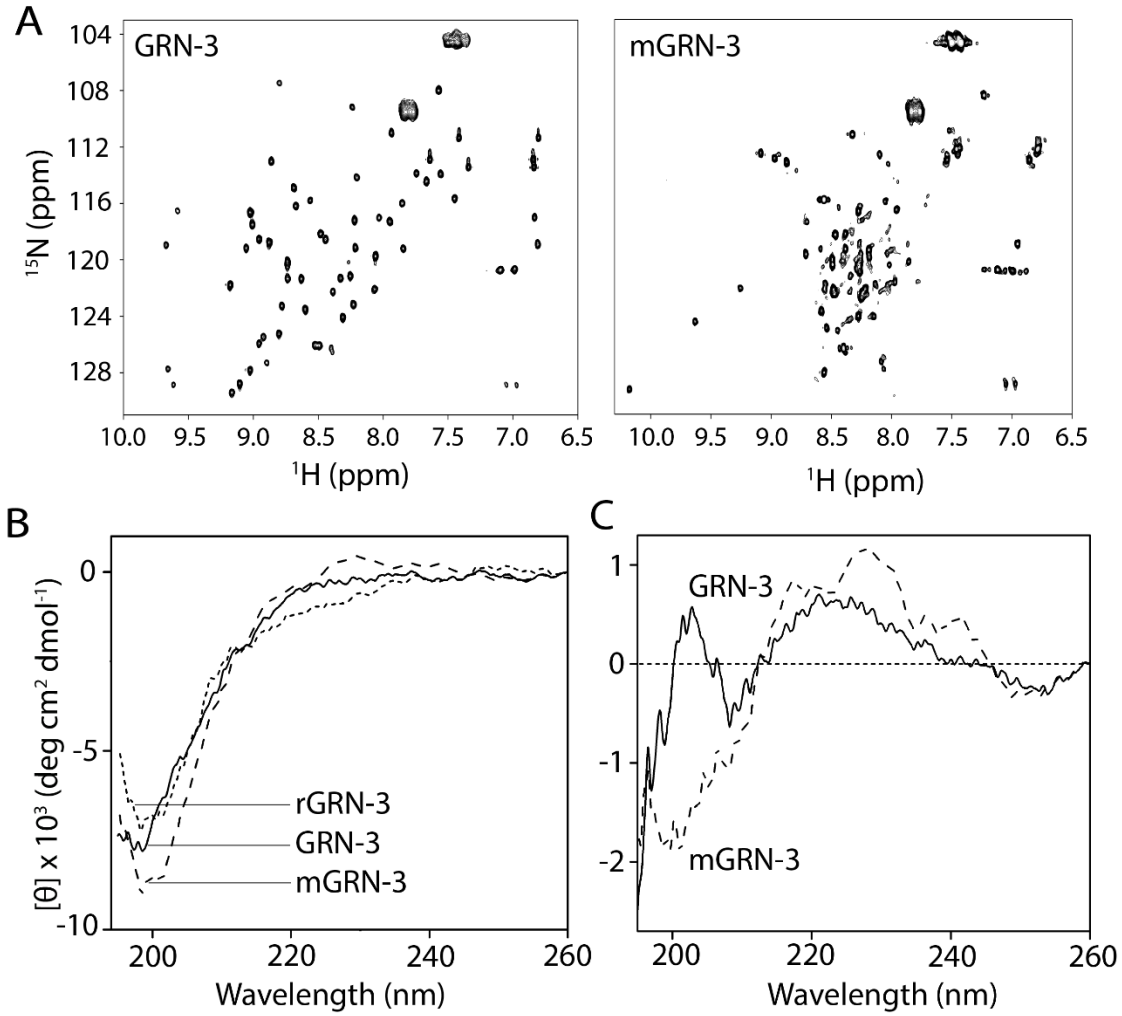

Figure 2.13 Structural Characterization of GRN-3, and mGRN-3.

A, ^{1}H-^{15}N SoFast HMQC NMR spectra of GRN-3, and mGRN-3. B, Far-UV circular dichroism (CD) spectra of native GRN-3 (solid line), mGRN-3 (dashed line), and rGRN-3 (short dashed line). Both GRN-3 and rGRN-3 show minima at 198 nm typical of random coil whereas mGRN-3 shows a minimum at 202nm and a maximum at ~230 nm corresponding to a PP2 helix. C, Residual spectra for GRN-3 (solid) and mGRN-3 (dash) after subtracting the CD spectrum of rGRN-3. The line at 0 (short dash) is the baseline obtained by zero correcting rGRN-3 spectrum.

line at 0 in Figure 2.13C is the baseline obtained by zero-correcting rGRN-3 spectrum. The potentially conflicting observations from NMR and CD data for GRN-3 can be explained from the fact that disulfide bonds, which if present in a ladder-like arrangement as observed in GRN4[100], hold the loops such that the protein backbone show minimal

conformational freedom. This may show distinct magnetic environment responsible for a good spectral dispersion in NMR yet, the backbone amide dipoles are not in a typical β-sheet environment to display $\pi \rightarrow \pi^*$ transition at 216 nm in CD. These findings seem to indicate that although disulfide bonds are important to induce structural order in GRN-3, they do not induce the formation of canonical secondary structures but rather disordered loops that are dynamic.

2.6.4 mGRN-3 has More Solvent-Exposed Hydrophobic Surfaces as Compared to GRN-3

To evaluate the structural differences in GRN-3 and mGRN-3, the solvent-exposed hydrophobic surfaces were qualitatively estimated the using 8-anilino-1-naphthalene sulfonic acid (ANS). ANS is an extrinsic dye which exhibits weak fluorescence in polar environments but shows strong fluorescence with a distinct blue shift in its emission wavelength upon binding to the solvent-exposed hydrophobic residues of proteins.[178] ANS has been widely used to study protein folding/unfolding and structure of the molten globule states.[179] Upon incubating 25 μM GRN-3 or mGRN-3 with 500 μM ANS, the fluorescent intensity with mGRN-3 was significantly higher than that with GRN-3 (Figure 2.14A). This indicates that mGRN-3 has more solvent-exposed hydrophobic surfaces than GRN-3. This evaluation is in agreement with the ^{1}H-^{15}N HMQC NMR data which shows mGRN-3 to be more disordered and collapsed as compared to GRN-3 (Figure 2.13A). In addition, the solvent accessibility of the single tryptophan residue (W28) in GRN-3 was examined using Stern-Volmer analysis where the fluorescence of the W residue was monitored with the increasing concentration of a quencher (acrylamide). A significant deviation from linearity was observed in case of

GRN-3 (Figure 2.14B, ●) indicating that tryptophan undergoes dynamic quenching indicative of the probe being solvent exposed[155], whereas, the deviation observed in case of mGRN-3 was relatively insignificant (Figure 2.14B, ○). Thus, the solvent accessibility of W28 is more in GRN-3 than it is in mGRN-3, perhaps, due to more collapsed structure of mGRN-3 the W residue may be buried inside the hydrophobic core.

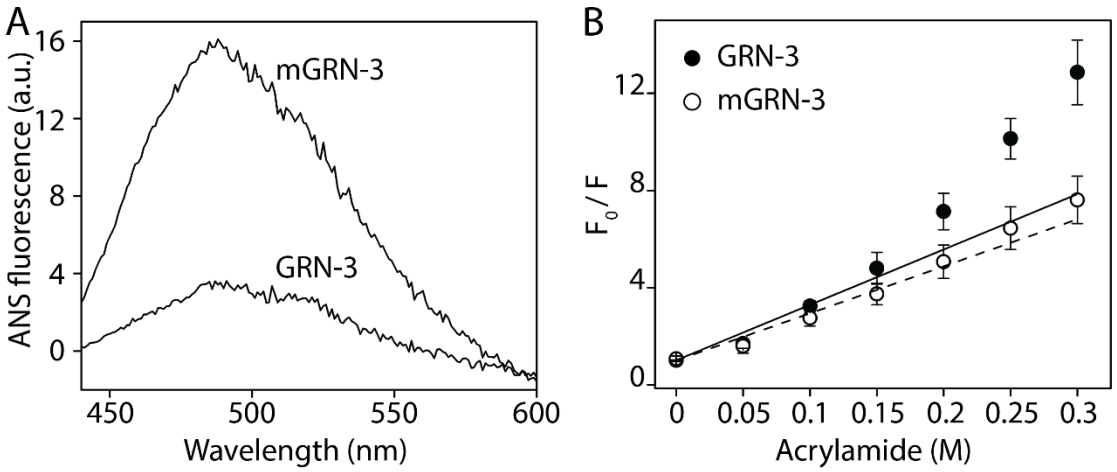

Figure 2.14 Structural differences between GRN-3 and mGRN-3.

A, Differential interaction of 8-anilino-1-naphthalene sulfonic acid (ANS) to GRN-3 and mGRN-3 at 25 μM, indicating differences in the exposed hydrophobic surfaces in GRN-3 and mGRN-3. B, Stern-Volmer plot of GRN-3 (●) and mGRN-3 (○) using acrylamide as the quenching agent.

2.6.5 Disulfide Bonds Contribute to the Overall Stability of GRN-3.

To obtain specific insights into the role of disulfide bonds in the structure and stability of GRN-3, the protein was subjected to detergent-induced thermal denaturation. It is known that high concentrations of SDS (> 1%) induce rod-like or necklace like structures to polypeptides that a largely exhibit an α-helical structure[180-182]. It has also been shown that SDS-induced thermal denaturation of proteins that lack significant secondary structure to α-helical structures, is a convenient way to monitor stability by CD[183]. Therefore, GRN-3, mGRN-3 or rGRN-3 samples were denatured with 1% SDS

(35 mM) and the conversion from the random coil to helical structure was monitored as a function of temperature by CD spectroscopy. As expected, largely disordered rGRN-3 instantly melted into an α-helix in presence of SDS prior to the heat treatment at 10 °C (Figure 2.15A, rGRN-3, dotted line) and remained largely α-helical over the temperature range up to 90 °C (Figure 2.15A and Figure 2.15B, Δ). GRN-3, on the other hand, showed no appreciable changes in the random coil structure at 10 °C, and it remained in largely disordered form up to 90 °C (Figure 2.15A, GRN-3, dotted line and Figure 2.15B, ■), with only a small deviation from the characteristic random coil to a spectrum towards α-helical structure with a minimum at 207 nm and a decrease at 220 nm (Figure 2.15A, GRN-3, dashed line, and Figure 2.15B, ■). A similar response was observed for mGRN-3 with the protein remaining as largely disordered throughout the temperature range (Figure 2.15A and Figure 2.15B, ○). It is clear that both GRN-3 and mGRN-3 resist denaturation by SDS and remain disordered even with the increase in the temperature exhibiting robust thermal stability, a rather unusual characteristic of IDPs. Perhaps, this can be attributed to the presence of six intramolecular disulfide bonds in GRN-3, which resist the formation of 'necklace' or 'rod-like' helical structures known when SDS interacts with polypeptides[180-182, 184]. If disulfide bonds are the main reason for the structural stability, abrogation of these should make the protein amenable to denaturation, which is precisely what is observed with rGRN-3. Secondly, in light of high stability of GRN-3 and mGRN-3 for SDS denaturation, we wanted to see whether this stability reflects in electrophoretic mobility. As observed earlier (Figure 2.10C, fraction 48), under both reducing and non-reducing conditions with heat treatment (boiling the sample with 1% SDS for five minutes), GRN-3 electrophoreses as a single band at 6.3 kDa

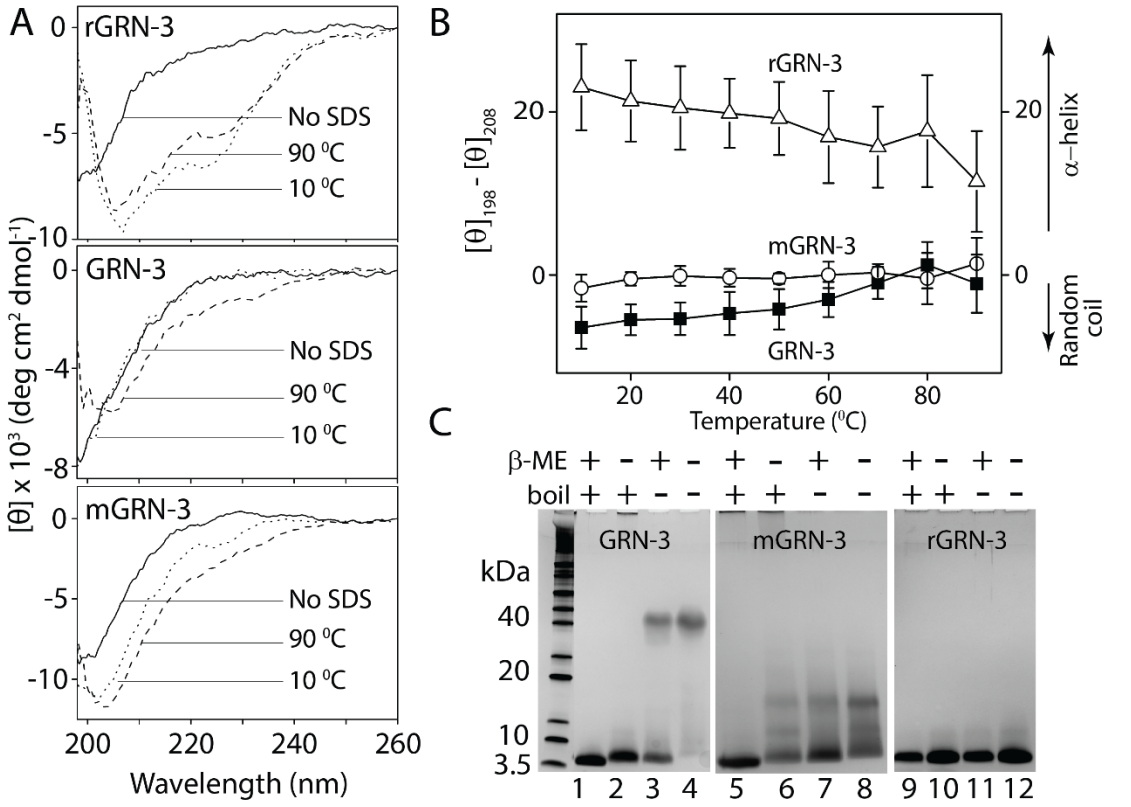

Figure 2.15 Structural Stability of GRN-3, mGRN-3, and rGRN-3.

A, Far-UV CD spectra of GRN-3, mGRN-3, and rGRN-3 without SDS (solid line) and in presence of 1 % SDS at 10 °C (dotted line), and 90 °C (dashed line). B, Difference in 198 nm (random coil) and 208 nm (α-helix) for GRN-3 (■), mGRN-3 (○), and rGRN-3 (Δ) plotted against increasing temperature in presence of 1% SDS. C, SDS-PAGE of GRN-3, mGRN-3, & rGRN-3 under reduced and non-reduced with heat treatment (lanes 1, 2, 5, 6, 9, & 10, respectively) and reduced and non-reduced without the heat treatment (lanes 3, 4, 7, 8, 11, & 12, respectively).

corresponding to the molecular weight of monomeric GRN-3 (Figure 2.15D, lanes 1 and 2). However, both under reducing and non-reducing conditions but without the heat treatment, a band is observed between 40 and 50 kDa GRN-3 (Figure 2.15D, lanes 3 and 4). Furthermore, in the presence of the reducing agent (βME), additional monomeric band was observed, which was absent in the βME untreated sample, reinforcing the inference that disulfide bonds are solely responsible for the stability and abnormal electrophoretic mobility of GRN-3. This unusual electrophoretic mobility was not observed in case of

mGRN-3 or rGRN-3 (Figure 2.15D, lanes 5 to 12) even though both mGRN-3 and rGRN-3 are more disordered than GRN-3 for reasons that remain uncertain. Many IDPs are notorious for their display of unusual mobility during electrophoresis, which is largely attributed to the reduced SDS binding and shape of the SDS-protein complex[9]

2.7 Discussion and Conclusions

The primary objective of this study was to identify the role of six disulfide bonds in the structure and dynamics of GRN-3 by investigating the structure of native GRN-3. In this context, the results presented here indicate that disulfide bonds play an intriguing role in inducing structural stability to the protein and raise some interesting aspects about the role of disulfide bonds in structural plasticity among IDPs. First, both *E. coli* and HEK cells are ineffective in making correct disulfide linkages indicated by the incapacity of both the cell types to generate intramolecularly disulfide bonded monomers exclusively. In *E. coli*, only 5% of the total protein expressed is monomeric while the remaining 95% forms different multimers with scrambled inter-molecular disulfide bonds, despite, the presence of thioredoxin tag and the oxidative environment of the engineered *E. coli* cells used for the expression. Surprisingly, even the mammalian (HEK) cells show some level of scrambled multimers and seem to be fully effective in generating monomers exclusively, in spite of having the adequate post-translational machinery required to form correct disulfide bonds. One plausible reason for this could be the high cysteine content of GRN-3 (20%) and the location of cysteines (four pairs of adjacent cysteines in the center with two single cysteines at each terminus; Figure 1.3) within its sequence. This unique arrangement could decrease the fidelity of protein disulfide isomerases (PDIs) to catalyze formation of correct disulfide bonds. Moreover,

in cells GRNs are produced by the proteolytic cleavage of their precursor, PGRN which could further exacerbate the complications in disulfide bonds formation as PGRN has 90 cysteines forming 45 disulfide bonds (7.5 tandem repeats of GRNs; Figure 1.3). Indeed, disulfide bonded multimeric isoforms of PGRN have been reported previously in HEK cells.[185]

The second interesting inference that can be drawn from this study is that the disulfide bonds solely dictate the structure of GRN-3 and depending upon whether the bonds are scrambled or absent altogether the protein is either partly disordered or completely disordered. The 2D-NMR HMQC data along with the other biophysical evidence presented in section *2.2.3* confirms rGRN-3 to be intrinsically disordered. Interestingly, the HMQC data also suggests that mGRN-3, with scrambled disulfide bonds, is largely disordered but shows more degree of order as compared to rGRN-3. In contrast, monomeric GRN-3 shows significant spectral dispersion suggestive of a well-defined structure for the protein. These findings confirm our hypothesis that ***the structure of GRN-3 is mainly dictated by the six intra-molecular bonds and the scrambling or the abrogation of the disulfide bonds result in a protein with partial or complete loss of structure.*** However, the CD data suggests that GRN-3 is unstructured as indicated by the random coil spectrum commonly observed for disordered proteins. rGRN-3 also shows an identical CD spectrum. This discrepancy in the NMR and the CD data could, perhaps, arise from the arrangement of the disulfide bonds in GRN-3 structure and the way they stabilize the disordered structure. The possibility of the conserved cysteines in GRN-3 forming a ladder-like disulfide bond arrangement as observed for GRN4 (Figure 2.16A, dark grey)[100] is high even though GRN-3 shows only 55% sequence identity with GRN-4.

In fact, the GRN-3 structure predicted using the I-TASSER structure prediction tool[186, 187] (Figure 2.16B, light grey), aligns with the GRN4 structure with root mean square deviation (rmsd) score of 1.02 over 56 residues (Figure 2.16C) suggestive of similar structure at least at the N-terminus.

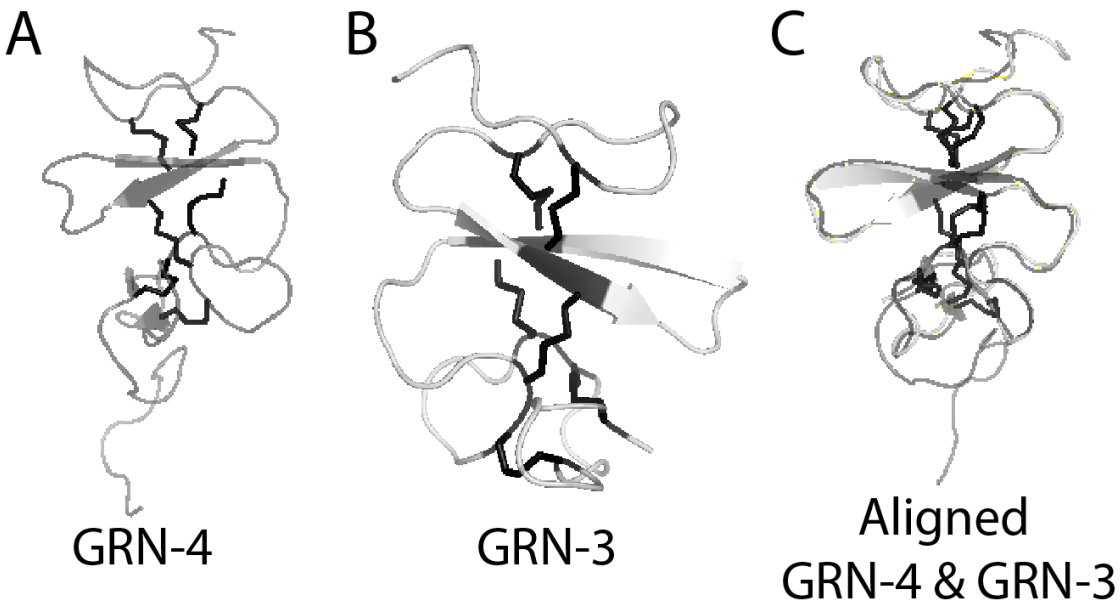

Figure 2.16 Structure alignment of Grn4 and GRN-3.

A, Solution NMR structure of Grn4 (pdb – 2jye) with disulfide bonds shown as black sticks. B, GRN-3 structure predicted based on the primary amino acid sequence using the I-TASSER prediction tool with predicted disulfide linkages shown in black C, Alignment of Grn4 and GRN-3 structures performed using PyMol; dark grey is Grn4 and light grey is GRN-3. Disulfides bonds are shown as black sticks.

From this alignment, it can be assumed that the structural order in GRN-3 is mainly achieved by the disulfide bonds that from the fulcrum to the structure stabilizing the loops surrounding them. Such a structure has minimal secondary structure content (only short segments of β-strands are observed in GRN-4 or GRN-3) and the conformational freedom of the loops seems to be curtailed by the central shaft made of disulfide bonds. The other family of proteins bearing closest resemblance to a disordered structure stabilized by disulfide bonds include the epidermal growth factor domain containing

proteins like the epidermal growth factor (EGF), and transforming growth factor α (TGF-α)[92, 188], and the kringle domain-containing family of proteins such as the hepatocyte growth factor[96], proteases involved in blood clotting like prothrombin, and plasminogen[97], apolipoprotein[98], and tissue plasminogen activator.[99] Both the EGF domain and kringle domains are characterized by disordered loops with minimal well-defined secondary structure stabilized by three disulfide bonds.

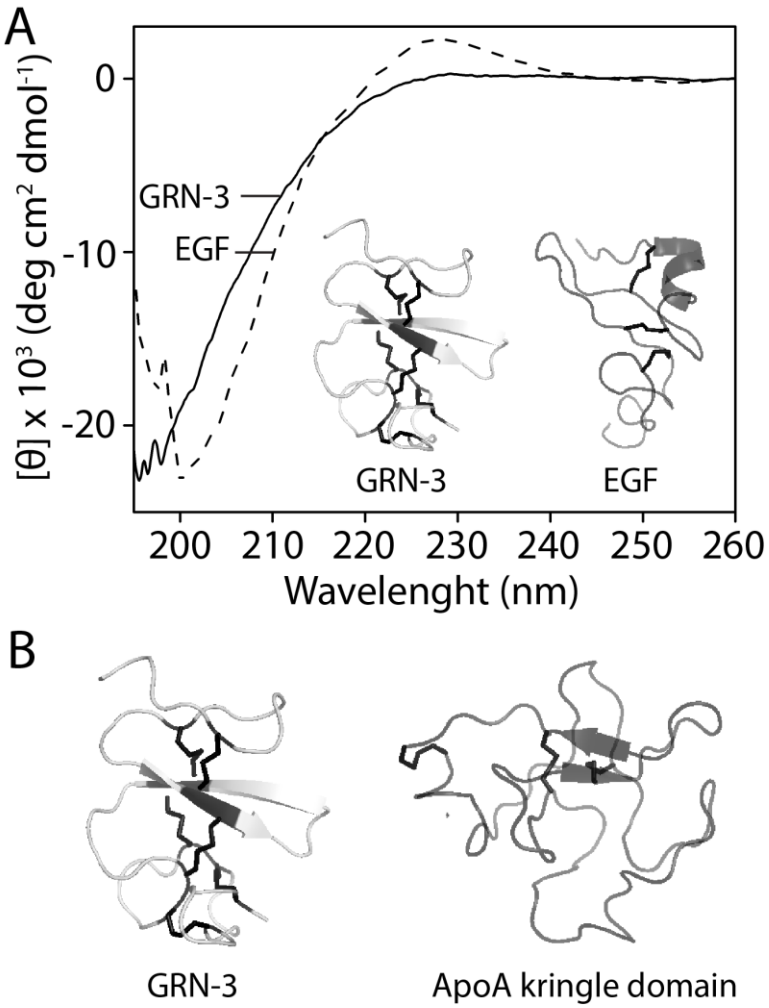

Figure 2.17 Structural fold similarity between GRN-3, EGF, and ApoA kringle domain.

A, Similarity between far-UV CD spectrum of GRN-3 (solid line) and human EGF (dashed line). *Inset*, Structural fold similarity between the predicted structure of GRN-3 and solution NMR structure of EGF (pdb – 2kv4). B, Structural fold similarity between predicted GRN-3 structure and ApoA kringle domain (pdb - 4bvd).

The murine EGF exhibits a striking resemblance to the unique stacked β-sheet domain observed for the N-terminal domain of GRN4 (Figure 1.5A). The comparison of the far-UV CD spectra of GRN-3 and that of human EGF showed striking resemblance, with the latter showing the PP2-helix profile (Figure 2.17A). The HSQC spectrum of human EGF shows well-dispersed resonances[189] whereas the CD spectrum indicates PP2-helix similar to what observed for GRN-3. Further, the predicted structure of GRN-3 and the solution NMR structure of human EGF (pdb – 2kv4)[189] show similar structural fold (Figure 2.17A, inset). Additionally, the kringle domain of ApoA also has similar structural fold (Figure 2.17B).

Though this study establishes the vital role of disulfide bonds in the structure of GRN-3, it raises questions on their necessity and their inability to induce secondary structure in the protein. From the thermal stability data, it is clear that disulfide bonds, alone, impart a remarkable thermal stability to GRN-3. Perhaps, it can be speculated that the fulcrum of disulfide bonds holds the loops in place imparting stability to an otherwise flexible protein but maintain some degree of structural plasticity. Further, this partial plasticity could potentially be responsible for the multifunctional roles of IDPs. Such pluripotent structures of IDPs leading to multifunctional roles are now well established.[9, 152, 165] This study brings forth some interesting aspects of the role of disulfide bonds in GRN-3 structure; the most striking of which is the delicate handshake between disulfides and disorder towards maintaining stability and plasticity.

CHAPTER III - INTERACTIONS BETWEEN GRN-3 AND Aβ AND THEIR IMPLICATIONS IN AD PATHOLOGY

3.1 Hypothesis and Rationale

As detailed in section *1.4.1*, several evidences point towards the involvement of GRNs in AD. We hypothesize that **GRN-3 directly interacts with Aβ during acute inflammation and modulates the latter's aggregation and neuronal toxicity.** This chapter is focused on the interaction between GRN-3 and Aβ by biophysical methods and are detailed and discussed in the following sections.

3.2 Results

3.2.1 GRN-3 Directly Interacts with Aβ42 Monomers with a Moderate Binding Affinity.

To investigate the interactions between GRN-3 and Aβ42, tetra-methyl rhodamine (TMR) labeled Aβ was used as a fluorescence probe and increasing concentrations of GRN-3 were titrated on it. The concentration of TMR-Aβ was kept constant at 4 μM throughout the titrations. The samples were excited at 550 nm (excitation λ^{max} for rhodamine) and the changes in the fluorescence emission of rhodamine labeled Aβ42 upon titration of GRN-3 were monitored at 580 nm. The normalized fluorescence intensities expressed as fraction bound were plotted against the stoichiometry yielding an exponential binding isotherm (Figure 3.1, ●). The binding isotherm was fitted using the following two-site binding model (see equation below) to obtain two binding affinities, 80 nM, and 2500 nM.

$$y = \frac{B_{max1} * x}{K_1 + x} + \frac{B_{max2} * x}{K_2 + x}$$

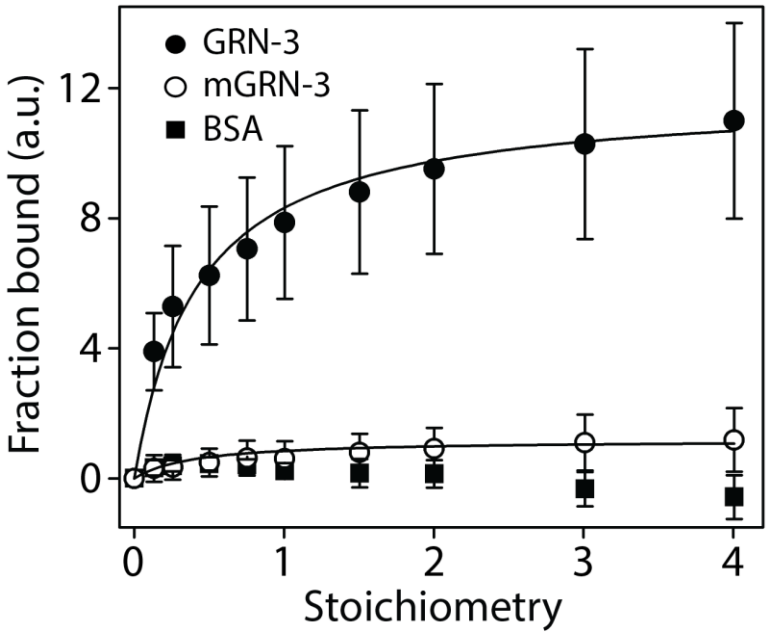

Figure 3.1 Binding interactions between GRN-3, mGRN-3, & BSA and TMR-Aβ42 monomer.

The binding isotherm is fitted with a two-site binding model.

where y is the fraction bound, x is the stoichiometry, B_{max1} and B_{max2} are the arbitrary parameters that are floated, and K_1 and K_2 are the binding constants for the two sites. Thus, from the two binding constants obtained, the binding affinity between GRN-3 and Aβ42 monomer is an order of magnitude stronger for one site as compared to the other. The binding interactions between mGRN-3 and TMR-Aβ42 were probed in a similar as described above. The response obtained from the titration of mGRN-3 indicated that the interaction between mGRN-3 and TMR-Aβ42 was significantly weaker as compared to that of GRN-3 (Figure 3.1, ○). BSA, the negative control used for the assay, didn't show any interaction with TMR-Aβ42 as expected (Figure 3.1, ■).

3.2.2 GRN-3 Accelerates Aβ42 Aggregation in a Concentration-Dependent Manner

The effects of GRN-3 and mGRN-3 on Aβ42 aggregation were monitored using thioflavin-T (ThT) fluorescence, immunoblotting, and far-UV CD. ThT is an extrinsic

fluorescent dye that shows an increase in its fluorescence intensities upon binding to the β-sheet rich Aβ aggregates. It is routinely used to monitor Aβ aggregation.[190] Freshly purified, aggregate-free Aβ42 monomers (20 μM) were incubated with sub-stoichiometric (4 μM), stoichiometric (20 μM), and super-stoichiometric (40 μM) concentrations of GRN-3 and mGRN-3 in 20 mM Tris, pH 6.5 and 50 mM NaCl at 37 °C under quiescent conditions. ThT fluorescence was measured at 12, 18, 24, 48, 72, and 96 h time points. Aβ42 co-incubated with super-stoichiometric concentration of GRN-3 showed accelerated aggregation within first 12 h of co-incubation as indicated by increase in the fluorescence intensity and the absence of the lag phase (Figure 3.2A, ▽) as compared to the Aβ42 control incubated and monitored under identical conditions (Figure 3.2A, □). Aβ co-incubated with stoichiometric concentrations (Figure 3.2A, ▲) of GRN-3 showed a slight increase in the fluorescence intensity, however, the lag time was similar to that of control Aβ. At sub-stoichiometric (Figure 3.2A, ●) concentration, the aggregation profile of co-incubated Aβ was identical to that of control for the first 24 h. Aliquots of the co-incubated samples were electrophoresed at 12 and 24 h and immunoblotted using an Aβ specific antibody, Ab5, to assess if the increase in the ThT fluorescence for Aβ co-incubated with 40 μM GRN-3 was due to formation of high molecular weight aggregates. An intense band corresponding to a high molecular weight aggregate (> 260 kDa) was observed for Aβ co-incubated with 40 μM GRN-3 with concomitant decrease in the monomeric band between 3.5 and 10 kDa (Figure 3.2C, lane 4) after 12 h of co-incubation whereas no such band was observed for Aβ control and Aβ co-incubated with 4 and 20 μM GRN-3 (Figure 3.2C, lanes 1, 2, & 3, respectively). This indicates that the increase in the ThT fluorescence observed at 12 h for Aβ co-incubated

with 40 μM GRN-3 was indeed due to formation of Aβ aggregates. After 24 h, a high molecular weight band was observed for Aβ co-incubated with all three concentrations of GRN-3, however, the intensity of the band was highest for 40 μM GRN-3, followed by 20 μM, and least for 4 μM GRN-3. A faint aggregate band was also observed for Aβ control.

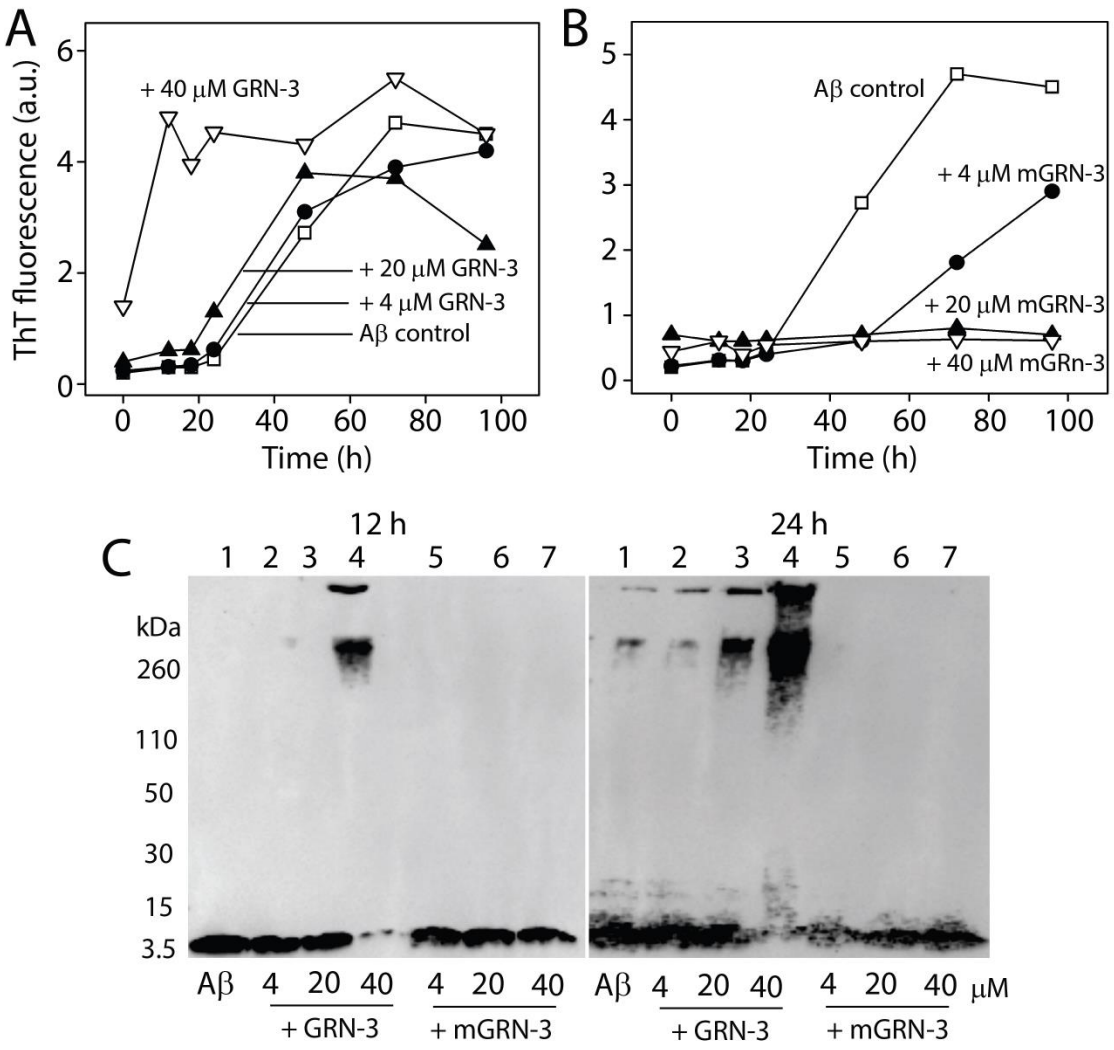

Figure 3.2 Effect of GRN-3 on Aβ42 aggregation.

Over time ThT fluorescence measurements of 20 μM Aβ42 alone (□) and Aβ42 co-incubated with 4 μM (●), 20 μM (▲), and 40 μM (▽) GRN-3 (A) and 4 μM (●), 20 μM (▲), and 40 μM (▽) mGRN-3 (B) in 20 mM Tris, pH 6.5 and 50mM NaCl at 37 °C under quiescent conditions. C, Immunoblots of 20 μM Aβ42 alone and Aβ42 co-incubated with 4 μM, 20 μM, and 40 μM GRN-3 and mGRN-3 at 12 h and 24 h time-points.

In contrast, Aβ co-incubated with same concentrations of mGRN-3, as GRN-3, did not show any increase in the ThT fluorescence (Figure 3.2B) and no aggregate band was observed for the co-incubated samples on the immunoblot at 12 h and 24 h time point (Figure 3.2C, lanes 5, 6, & 7). Since GRN-3 promoted aggregate formation within 12 h of coincubation, the possibility of GRN-3 augmenting Aβ42 aggregate formation before 12 h was investigated by co-incubating freshly purified 20 μM Aβ42 monomers with 40 μM GRN-3 and aliquots were electrophoresed after 1, 3, & 6 h of co-incubation. Interestingly, GRN-3 was able to promote formation of aggregates within 1 h of coincubation (Figure 3.3, lane 2) and the amount of the aggregate formed increased after 3 and 6 h of co-incubation as evident from the intensity of the band (Figure 3.3, lane 3 & 4, respectively). The Aβ42 monomer didn't aggregate within the experimental time frame (Figure 3.3, lane 1).

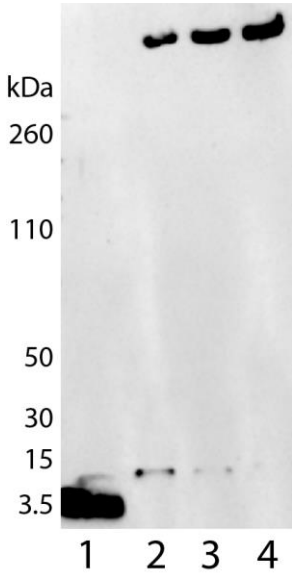

Figure 3.3 Time-dependent Aβ42 aggregation co-incubated with GRN-3.

Lane 1, 20 μM Aβ42 monomer alone after 6 h; *Lane 2*, 20 μM Aβ42 + 40 μM GRN-3 after 1 h; *Lane 3*, 20 μM Aβ42 + 40 μM GRN-3 after 3 h; *Lane 4*, 20 μM Aβ42 + 40 μM GRN-3 after 6 h.

Furthermore, the co-incubated samples were monitored via far-UV CD to investigate if the augmentation in aggregation is complemented by changes in the secondary structure of Aβ42 monomers from random coil to β-sheet. The control Aβ42 sample showed the random coil spectrum immediately after incubation i.e. at 0 h (Figure 3.4A, dashed line) and it remained random coiled even after 12 h (Figure 3.4A, dotted line) and 24 h (Figure 3.4A, solid line) of incubation at 37 °C. For Aβ42 co-incubated with 40 μM GRN-3, the spectrum was random coil at 0 h (Figure 3.4B, dashed line), however, after 12 h of incubation a slight negative minimum was observed at 216 nm indicating formation of β-sheet (Figure 3.4B, dotted line). The change can be better appreciated by the difference spectra (observed – control) shown in Figure 3.4B, inset, dotted line). This change in the secondary structure of Aβ co-incubated with 40 μM GRN-3 corroborates with the increased ThT fluorescence and aggregate band observed for this sample as detailed previously. The change was pronounced after 24 h of co-incubation with a distinct negative minimum at 216 nm and a positive maximum at 198 nm, typical of β-sheet structure observed for high molecular weight aggregates of Aβ (Figure 3.4B, solid line). The change is pronounced in the difference spectra (Figure 3.4B, inset, solid line). For Aβ co-incubated with 4 μM GRN-3, the change in the secondary structure was observed only after 24 h as seen in the difference spectrum (Figure 3.4C, inset, solid line) which also correlates with the high molecular weight band observed in the immunoblot (Figure 3.4C, 24 h, lane 3). Surprisingly, Aβ co-incubated with 4 and 40 μM mGRN-3 also showed a change in the secondary structure after 24 h but no high molecular weight aggregate band was observed in 24 immunoblot for both

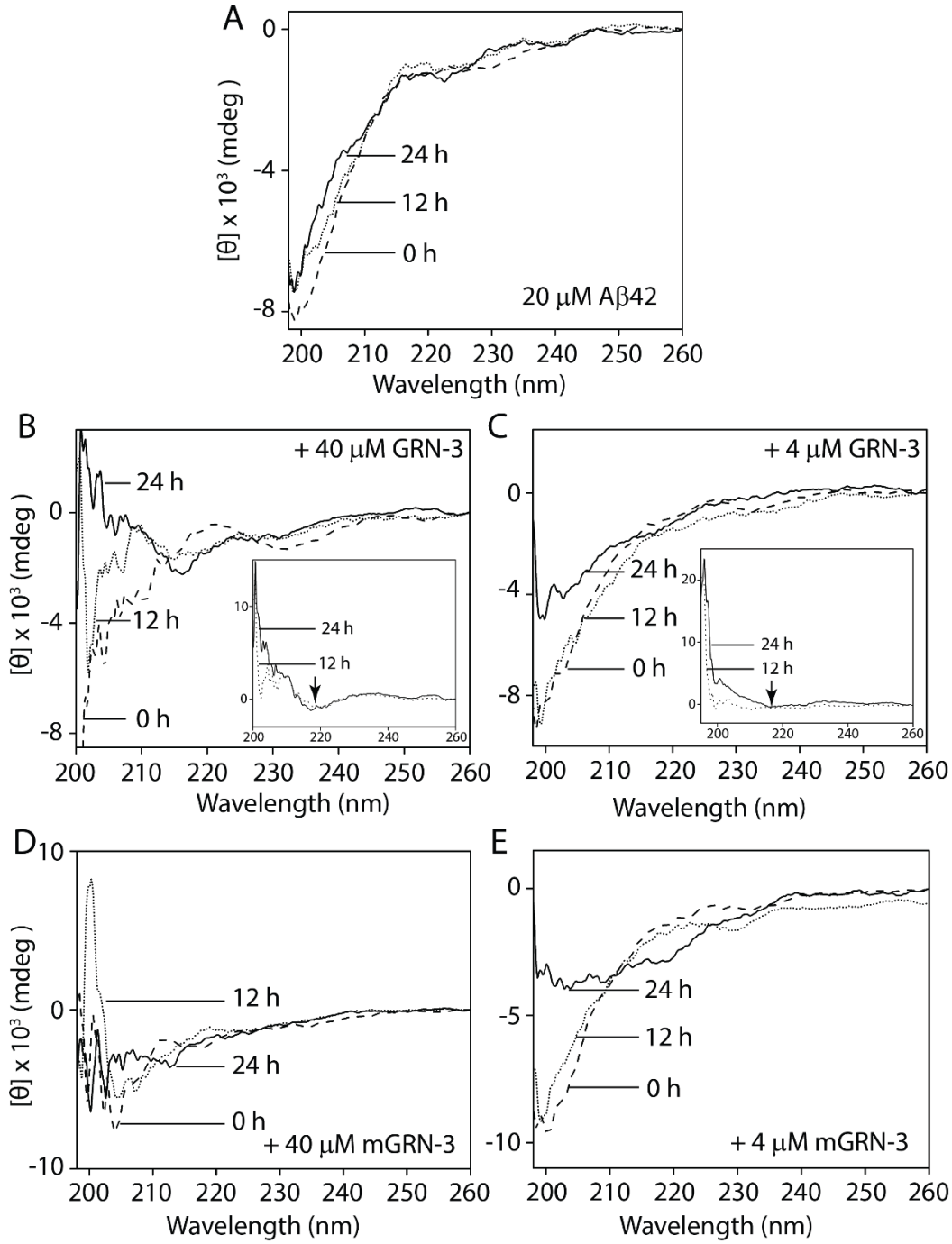

Figure 3.4 Changes in the secondary structure of Aβ42 co-incubated with GRN-3.

A, Far-UV CD spectrum of 20 μM Aβ42 incubated in 20 mM Tris, pH 6.5 and 50 mM NaCl at 0 (dashed line), 12 (dotted line), & 24 h (solid line) time-points. Far-UV CD spectrum of 20 μM Aβ42 at 0 (dashed line), 12 (dotted line), & 24 h (solid line) time-points, co-incubated with 40 μM GRN-3 B, 4 μM GRN-3 C, 40 μM mGRN-3 D, and 4 μM mGRN-3 E, The samples were incubated in 20 mM Tris, pH 6.5 and 50 mM NaCl at 37 °C under quiescent conditions. B, & C, inset, Difference spectra (observed – control)

the concentrations (Figure 3.4C, 24 h, lanes 5, 6, & 7). However, the spectra didn't show the typical β-sheet minimum at 216 nm but resembled an intermediate structure having both random coil and β-sheet type structures indicative of some intermediate formed along the aggregation pathway. These results indicate that GRN-3 augments aggregation of Aβ42 in a concentration-dependent manner in which super-stoichiometric concentrations abolish the lag time observed during canonical Aβ aggregation to promote the formation of high molecular weight aggregates.

3.2.3 GRN-3 Promotes High Molecular Weight Aggregates of Oligomers.

Aβ can aggregate to form fibrils via multiple different pathways generating non-canonical neurotoxic oligomers.[191-196] Large Fatty Acid Derived Oligomers (LFAOs), generated in our lab in presence of fatty acid interfaces are established as those formed along 'off-pathway'.[23] LFAOs are kinetically trapped along an alternate pathway that are incapable of converting into fibrils for an extended period of time. LFAOs also undergo self-propagative replication by quantitatively converting more monomers into similar toxic oligomers.[24]

Since GRN-3 was able to interact with Aβ monomers and promote aggregates, we questioned whether GRN-3 will be able to interact with specifically with oligomers. To do so, we used LFAOs as model oligomers to investigate. Specifically, we wanted to explore the effect of GRN-3 on the self-propagative replication of LFAOs. Freshly purified LFAOs (1 μM) were incubated with freshly purified seed-free Aβ42 monomers (20 μM) in presence of 40 μM GRN-3 in 20 mM Tris, pH 8.0 at room temperature for 72 h. Control reactions, without the GRN-3, were also incubated under similar conditions. The samples were electrophoresed and immunoblotted after 72 h. No change was

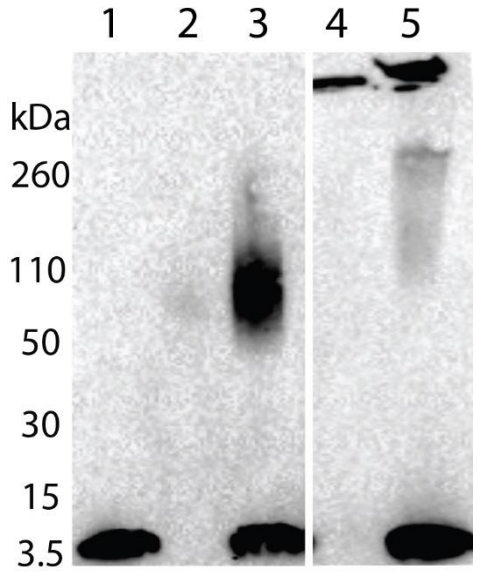

Figure 3.5 Effect of GRN-3 on LFAO replication.

Lane 1, 20 μM Aβ42 monomer alone; *Lane 2*,1 μM LFAO alone; *Lane 3*, 20 μM Aβ42 monomer + 1 μM LFAO; *Lane 4*, 1 μM LFAO + 40 μM GRN-3; and *Lane 5*, 20 μM Aβ42 monomer + 1 μM LFAO + 40 μM GRN-3.

observed in Aβ42 monomer alone and LFAO alone controls after 72 h of incubations (Figure 3.5, lanes 1 and 2, respectively). As expected, there was an increase in the amount of LFAOs incubated with Aβ42 monomers as indicated by the intense band observed in Figure 3.5, lane 3. This increase is due to the unique self-propagative replication of LFAOs as previously reported.[24] However, LFAOs co-incubated with 40 μM GRN-3 alone and with 40 μM GRN-3 and Aβ42 monomers in separate reactions, formed fibrils instead of undergoing their characteristic self-propagation (Figure 3.5, lanes 5 and 6, respectively). This suggests that GRN-3 is able to interact with Aβ irrespective of whether monomeric or oligomeric.

3.3 Discussion and Conclusions

Discerning the causes of AD pathogenesis has been a continuous pursuit to understand the etiology of the disease. In this context, determining the role played by

neuroinflammatory pathways and the myriads of players involved in these pathways in the onset and the progression of AD is vital. One of several such critical players are PGRN and GRNs. Though several clinical evidences support the direct role of PGRN & GRNs in AD pathology, the mechanistic details remain elusive. In this chapter, we provide a proof of concept for involvement of GRN-3 in AD pathology by showing direct interactions between GRN-3 and Aβ, which supports our hypothesis on inflammation-induced neurodegeneration. The data presented here indicate that GRN-3 interacts with Aβ42 monomers at sub-micromolar concentrations. Moreover, the data suggests that the interactions may potentially involve two binding sites with an order of magnitude differences in the binding affinities. Further, we show that GRN-3 rapidly augments Aβ aggregation in a concentration- and time-dependent manner to form high molecular weight fibril-like aggregates. In chapter IIB we established that GRN-3 has a well-defined structure, potentially a β-sheet type structure, whereas mGRN-3 has a collapsed disordered structure due to the disulfide bond scrambling. There is a possibility that GRN-3 may act as a potential template for Aβ aggregation. However, more detailed analyses of this phenomenon are warranted before this claim can be substantiated and will be the future direction of this study. Nevertheless, we have shown that, at super-stoichiometric concentrations, GRN-3 can induce a rapid change in the secondary structure of Aβ monomers from random coil to β-sheet. We have also shown that GRN-3 promotes fibrils formation not only from Aβ monomers but also from specific Aβ oligomers called LFAOs. Taken together, these results provide a proof of concept to support our hypothesis. Further experimentation necessary to determine the precise molecular details underlying GRN-3-Aβ interactions are ongoing in the lab.

CHAPTER IV – OVERALL CONCLUSIONS AND FUTURE DIRECTIONS

4.1 Overall Conclusions

The primary aim of this study was to understand the structure of GRN-3 - one of the seven GRNs proteolytically cleaved from their precursor PGRN with an objective of correlating the information gained to its functions. As mentioned earlier, GRN-3, like other six GRNs, contains twelve conserved cysteines and forms six disulfide bonds. Thus, it was important to discern the role of the disulfide bonds in the structure of GRN-3 which potentially could dictate its functions, especially, its function in AD. The following overall conclusions can be drawn from this study:

- Abrogation of the disulfide bonds renders GRN-3 (rGRN-3) completely disordered which exists as an IDP at low concentrations.
- rGRN-3 shows interesting conformational dynamics; it dimerizes at elevated concentrations and forms a fuzzy complex.
- rGRN-3 exhibits a pro-inflammatory function in CNS, indicated by the activation of NF- κB in neuroblastoma cells.
- Cellular machinery, especially in *E. coli* seems to be rather inefficient in generating native GRN-3 with correct disulfide bonds. In *E. coli*, only 5% of the total expressed GRN-3 is monomeric with all 12 cysteines forming intramolecular disulfide bonds. GRN-3 expressed in human embryonic kidney (HEK) cells too, do not generate intramolecularly disulfide-bonded monomers exclusively although better than *E. coli*. Both *E. coli* and HEK cells form heterogeneous isoforms of multimeric GRN-3 (mGRN-3) consisting of scrambled disulfide bonds to varying degrees.

- GRN-3 shows a well-defined ordered structure as compared to that of mGRN-3 or rGRN-3. mGRN-3 has a largely disordered structure but is more ordered as compared to that of rGRN-3.
- The ordered structure of GRN-3 and the lack of thereof in rGRN-3 or mGRN-3 confirms that disulfide bonds solely dictate the structure of GRN-3 and impart stability to a disordered protein. They mediate an unusual cooperation between structural stability and plasticity which potentially can affect the functions of the protein.
- GRN-3 augments Aβ aggregation by interacting with Aβ monomers and LFAOs providing a proof of concept for the role of GRN-3 in AD pathology.

4.2 Future Directions

Future studies will be directed towards solving the structure of monomeric GRN-3. The HMQC data indicated that GRN-3 has a well-defined structure and elucidating the structure will be very critical. In short, triple resonance spectroscopy will be used where GRN-3 will be doubly labeled with ^{13}C and ^{15}N and the cross-peak correlations will be assigned to obtain the structure.

The role of GRN-3, mGRN-3, and rGRN-3 in AD pathogenesis will be explored in further details. 2D-NMR spectroscopy will be used to confirm the binding interactions between GRN-3 and Aβ42. Briefly, Aβ will be co-incubated with ^{15}N labeled GRN-3 and the changes in the 2D-NMR spectrum of GRN-3 will be monitored. The 2D-NMR spectrum of GRN-3 without Aβ42 will be used as a control. The morphology and structure of high molecular weight aggregates of Aβ promoted by GRN-3 will be investigated using atomic force microscopy.

CHAPTER V – MATERIALS AND EXPERIMENTAL PROCEDURES

5.1 Materials

Wild-type Aβ42 peptide was obtained commercially from the Peptide Synthesis facility at the Mayo Clinic (Rochester, MN). Monoclonal antibody, Ab5 specific for Aβ1-16 was obtained from Mayo Clinic (Jacksonville, FL). The secondary HRP conjugated anti-mouse anti-Fc antibody was obtained from Sigma (St. Loius, MO). All the gel electrophoresis and immunoblotting apparatus and buffers were procured from BioRad Laboratories, (Hercules, CA). The RP-18 LiChroCART HPLC column was obtained from Merck, Germany. The semi-preparative Jupiter® 5 μm C18 reverse phase HPLC column was purchased from Phenomenex, California. All the other chemicals and consumables were procured from VWR, Inc. or Fisher Scientific unless otherwise indicated.

5.2 Experimental Procedures

5.2.1 Cloning of Human GRN-3 in *E. coli*.

Cloning and modifications of the plasmid were carried out at the molecular cloning facility at Florida State University. The GRN-3 cDNA containing a Y24W mutation to facilitate fluorescence detection as well as NcoI and XhoI restriction enzyme sites at N- and C-termini, respectively, was synthesized commercially (Genewiz Inc.). These restriction sites were used to insert GRN-3 cDNA into a pET32b expression vector (Novagen). The commercially available pET32b plasmid facilitates protein expression as a trxA-GRN-3 fusion containing both N- and C-terminal hexa-histidine tags. The enterokinase cleavage site separating thioredoxin from the protein leaves an unwanted His-tag at the C-terminus of the expressed protein. In order to circumvent this obstacle,

the plasmid was modified to remove the C-terminal His-tag by introducing a stop codon downstream from GRN-3 cDNA. In addition, the enterokinase cleavage site along with the spacer DNA were deleted so that the GRN-3 cDNA was present upstream from a preexisting thrombin cleavage site. This modification enabled the expression of GRN-3 protein with a trxA fusion partner and only the N-terminal His-tag. The modified plasmids containing the GRN-3 construct were expressed in the *E. coli* Origami 2(DE3) strain (Novagen) for purification of rGRN-3 and in the *E. coli* SHuffle^{TM} strain (NEB) for purification of GRN-3. The transformed cells expressing the recombinant trxA-GRN-3 fusion protein were grown at 37 °C (Origami) or 30 °C (SHuffle) in 2 L baffled culture shake flasks containing 1 L LB medium supplemented with 100 μg mL^{-1} of ampicillin. Expression of the protein was induced by adding isopropyl β-D-1-thiogalactopyranoside (IPTG) to a final concentration of 0.9 mM for Origami strain and 0.1 mM for SHuflle strain when the optical density of the culture media was between 0.5 and 0.7 AU, as measured by UV-absorbance at 600 nm. Following 4 hours of induction at 37 °C (Origami) or 6 hours of induction at 30 °C (SHuffle), cells were harvested by centrifuging (14000x*g*, 4 °C) and used immediately or stored at -20 °C.

5.2.2 Purification of Recombinant rGRN-3.

Cell pellets from 2 L of culture were thawed at room temperature and resuspended in 30-40 mL of equilibration buffer (50 mM Tris, pH 6.5, 300 mM NaCl, 10 mM imidazole, 2 M urea) containing 0.5 mM phenylmethylsulfonyl fluoride (PMSF). The cell suspension was sonicated for 2 minutes (20-second burst with 1-minute rest) on ice and centrifuged at 9200x*g* to remove debris. The supernatant was loaded onto Ni^{2+}-NTA beads in a flex column pre-equilibrated with five-bed volumes of the equilibration

buffer. The column was then rocked for 1 hour at room temperature, and the supernatant was allowed to flow through the beads under gravity and collected as a flow-through fraction. The beads were then sequentially washed with 100 and 120 mL of buffer (50 mM Tris, pH 6.5, 300 mM NaCl) containing 60 and 80 mM imidazole, respectively. The trxA-rGRN-3 fusion protein was eluted using 20 mL of 300 mM imidazole in 50 mM Tris, pH 6.5, and 300 mM NaCl. The eluate was then reduced with ~10 fold molar excess of the reducing agent, tris(2-carboxyethyl) phosphine (TCEP), by rocking for 1 hour at room temperature and then diluted 10 times with 50 mM Tris, pH 6.5, and 300 mM NaCl. The protein was then dialyzed to remove TCEP and imidazole at room temperature against a buffer of 0.2 mM Tris, pH 6.5, and 0.5 mM NaCl and using a 10 kDa MWCO dialysis membrane (Spectrum Labs). The dialysate was then lyophilized using vacuum evaporation and resuspended in sterile water such that the final buffer concentration was 20 mM Tris, pH 6.5, and 50 mM NaCl. Concentration of the fusion protein was measured using UV-Vis spectroscopy with a molar extinction coefficient of 20355 $M^{-1}cm^{-1}$ at 280 nm.[150] On average, 7-9 mg of fusion protein was obtained per liter of induced cells. The fusion protein was aliquoted in 2 mg mL^{-1} fractions and used immediately or stored at – 20 °C. Further purification of rGRN-3 was accomplished by digesting 2 mg aliquots of the protein via addition of restriction grade thrombin (Novagen) (10 U) to cleave both trxA and the His-tag. The reaction was incubated in a 37 °C water bath for 22-24 hours with 5 U of enzyme added at the start of the incubation and the remaining 5 U added after 8-10 hours of incubation. Completion of the cleavage reaction was confirmed by SDS-PAGE analysis (data not shown). rGRN-3 protein was then fractionated using a LiChroCART C-18 reverse phase HPLC column (Merck Inc, Germany) with a gradient

of 30-90% acetonitrile containing 0.1% TFA. Freshly purified rGRN-3 was used for every experiment, and the protein was used within 2 h of purification to avoid potential re-oxidation issues.

5.2.3 Purification of GRN-3

Cell pellets from 4 L of culture were thawed at room temperature and resuspended in 120 mL of equilibration buffer (50 mM Tris, pH 6.5, 300 mM NaCl, 10 mM imidazole, 2 M urea) containing 0.5 mM phenylmethylsulfonyl fluoride (PMSF). The cell suspension was sonicated for 2 and a half minutes (40-second burst with 1-minute rest) on ice and centrifuged at 9200x*g* to remove debris. The supernatant was incubated with Ni^{2+}-NTA beads pre-equilibrated with five-bed volumes of the equilibration buffer and stirred gradually at 4 °C for 1 hour. The supernatant was then allowed to flow through the beads using a peristaltic pump and collected as a flow-through fraction. The beads were then washed with 200 of buffer (50 mM Tris, pH 6.5, 300 mM NaCl) containing 120 mM imidazole. The trxA-GRN-3 fusion protein was eluted using 50 mL of 400 mM imidazole in 50 mM Tris, pH 6.5, and 300 mM NaCl. The eluate was then dialyzed at 4 °C against a buffer of 2 mM Tris, pH 6.5, and 5 mM NaCl and using a 10 kDa MWCO dialysis membrane (Spectrum Labs). The dialysate was then concentrated 10 times using vacuum evaporation such that the final buffer concentration was 20 mM Tris, pH 6.5, and 50 mM NaCl. Concentration of the fusion protein was measured using UV-Vis spectroscopy with a molar extinction coefficient of 20355 $M^{-1}cm^{-1}$ at 280 nm.[150] On average, 8-10 mg of fusion protein was obtained per liter of induced cells. The fusion protein was then digested by addition of restriction grade thrombin (Novagen) 1U per 1 mg of the protein to cleave both trxA and the His-tag. The

reaction was incubated in a 37 °C water bath for 22-24 hours with half of the units of enzyme added at the start of the incubation and the remaining half were added after 8-10 hours of incubation. Completion of the cleavage reaction was confirmed by SDS-PAGE analysis. GRN-3 protein was then fractionated using a semi-preparative Jupiter® 5 μm C18 reverse phase HPLC column (Phenomenex, CA) with height and internal diameter of 250 mm and 10 mm, respectively with a gradient of 80 – 60 % acetonitrile containing 0.1% TFA. Freshly purified GRN-3 was used for every experiment. The concentration of the protein was estimated spectrophotometrically using the calculated molar extinction coefficient of 6250 $M^{-1}cm^{-1}$ at 280 nm.[150]

5.2.4 Expression and Purification of GRN-3 for ^{15}N Labelling.

For uniform labeling of the backbone and side chain amide nitrogens with ^{15}N the cells were grown in M9 minimal medium with $^{15}NH_4Cl$ (Cambridge Isotope Laboratories, Inc., MA) as the sole nitrogen source. 10x M9 medium was prepared by adding 60g of Na_2HPO_4, 30g KH_2PO_4, 5 g of NaCl, and 5 g of $^{15}NH_4Cl$ to 1 liter of H_2O and sterilized by autoclaving at 121 °C, 15 psi for 20 mins. The 10% (v/v) of 10x M9 medium was supplemented with 1% (v/v) of 100x trace elements solution, 2% (v/v) of 20 % (w/v) Glucose, 0.1% (v/v) of 1M MgSO4, 0.1% (v/v) of 1M CaCl2, 0.1% (v/v) of 1 mg mL^{-1} biotin, 0.1% (v/v) of 1 mg mL^{-1} thiamine and 100 μg mL^{-1} of ampicillin and the final volume was made up to 1000 ml. All the stock solutions, except for 20 % Glucose, were filter sterilized using 0.2 μm filter; glucose was sterilized by autoclaving at 121 °C, 15 psi for 20 mins. The 100x trace elements solution was prepared by adding 5 g of EDTA, 0.83 g of $FeCl_3$ x $6H_2O$, 84 mg of $ZnCl_2$, 13 mg of $CuCl_2$ x 2 H_2O, 10 mg of $CoCl_2$ x 6 H_2O, 10 mg H_3BO_3, and 1.6 mg of $MnCl_2$ x 6 H_2O to 1 liter of sterilized H_2O

and filter sterilized using a 0.2 μm filter. ^{15}N-labeled GRN-3-trxA was expressed and purified using the same protocol as detailed in section *5.2.3*. Further, 15N-labeled GRN-3, mGRN-3, or rGRN-3 were purified using same protocols as detailed in sections *5.2.3* & *5.2.2*. The ^{15}N-labeling was confirmed using MALDI-ToF by assessing the increase in the molecular weight.

5.2.5 Cloning, Expression, and Purification of hGRN-3 from HEK Cells

hGRN-3 was expressed and purified from human embryonic kidney cells by Dr. Kukar's lab at the Emory university. The DNA sequences encoding Granulin-3 (AKA B) was codon optimized and custom synthesized by GenScript (Piscataway, NJ). The amino acid sequence for human GRN 3/B including the linker region at the carboxyl-terminal end was identified based on the Universal Protein Resource database (P28799l; GRN_HUMAN). The endogenous PGRN signal peptide (SP) sequence followed by a twin-Strep and FLAG tag was added to the amino-terminus of GRN-3. Synthetic GRN gene constructs were designed to add a 5' HindIII (AAGCTT) site, a Kozak sequence (GCCACC) before the ATG start codon, a 3' Stop codon, and a XhoI (TGACTCGAG) site. Following synthesis, each gene was inserted into the pcDNA3.1 (+) vector using a HindIII/XhoI cloning strategy. All constructs were verified using DNA sequencing, restriction digests, and PCR amplification. Subsequently, primers were designed to remove the linker region of GRN-3; each construct was amplified via PCR, and subcloned into pcDNA3.1 (+) vector, and verified using DNA sequencing. Amino acid sequence for Granulin-3 without linker 4 (GRN-3) amino acid sequence:
MWTLVSWVALTAGLVAGSAWSHPQFEKGGGSGGGSGGSAWSHPQFEKGASDY

KDDDDKSVMCPDARSRCPDGSTCCELPSGKYGCCPMPNATCCSDHLHCCPQDT VCDLIQSKCLS.

HEK Expi293 cells were transfected with the pcDNA3.1 GRN-3 constructs and conditioned media was collected following the manufacturer's protocol (Thermo-Fisher; Cat# A14635). GRNs were affinity-purified from conditioned media over Strep-Tactin XT Superflow resin using a slightly modified protocol as described by the manufacturer (IBA GmbH; Göttingen, Germany). The elutions containing recombinant GRNs were concentrated and desalted into PBS using Vivaspin 500 Protein Concentrators (molecular weight cut-off 50 kDa; GE Healthcare Life Sciences). The purity of recombinant GRNs was assessed by SDS-PAGE followed by colloidal coomassie dye G-250 protein stain (GelCode Blue; Thermo-Fisher) or silver stain (cat #24600; Thermo-Fisher) and estimated to be >95% pure.

5.2.6 Ellman's Assay

The integrity of disulfide bond in GRN-3 or mGRN-3 or the lack thereof in rGRN-3 was tested using Ellman's assay (Thermo Scientific). Ellman's assay can be used to obtain the free cysteine content in a protein sample. The assay was performed using the manufacturer instructions (Thermo Scientific).

5.2.7 Electrophoresis and Western Blotting

SDS gel electrophoresis was carried out by using 8-16% or 4 – 20% Mini-Protean pre-cast gels (Biorad) and native gel electrophoresis was carried out by using in-house hand casted 14% polyacrylamide gels prepared in 1.5 M Tris, pH 8.8. For SDS gel electrophoresis, the samples were mixed with 4X or 2X reduced or non-reduced Laemmli buffer and were either treated with heat or not. For native gel electrophoresis, samples

were mixed with 2x native gel sample buffer (62.5 mM Tris, pH 8.8, 25% glycerol (v/v), 1% bromophenol blue (w/v)) and electrophoresed using 1x native gel running buffer (2.5mM Tris, pH 8.8 and 19.2 mM glycine). Both SDS and native gels were stained using the Pierce silver staining kits (Thermo Scientific). For immunoblotting, the proteins were transferred on a 0.45 μm BioTrace^{TM} NT nitrocellulose membrane (PALL Life Sciences/BioRad) and blocked with 5% non- fat dry milk in 1x phosphate buffered saline (PBS) with 0.1% tween 20. The blots were probed overnight with an Aβ42 specific antibody, Ab5 (Mayo Clinic, Florida). Blots were then incubated with a HRP-conjugated anti-mouse anti-Fc secondary antibody (Sigma) for 1-2 h and developed with ECL substrate for 2 min (Thermo Scientific). Images were obtained using a GelDoc molecular imager (Biorad).

5.2.8 Mass Spectrometry

The purity of protein preparation was analyzed using MALDI-ToF mass spectrometry (Bruker Daltonics Inc). The sinnapinic acid (SA) matrix was prepared by resuspending 10 mg of SA (Sigma) in one mL of 1:1 acetonitrile: water with 0.1% TFA. One μL of protein samples was mixed with one μL of SA matrix such that the final protein concentration was in 0.01 – 0.1 nM range. Protein-matrix mixture was then spotted in duplicates (1 μL) on a MSP 96 microchip target (Bruker). The laser intensity and the detector gain were kept constant at 70-90% laser and 3x detector gain. For alkylation experiments, 2-4 μg of GRN-3, mGRN-3, or rGRN-3 was incubated with 2000x molar excess of iodoacetamide solution in presence of 1000x molar excess of guanidium hydrochloride at room temperature for 90 mins to overnight in dark. The

alkylation of rGRN-3 or lack of thereof in GRN-3 or mGRN-3 was assessed using MALDI-ToF.

5.2.9 Fluorescence Spectroscopy

Fluorescence measurements were performed on a Cary Eclipse spectrometer (Agilent Inc.). Emission spectral scans between 320-400 nm arising from intrinsic tryptophan fluorescence were measured by exciting the samples at 280 nm. The excitation and emission slits were set at 10 or 20 nm. For ANS binding assay of rGRN-3, the concentration of ANS was kept constant at 500 μM as the rGRN-3 was diluted from 25 μM to 1 μM. Scans were obtained by exciting the samples at 380 nm and reading the emission between from 410 and 600 nm with excitation and emission slits set at 10 nm each. For both tryptophan and ANS experiments, an average of three scans were collected. The data obtained was fit to the following equation for a monomer-dimer model using Origin 8.5 software.

$$F = \frac{2}{M} * \left\{ F_0 - \left(F_0 - F_f \right) * \left(\frac{(4M + K_d) \pm \sqrt{(4M + K_d)^2 - 16M^2}}{8} \right) \right\}$$

in which F is the fraction dimer, M is the monomer concentration, F_0 is initial dimer fraction, F_f is the final dimer fraction, and K_d is the dissociation equilibrium constant. For ANS binding of GRN-3 or mGRN-3, 25 μM of either was incubated with 500 μM ANS as scans were obtained as detailed above. An average of 9 scans were collected to reduce the signal to noise ratio. For Stern-Volmer analysis, 10 & 100 μM of rGRN-3 and 25 μM of GRN-3 or mGRN-3 were titrated with acrylamide ranging from 0.1 to 3 M and the tryptophan fluorescence was monitored as detailed above. Tryptophan fluorescence without the quencher was also obtained by appropriately diluting the protein

using buffer. The F_0/F (without quencher/with quencher) was plotted against the quencher concentration using the Origin 8.5 software to obtain the Stern-Volmer plot.

For TMR-Aβ42-GRN-3 binding experiments, the experimental procedure has been described in section *3.2.1*. For ThT fluorescence, the samples were diluted 15-fold using 10 μM ThT prepared in 20 mM Tris, pH 8.0 or 6.5. Continuous measurements of F were taken for 1 minute with the excitation and emission wavelengths fixed at 450 and 482 nm respectively, and the excitation and emission slits set at 10 nm.

5.2.10 Circular Dichroism (CD)

Far-UV CD spectra were obtained on a Jasco J-815 CD spectrometer. For protein samples with concentration up to 100 μM, a 1 mm path length quartz cuvette (Hellma) was used, whereas, for concentrations above 200 μM, 0.1 mm path length quartz cuvette (Precision cell) was used. Similarly, for effect of TMAO on GRN-3 structure, 0.1 mm path length quartz cuvette (Precision Cell) was used to minimize the scattering. The samples were monitored in a continuous scan mode from 260 to 198 nm with a scanning speed of 50 nm/min with a data integration time of 8 s, 1 nm bandwidth, and the data pitch of 0.1 nm. Each data set was an average of 3 scans and appropriate blanks were subtracted as indicated in the results sections. The corrected scans were smoothened using the Savitzky-Golay algorithm (provided by the manufacturer) with the convolution width of 15 using the Jasco spectrum analysis program. For temperature melt experiments, the samples were first scanned at 25 °C, prior to addition of 1 % SDS, using the continuous scan mode from 260 to 195 nm with a scanning speed of 50 nm min^{-1} with a data integration time of 8 seconds, 1 nm bandwidth, and a data pitch of 0.1 nm. Each data set represents an average of 3 scans with appropriate blank subtraction. After adding

SDS, the samples were scanned immediately over the temperature range of 10 °C to 90 °C with an interval of 10 °C and a ramp rate of 10 °C/min using the temperature interval scan method. Rest of the parameters were same as continuous scanning mode. The scans were subjected to smoothening via the Savitzky-Golay algorithm (provided by the manufacturer) with the convolution width of 9 using the Jasco spectrum analysis program, were blank subtracted, zero corrected, and normalized using Origin 8.5.

5.2.11 Analytical Ultracentrifugation (AUC)

AUC experiments were performed in a Beckman XL-I centrifuge (Beckman Coulter, Inc., Indianapolis, IN) using absorbance optics by measuring intensity scans at 280 nm by Dr. Claudius Mundoma at the Institute of Molecular Biophysics, Florida State University. The experiments were performed at 20 °C in two-channel Epon centerpieces with an AN60 Ti rotor at 55,000 rpm. The protein was solubilized using the buffer 20 mM Tris pH 6.5 protein. Data were analyzed using the UltraScan III version 3.3 software suite.[197]. Data were first analyzed with the two-dimensional spectrum analysis with simultaneous time-invariant noise subtraction according to the method of Schuck and Demeler.[198] After noise subtraction, the data were examined for heterogeneity with the enhanced van Holde−Weischet analysis.[199] The partial specific volume at 20 °C of the GRN-3 protein (0.7021cm^3/g) was estimated from the peptide sequence as described by Durchschlag.[200] All the raw data were processed using SEDFIT program (3) to generate $c(s)$ distributions. A constant diffusion coefficient for all samples was assumed and an f/f_0 value of 1.4.

5.2.12 SOFAST Heteronuclear Multiple Quantum Coherence (HMQC) NMR Spectroscopy

The NMR spectra for GRN-3, mGRN-3, or rGRN-3 was acquired on the Bruker Advance – III-HD 850 MHz NMR spectrometer equipped with a Bruker TCI cryoprobe at the high field NMR facility of University of Alabama, Birmingham. SOFAST HMQC was used as it allows reduction of the recycle delays (T_{scan}) to ≤ 100 ms while maintaining high sensitivity thereby decreasing the overall experimental time.[201] HMQC spectra was obtained for 40 μM (152 μg) of GRN-3 or mGRN-3 and 10 μM (38 μg) of rGRN-3 resuspended in 20 mM Tris, pH 6.5 with 10% D2O inside a Shigemi NMR tube. The spectra were collected with 2048 data points in F2 (^{1}H) with 128 scans coadded for each of the 160 F1 (^{15}N) increments. A $^{1}J_{(NH)}$ of 90 Hz was used with a 100 ms relaxation delay. The delay interval from F1 to F2 was set at 0.32 ms. The spectra was acquired at 25 °C. The HMQC spectra were processed using Bruker TopSpin 3.5 analysis software with standard methods with phase corrections in both dimensions.

5.2.13 Human Neuroblastoma SH-SY5Y Cell Culture and Treatment

The cell culture and treatment was carried out by Lauren Wolf from Dr. Melissa Moss's group at the University of South Carolina. Human neuroblastoma SH-SY5Y cells (Sigma-Aldrich) were maintained in a 1:1 mixture of DMEM and Ham's F12K medium supplemented with FBS (10%), penicillin (100 Units mL^{-1}), and streptomycin (100 μg mL^{-1}). All cultures were maintained at 37 °C in a humid atmosphere of 5% CO_2 and 95% air. SH-SY5Y cells were seeded onto 22 x 22 mm glass coverslips (Corning) at a density of 4×10^5 cells mL^{-1} and allowed to stabilize in culture for 24 hours. Cells were then treated for 60 minutes at 37 °C with rGRN-3 diluted into cell culture medium containing

1% FBS to achieve final concentrations of 0.02-2 μM rGRN-3. Parallel treatment with an equivalent dilution of buffer (20 mM Tris-HCl, pH 6.5, 50 mM NaCl) served as the negative control. Cells were fixed and assessed via immunocytochemistry for normalized cellular NF-κB activation and results are reported as the mean ± SEM for 3-4 independent trials. Statistical analysis was performed with a one-way ANOVA using GraphPad Prism 6 software. When the results of the ANOVA analysis demonstrated significance, a Dunnett's test for multiple comparisons identified groups with means significantly different than the control.

5.2.14 Immunocytochemistry

Following 60 minutes rGRN-3, GRN-3, or mGRN-3 treatment, cells were washed with medium containing 1% FBS and fixed with 4% paraformaldehyde in PBS for 10 minutes at 25 °C. Fixed cells were rinsed 3x with DPBS, permeabilized (0.1% Triton X-100, 0.01 mol L^{-1} glycine in DPBS), and rinsed again with DPBS. To prevent non-specific binding, cells were blocked first with 5% BSA in DPBS, followed by 5% normal donkey serum, 1% BSA in DPBS. Cells were incubated overnight at 4 °C with the primary antibody MAB3026 (Millipore), which is specific for the activated form of the NF-κB p65 subunit, diluted 1:1200 in DPBS. Labeled cells were rinsed with 1% BSA in DPBS prior to blocking with 5% normal donkey serum, 1% BSA in DPBS. Bound primary antibody was detected via incubation for 2 hours at 25 °C with Alexa Fluor 555 conjugate goat anti-mouse secondary antibody diluted 1:1000 in DPBS. After rinsing 3x with 1% BSA in DPBS followed by 2x with DPBS prepared coverslips were mounted onto slides using Fluoroshield with DAPI (Sigma-Aldrich).

Slides were visualized under a Zeiss LSM 510 META Confocal Scanning Laser Microscope (Carl Zeiss) using a plan-neofluar 40X/1.3 oil DIC immersion objective (Carl Zeiss). Z-stacks of the two-channels, corresponding to fluorescently-labeled activated NF-κB and DAPI-labeled nuclei, were acquired to encompass the entire cell layer; z-stacks of three different fields were captured for each treatment.[202, 203] was used to create a z-projection of maximum intensity for each of the two channels within every acquired z-stack. The resultant two-channel images were converted to TIFF files for quantitative image analysis using a custom subroutine written in Matlab™ software (MathWorks). Here, images were separated into the two channels, and each channel was converted into 8-bit monochrome images. DAPI images were transformed into 8-bit binary images via comparison of individual pixel values to a common threshold, and noise was removed. Nuclei were then identified by tagging the pixels representative of nuclear boundaries and identifying successive 'layers' of pixels toward the interior of this boundary until convergence was reached. Upon convergence, a cell was counted, and a radius of exclusivity was defined within which another cell could not be identified. Next, 8-bit monochrome NF-κB images were used to calculate the fluorescence associated with activated NF-κB, which was divided by the number of cells to yield the activated NF-κB fluorescence per cell. This cellular NF-κB activation was determined using the three images acquired for each treatment. Reported values are normalized to the cellular NF-κB activation observed for the control.

5.2.15 I-TASSER Analysis

The structure prediction of GRN-3 was carried out using the free structure predicting tool called I-TASSER (Iterative Threading ASSEmbly Refinement) available

at http://zhanglab.ccmb.med.umich.edu/I-TASSER/. The primary amino acid sequence of GRN-3 was submitted in the FASTA format. Briefly, I-TASSER identifies similar structural templates from PDB (protein data bank) using multiple threading approach LOMETS (local meta-threading server). The server then uses the iterative template fragment assembly simulations to generate the full-length atomic models. Each predicted model is assigned a c-score or the confidence score which determines the validity of the prediction; higher the c-score, higher the validity of prediction.

REFERENCES

1. Selkoe, D. J. (2001) Alzheimer's disease: genes, proteins, and therapy, *Physiol Rev 81*, 741-766.
2. Haass, C., and Selkoe, D. J. (2007) Soluble protein oligomers in neurodegeneration: lessons from the Alzheimer's amyloid beta-peptide, *Nat Rev Mol Cell Biol 8*, 101-112.
3. Miller, D. L., Papayannopoulos, I. A., Styles, J., Bobin, S. A., Lin, Y. Y., Biemann, K., and Iqbal, K. (1993) Peptide compositions of the cerebrovascular and senile plaque core amyloid deposits of Alzheimer's disease, *Arch Biochem Biophys 301*, 41-52.
4. Selkoe, D. J. (1990) Deciphering Alzheimer's disease: the amyloid precursor protein yields new clues, *Science 248*, 1058-1060.
5. Small, D. H., and McLean, C. A. (1999) Alzheimer's Disease and the Amyloid β Protein, *Journal of neurochemistry 73*, 443-449.
6. Vassar, R., Bennett, B. D., Babu-Khan, S., Kahn, S., Mendiaz, E. A., Denis, P., Teplow, D. B., Ross, S., Amarante, P., Loeloff, R., Luo, Y., Fisher, S., Fuller, J., Edenson, S., Lile, J., Jarosinski, M. A., Biere, A. L., Curran, E., Burgess, T., Louis, J.-C., Collins, F., Treanor, J., Rogers, G., and Citron, M. (1999) β-Secretase Cleavage of Alzheimer's Amyloid Precursor Protein by the Transmembrane Aspartic Protease BACE, *Science 286*, 735-741.
7. Kimberly, W. T., LaVoie, M. J., Ostaszewski, B. L., Ye, W., Wolfe, M. S., and Selkoe, D. J. (2003) Gamma-secretase is a membrane protein complex comprised of presenilin, nicastrin, Aph-1, and Pen-2, *Proc Natl Acad Sci U S A 100*, 6382-6387.
8. Kirkitadze, M. D., Condron, M. M., and Teplow, D. B. (2001) Identification and characterization of key kinetic intermediates in amyloid β-protein fibrillogenesis, *Journal of molecular biology 312*, 1103-1119.
9. Tompa, P. (2002) Intrinsically unstructured proteins, *Trends in Biochemical Sciences 27*, 527-533.
10. Harper, J. D., and Lansbury, P. T. (1997) MODELS OF AMYLOID SEEDING IN ALZHEIMER'S DISEASE AND SCRAPIE:Mechanistic Truths and Physiological Consequences of the Time-Dependent Solubility of Amyloid Proteins, *Annual Review of Biochemistry 66*, 385-407.
11. Lomakin, A., Teplow, D. B., Kirschner, D. A., and Benedek, G. B. (1997) Kinetic theory of fibrillogenesis of amyloid β-protein, *Proceedings of the National Academy of Sciences 94*, 7942-7947.
12. Ghosh, P., Kumar, A., Datta, B., and Rangachari, V. (2010) Dynamics of protofibril elongation and association involved in Abeta42 peptide aggregation in Alzheimer's disease, *BMC Bioinformatics 11*, S24.
13. Hardy, J. A., and Higgins, G. A. (1992) Alzheimer's disease: the amyloid cascade hypothesis, *Science 256*, 184-185.
14. Hsiao, K., Chapman, P., Nilsen, S., Eckman, C., Harigaya, Y., Younkin, S., Yang, F., and Cole, G. (1996) Correlative Memory Deficits, Aβ Elevation, and Amyloid Plaques in Transgenic Mice, *Science 274*, 99-103.

15. McLean, C. A., Cherny, R. A., Fraser, F. W., Fuller, S. J., Smith, M. J., Beyreuther, K., Bush, A. I., and Masters, C. L. (1999) Soluble pool of Abeta amyloid as a determinant of severity of neurodegeneration in Alzheimer's disease, *Ann Neurol 46*, 860-866.
16. Townsend, M., Shankar, G. M., Mehta, T., Walsh, D. M., and Selkoe, D. J. (2006) Effects of secreted oligomers of amyloid beta-protein on hippocampal synaptic plasticity: a potent role for trimers, *J Physiol 572*, 477-492.
17. Walsh, D. M., Klyubin, I., Fadeeva, J. V., Rowan, M. J., and Selkoe, D. J. (2002) Amyloid-beta oligomers: their production, toxicity and therapeutic inhibition, *Biochem Soc Trans 30*, 552-557.
18. McLean, C. A., Cherny, R. A., Fraser, F. W., Fuller, S. J., Smith, M. J., Konrad, V., Bush, A. I., and Masters, C. L. (1999) Soluble pool of Aβ amyloid as a determinant of severity of neurodegeneration in Alzheimer's disease, *Annals of Neurology 46*, 860-866.
19. Lesné, S., Koh, M. T., Kotilinek, L., Kayed, R., Glabe, C. G., Yang, A., Gallagher, M., and Ashe, K. H. (2006) A specific amyloid-β protein assembly in the brain impairs memory, *Nature 440*, 352-357.
20. Lesne, S., Koh, M. T., Kotilinek, L., Kayed, R., Glabe, C. G., Yang, A., Gallagher, M., and Ashe, K. H. (2006) A specific amyloid-beta protein assembly in the brain impairs memory, *Nature 440*, 352-357.
21. Shankar, G. M., Li, S., Mehta, T. H., Garcia-Munoz, A., Shepardson, N. E., Smith, I., Brett, F. M., Farrell, M. A., Rowan, M. J., Lemere, C. A., Regan, C. M., Walsh, D. M., Sabatini, B. L., and Selkoe, D. J. (2008) Amyloid-beta protein dimers isolated directly from Alzheimer's brains impair synaptic plasticity and memory, *Nat Med 14*, 837-842.
22. Podlisny, M. B., Ostaszewski, B. L., Squazzo, S. L., Koo, E. H., Rydell, R. E., Teplow, D. B., and Selkoe, D. J. (1995) Aggregation of secreted amyloid beta-protein into sodium dodecyl sulfate-stable oligomers in cell culture, *J Biol Chem 270*, 9564-9570.
23. Kumar, A., Bullard, R. L., Patel, P., Paslay, L. C., Singh, D., Bienkiewicz, E. A., Morgan, S. E., and Rangachari, V. Non-esterified fatty acids generate distinct low-molecular weight amyloid-beta (Abeta42) oligomers along pathway different from fibril formation, *PLoS One 6*, e18759.
24. Kumar, A., Paslay, L. C., Lyons, D., Morgan, S. E., Correia, J. J., and Rangachari, V. Specific soluble oligomers of amyloid-beta peptide undergo replication and form non-fibrillar aggregates in interfacial environments, *J Biol Chem 287*, 21253-21264.
25. Dean, D. N., Pate, K. M., Moss, M. A., and Rangachari, V. (2016) Conformational Dynamics of Specific Aβ Oligomers Govern Their Ability to Replicate and Induce Neuronal Apoptosis, *Biochemistry 55*, 2238-2250.
26. Dean, D. N., Das, P. K., Rana, P., Burg, F., Levites, Y., Morgan, S. E., Ghosh, P., and Rangachari, V. (2017) Strain-specific Fibril Propagation by an Aβ Dodecamer, *Scientific Reports 7*, 40787.
27. Selkoe, D. J., and Podlisny, M. B. (2002) Deciphering the genetic basis of Alzheimer's disease, *Annu Rev Genomics Hum Genet 3*, 67-99.

28. Akiyama, H., Barger, S., Barnum, S., Bradt, B., Bauer, J., Cole, G., Cooper, N., Eikelenboom, P., Emmerling, M., Fiebich, B., Finch, C., Frautschy, S., Griffin, W., Hampel, H., Hull, M., Landreth, G., Lue, L., Mrak, R., Mackenzie, I., McGeer, P., O'Banion, M., Pachter, J., Pasinetti, G., Plata-Salaman, C., Rogers, J., Rydel, R., Shen, Y., Streit, W., Strohmeyer, R., and Tooyoma, I. (2000) Inflammation and Alzheimer's disease, *Neurobiol Aging 21*, 383 - 421.
29. Wyss-Coray, T., and Mucke, L. (2002) Inflammation in neurodegenerative disease—a double-edged sword, *Neuron 35*, 419-432.
30. Kalaria, R. N. (1999) Microglia and Alzheimer's disease, *Current Opinion in Hematology 6*, 15.
31. Eikelenboom, P., Veerhuis, R., Scheper, W., Rozemuller, A. J. M., van Gool, W. A., and Hoozemans, J. J. M. (2006) The significance of neuroinflammation in understanding Alzheimer's disease, *J Neural Transm 113*, 1685-1695.
32. Kreutzberg, G. W. (1996) Microglia: a sensor for pathological events in the CNS, *Trends in Neurosciences 19*, 312-318.
33. Lee, C. D., and Landreth, G. E. (2010) The role of microglia in amyloid clearance from the AD brain, *J Neural Transm 117*, 949-960.
34. Hickman, S. E., Allison, E. K., and El Khoury, J. (2008) Microglial dysfunction and defective β-amyloid clearance pathways in aging Alzheimer's disease mice, *The Journal of neuroscience 28*, 8354-8360.
35. Rogers, J., Strohmeyer, R., Kovelowski, C., and Li, R. (2002) Microglia and inflammatory mechanisms in the clearance of amyloid β peptide, *Glia 40*, 260-269.
36. Morgan, D., Gordon, M., Tan, J., Wilcock, D., and Rojiani, A. (2005) Dynamic complexity of the microglial activation response in transgenic models of amyloid deposition: implications for Alzheimer therapeutics, *J Neuropathol Exp Neurol 64*, 743 - 753.
37. Engelhart, M., Geerlings, M., Meijer, J., Kiliaan, A., Ruitenberg, A., van Swieten, J., Stijnen, T., Hofman, A., Witteman, J., and Breteler, M. (2004) Inflammatory proteins in plasma and the risk of dementia: the rotterdam study, *Arch Neurol 61*, 668 - 672.
38. Stewart, W. F., Kawas, C., Corrada, M., and Metter, E. J. (1997) Risk of Alzheimer's disease and duration of NSAID use, *Neurology 48*, 626-632.
39. In 't Veld, B. A., Launer, L. J., Hoes, A. W., Ott, A., Hofman, A., Breteler, M. M. B., and Stricker, B. H. C. (1998) NSAIDs and incident Alzheimer's disease. the Rotterdam study, *Neurobiology of Aging 19*, 607-611.
40. Herrup, K. (2010) Reimagining Alzheimer's Disease—An Age-Based Hypothesis, *The Journal of Neuroscience 30*, 16755-16762.
41. Lye, T. C., and Shores, E. A. (2000) Traumatic brain injury as a risk factor for Alzheimer's disease: a review, *Neuropsychology review 10*, 115-129.
42. Nemetz, P. N., Leibson, C., Naessens, J. M., Beard, M., Kokmen, E., Annegers, J. F., and Kurland, L. T. (1999) Traumatic brain injury and time to onset of Alzheimer's disease: a population-based study, *American Journal of Epidemiology 149*, 32-40.

43. Johnson, V. E., Stewart, W., and Smith, D. H. (2010) Traumatic brain injury and amyloid-β pathology: a link to Alzheimer's disease?, *Nature Reviews Neuroscience 11*, 361-370.
44. El Khoury, J., Toft, M., Hickman, S. E., Means, T. K., Terada, K., Geula, C., and Luster, A. D. (2007) Ccr2 deficiency impairs microglial accumulation and accelerates progression of Alzheimer-like disease, *Nature medicine 13*, 432-438.
45. Del Bo, R., Angeretti, N., Lucca, E., De Simoni, M. G., and Forloni, G. (1995) Reciprocal control of inflammatory cytokines, IL-1 and IL-6, and β-amyloid production in cultures, *Neuroscience Letters 188*, 70-74.
46. Ringheim, G. E., Szczepanik, A. M., Petko, W., Burgher, K. L., Zhu, S. Z., and Chao, C. C. (1998) Enhancement of beta-amyloid precursor protein transcription and expression by the soluble interleukin-6 receptor/interleukin-6 complex, *Molecular Brain Research 55*, 35-44.
47. Baba, T., Hoff, H. B., Nemoto, H., Lee, H., Orth, J., Arai, Y., and Gerton, G. L. (1993) Acrogranin, an acrosomal cysteine-rich glycoprotein, is the precursor of the growth-modulating peptides, granulins, and epithelins, and is expressed in somatic as well as male germ cells, *Molecular reproduction and development 34*, 233-243.
48. Bateman, A., and Bennett, H. P. (1998) Granulins: the structure and function of an emerging family of growth factors, *J Endocrinol 158*, 145-151.
49. Plowman, G. D., Green, J. M., Neubauer, M. G., Buckley, S. D., McDonald, V. L., Todaro, G. J., and Shoyab, M. (1992) The epithelin precursor encodes two proteins with opposing activities on epithelial cell growth, *Journal of Biological Chemistry 267*, 13073-13078.
50. Zanocco-Marani, T., Bateman, A., Romano, G., Valentinis, B., He, Z.-H., and Baserga, R. (1999) Biological activities and signaling pathways of the granulin/epithelin precursor, *Cancer Research 59*, 5331-5340.
51. Zhou, J., Gao, G., Crabb, J. W., and Serrero, G. (1993) Purification of an autocrine growth factor homologous with mouse epithelin precursor from a highly tumorigenic cell line, *Journal of Biological Chemistry 268*, 10863-10869.
52. Bhandari, V., Palfree, R., and Bateman, A. (1992) Isolation and sequence of the granulin precursor cDNA from human bone marrow reveals tandem cysteine-rich granulin domains, *Proceedings of the National Academy of Sciences 89*, 1715-1719.
53. Bucan, M., Gatalica, B., Baba, T., and Gerton, G. (1996) Mapping of Grn, the gene encoding the granulin/epithelin precursor (acrogranin), to mouse chromosome 11, *Mammalian Genome 7*, 704-705.
54. Avrova, A. O., Stewart, H. E., De Jong, W., Heilbronn, J., Lyon, G. D., and Birch, P. R. (1999) A cysteine protease gene is expressed early in resistant potato interactions with Phytophthora infestans, *Molecular plant-microbe interactions 12*, 1114-1119.
55. Belcourt, D. R., Lazure, C., and Bennett, H. (1993) Isolation and primary structure of the three major forms of granulin-like peptides from hematopoietic tissues of a teleost fish (Cyprinus carpio), *Journal of Biological Chemistry 268*, 9230-9237.

56. Couto, M., Harwig, S., Cullor, J. S., Hughes, J., and Lehrer, R. (1992) Identification of eNAP-1, an antimicrobial peptide from equine neutrophils, *Infection and immunity 60*, 3065-3071.
57. Hong, S. J., and Kang, K. W. (1999) Purification of granulin-like polypeptide from the blood-sucking leech, Hirudo nipponia, *Protein expression and purification 16*, 340-346.
58. Daniel, R., Daniels, E., He, Z., and Bateman, A. (2003) Progranulin (acrogranin/PC cell-derived growth factor/granulin-epithelin precursor) is expressed in the placenta, epidermis, microvasculature, and brain during murine development, *Developmental Dynamics 227*, 593-599.
59. Daniel, R., He, Z., Carmichael, K. P., Halper, J., and Bateman, A. (2000) Cellular Localization of Gene Expression for Progranulin, *Journal of Histochemistry & Cytochemistry 48*, 999-1009.
60. Moisse, K., Volkening, K., Leystra-Lantz, C., Welch, I., Hill, T., and Strong, M. J. (2009) Divergent patterns of cytosolic TDP-43 and neuronal progranulin expression following axotomy: implications for TDP-43 in the physiological response to neuronal injury, *Brain research 1249*, 202-211.
61. Petkau, T. L., Neal, S., Orban, P., MacDonald, J., Hill, A., Lu, G., Feldman, H., Mackenzie, I., and Leavitt, B. (2010) Progranulin expression in the developing and adult murine brain, *Journal of Comparative Neurology 518*, 3931-3947.
62. Ryan, C. L., Baranowski, D. C., Chitramuthu, B. P., Malik, S., Li, Z., Cao, M., Minotti, S., Durham, H. D., Kay, D. G., and Shaw, C. A. (2009) Progranulin is expressed within motor neurons and promotes neuronal cell survival, *BMC neuroscience 10*, 1.
63. Pereson, S., Wils, H., Kleinberger, G., McGowan, E., Vandewoestyne, M., Van Broeck, B., Joris, G., Cuijt, I., Deforce, D., and Hutton, M. (2009) Progranulin expression correlates with dense-core amyloid plaque burden in Alzheimer disease mouse models, *The Journal of pathology 219*, 173-181.
64. Byrnes, K. R., Washington, P. M., Knoblach, S. M., Hoffman, E., and Faden, A. I. (2011) Delayed inflammatory mRNA and protein expression after spinal cord injury, *Journal of neuroinflammation 8*, 1.
65. Naphade, S. B., Kigerl, K. A., Jakeman, L. B., Kostyk, S. K., Popovich, P. G., and Kuret, J. (2010) Progranulin expression is upregulated after spinal contusion in mice, *Acta neuropathologica 119*, 123-133.
66. Tanaka, Y., Matsuwaki, T., Yamanouchi, K., and Nishihara, M. (2013) Exacerbated inflammatory responses related to activated microglia after traumatic brain injury in progranulin-deficient mice, *Neuroscience 231*, 49-60.
67. Vercellino, M., Grifoni, S., Romagnolo, A., Masera, S., Mattioda, A., Trebini, C., Chiavazza, C., Caligiana, L., Capello, E., and Mancardi, G. L. (2011) Progranulin expression in brain tissue and cerebrospinal fluid levels in multiple sclerosis, *Multiple Sclerosis Journal 17*, 1194-1201.
68. Songsrirote, K., Li, Z., Ashford, D., Bateman, A., and Thomas-Oates, J. (2010) Development and application of mass spectrometric methods for the analysis of progranulin N-glycosylation, *Journal of proteomics 73*, 1479-1490.

69. Bateman, A., Belcourt, D., Bennett, H., Lazure, C., and Solomon, S. (1990) Granulins, a novel class of peptide from leukocytes, *Biochemical and Biophysical Research Communications 173*, 1161-1168.
70. Shoyab, M., McDonald, V. L., Byles, C., Todaro, G. J., and Plowman, G. D. (1990) Epithelins 1 and 2: isolation and characterization of two cysteine-rich growth-modulating proteins, *Proceedings of the National Academy of Sciences 87*, 7912-7916.
71. Hrabal, R., Chen, Z., James, S., Bennett, H., and Ni, F. (1996) The hairpin stack fold, a novel protein architecture for a new family of protein growth factors, *Nature structural biology 3*, 747-752.
72. Zhu, J., Nathan, C., Jin, W., Sim, D., Ashcroft, G. S., Wahl, S. M., Lacomis, L., Erdjument-Bromage, H., Tempst, P., Wright, C. D., and Ding, A. (2002) Conversion of proepithelin to epithelins: roles of SLPI and elastase in host defense and wound repair, *Cell 111*, 867-878.
73. Kessenbrock, K., Fr, xF, hlich, L., Sixt, M., xE, mmermann, T., Pfister, H., Bateman, A., Belaaouaj, A., Ring, J., Ollert, M., ssler, R., and Jenne, D. E. (2008) Proteinase 3 and neutrophil elastase enhance inflammation in mice by inactivating antiinflammatory progranulin, *The Journal of Clinical Investigation 118*, 2438-2447.
74. Vercellino, M., Grifoni, S., Romagnolo, A., Masera, S., Mattioda, A., Trebini, C., Chiavazza, C., Caligiana, L., Capello, E., Mancardi, G. L., Giobbe, D., Mutani, R., Giordana, M. T., and Cavalla, P. (2011) Progranulin expression in brain tissue and cerebrospinal fluid levels in multiple sclerosis, *Multiple Sclerosis Journal 17*, 1194-1201.
75. Butler, G. S., Dean, R. A., Tam, E. M., and Overall, C. M. (2008) Pharmacoproteomics of a Metalloproteinase Hydroxamate Inhibitor in Breast Cancer Cells: Dynamics of Membrane Type 1 Matrix Metalloproteinase-Mediated Membrane Protein Shedding, *Molecular and Cellular Biology 28*, 4896-4914.
76. Bai, X.-H., Wang, D.-W., Kong, L., Zhang, Y., Luan, Y., Kobayashi, T., Kronenberg, H. M., Yu, X.-P., and Liu, C.-j. (2009) ADAMTS-7, a Direct Target of PTHrP, Adversely Regulates Endochondral Bone Growth by Associating with and Inactivating GEP Growth Factor, *Molecular and Cellular Biology 29*, 4201-4219.
77. Cenik, B., Sephton, C. F., Cenik, B. K., Herz, J., and Yu, G. (2012) Progranulin: a proteolytically processed protein at the crossroads of inflammation and neurodegeneration, *Journal of Biological Chemistry*.
78. Sparro, G., Galdenzi, G., Eleuteri, A. M., Angeletti, M., Schroeder, W., and Fioretti, E. (1997) Isolation and N-terminal sequence of multiple forms of granulins in human urine, *Protein expression and purification 10*, 169-174.
79. Bateman, A., and Bennett, H. (1998) Granulins: the structure and function of an emerging family of growth factors, *Journal of Endocrinology 158*, 145-151.
80. Toh, H., Chitramuthu, B. P., Bennett, H. P., and Bateman, A. (2011) Structure, function, and mechanism of progranulin; the brain and beyond, *Journal of Molecular Neuroscience 45*, 538-548.

81. Baker, M., Mackenzie, I. R., Pickering-Brown, S. M., and al., e. (2006) Mutations in progranulin cause tau-negative frontotemporal dementia linked to chromosome 17, *Nature 442*, 916-919.
82. Díaz-Cueto, L., Stein, P., Jacobs, A., Schultz, R. M., and Gerton, G. L. (2000) Modulation of mouse preimplantation embryo development by acrogranin (epithelin/granulin precursor), *Developmental biology 217*, 406-418.
83. SUZUKI, M., MATSUMURO, M., Hirabayashi, K., Ogawara, M., Takahashi, M., and Nishihara, M. (2000) Oocyte-Specific Expression of Granulin Precursor (Acrogranin) in Rat Ovary, *Journal of Reproduction and Development 46*, 271-277.
84. Anakwe, O., and Gerton, G. (1990) Acrosome biogenesis begins during meiosis: evidence from the synthesis and distribution of an acrosomal glycoprotein, acrogranin, during guinea pig spermatogenesis, *Biology of reproduction 42*, 317-328.
85. Suzuki, M., and Nishiahara, M. (2002) Granulin precursor gene: a sex steroid-inducible gene involved in sexual differentiation of the rat brain, *Molecular genetics and metabolism 75*, 31-37.
86. De Muynck, L., Herdewyn, S., Beel, S., Scheveneels, W., Van Den Bosch, L., Robberecht, W., and Van Damme, P. (2013) The neurotrophic properties of progranulin depend on the granulin E domain but do not require sortilin binding, *Neurobiology of aging 34*, 2541-2547.
87. Gass, J., Lee, W. C., Cook, C., Finch, N., Stetler, C., Jansen-West, K., Lewis, J., Link, C. D., Rademakers, R., and Nykjær, A. (2012) Progranulin regulates neuronal outgrowth independent of sortilin, *Molecular neurodegeneration 7*, 1.
88. Pickford, F., Marcus, J., Camargo, L. M., Xiao, Q., Graham, D., Mo, J.-R., Burkhardt, M., Kulkarni, V., Crispino, J., Hering, H., and Hutton, M. (2011) Progranulin Is a Chemoattractant for Microglia and Stimulates Their Endocytic Activity, *The American Journal of Pathology 178*, 284-295.
89. Minami, S. S., Min, S.-W., Krabbe, G., Wang, C., Zhou, Y., Asgarov, R., Li, Y., Martens, L. H., Elia, L. P., Ward, M. E., Mucke, L., Farese Jr, R. V., and Gan, L. (2014) Progranulin protects against amyloid [beta] deposition and toxicity in Alzheimer's disease mouse models, *Nat Med 20*, 1157-1164.
90. He, Z., and Bateman, A. (2003) Progranulin (granulin-epithelin precursor, PC-cell-derived growth factor, acrogranin) mediates tissue repair and tumorigenesis, *Journal of Molecular Medicine 81*, 600-612.
91. Tang, W., Lu, Y., Tian, Q.-Y., Zhang, Y., Guo, F.-J., Liu, G.-Y., Syed, N. M., Lai, Y., Lin, E. A., and Kong, L. (2011) The growth factor progranulin binds to TNF receptors and is therapeutic against inflammatory arthritis in mice, *Science 332*, 478-484.
92. Kohda, D., and Inagaki, F. (1991) 3D Structures of EGF and TGF-alpha determined by NMR, *Analytical Sciences 7*, 853-856.
93. Moy, F. J., Li, Y. C., Rauenbuehler, P., Winkler, M. E., Scheraga, H. A., and Montelione, G. T. (1993) Solution structure of human type-. alpha. transforming growth factor determined by heteronuclear NMR spectroscopy and refined by energy minimization with restraints, *Biochemistry 32*, 7334-7353.

94. Prestrelski, S., Arakawa, T., Wu, C., O'Neal, K., Westcott, K., and Narhi, L. (1992) Solution structure and dynamics of epidermal growth factor and transforming growth factor alpha, *Journal of Biological Chemistry 267*, 319-322.
95. Matsumoto, K., Takehara, T., Inoue, H., Hagiya, M., Shimizu, S., and Nakamura, T. (1991) Deletion of kringle domains or the N-terminal hairpin structure in hepatocyte growth factor results in marked decreases in related biological activities, *Biochemical and Biophysical Research Communications 181*, 691-699.
96. Nakamura, T., Nishizawa, T., Hagiya, M., Seki, T., Shimonishi, M., Sugimura, A., Tashiro, K., and Shimizu, S. (1989) Molecular cloning and expression of human hepatocyte growth factor.
97. Magnusson, S., Petersen, T. E., Sottrup-Jensen, L., and Claeys, H. (1975) Complete primary structure of prothrombin: Isolation, structure and reactivity of ten carboxylated glutamic acid residues and regulation of prothrombin activation by thrombin, *Proteases and biological control 2*, 123-149.
98. McLean, J. W., Tomlinson, J. E., Kuang, W.-J., Eaton, D. L., Chen, E. Y., Fless, G. M., Scanu, A. M., and Lawn, R. M. (1987) cDNA sequence of human apolipoprotein (a) is homologous to plasminogen, *Nature 330*, 132-137.
99. De Vos, A. M., Ultsch, M. H., Kelley, R. F., Padmanabhan, K., Tulinsky, A., Westbrook, M. L., and Kossiakoff, A. A. (1992) Crystal structure of the kringle 2 domain of tissue plasminogen activator at 2.4-. ANG. resolution, *Biochemistry 31*, 270-279.
100. Tolkatchev, D., Malik, S., Vinogradova, A., Wang, P., Chen, Z., Xu, P., Bennett, H. P., Bateman, A., and Ni, F. (2008) Structure dissection of human progranulin identifies well-folded granulin/epithelin modules with unique functional activities, *Protein Sci 17*, 711-724.
101. Vranken, W. F., Chen, Z. G., Xu, P., James, S., Bennett, H. P. J., and Ni, F. (1999) A 30-residue fragment of the carp granulin-1 protein folds into a stack of two β-hairpins similar to that found in the native protein, *The Journal of Peptide Research 53*, 590-597.
102. Tolkatchev, D., Ng, A., Vranken, W., and Ni, F. (2000) Design and solution structure of a well-folded stack of two beta-hairpins based on the amino-terminal fragment of human granulin A, *Biochemistry 39*, 2878-2886.
103. Liau, L. M., Lallone, R. L., Seitz, R. S., Buznikov, A., Gregg, J. P., Kornblum, H. I., Nelson, S. F., and Bronstein, J. M. (2000) Identification of a Human Glioma-associated Growth Factor Gene, granulin, Using Differential Immuno-absorption, *Cancer Research 60*, 1353-1360.
104. Azizi, G., Navabi, S. S., Al-Shukaili, A., Seyedzadeh, M. H., Yazdani, R., and Mirshafiey, A. (2015) The Role of Inflammatory Mediators in the Pathogenesis of Alzheimer's Disease, *Sultan Qaboos University Medical Journal 15*, e305-e316.
105. Brouwers, N., Nuytemans, K., van der Zee, J., and et al. (2007) ALzheimer and parkinson diagnoses in progranulin null mutation carriers in an extended founder family, *Archives of Neurology 64*, 1436-1446.
106. Cortini, F., Fenoglio, C., Guidi, I., Venturelli, E., Pomati, S., Marcone, A., Scalabrini, D., Villa, C., Clerici, F., Dalla Valle, E., Mariani, C., Cappa, S., Bresolin, N., Scarpini, E., and Galimberti, D. (2008) Novel exon 1 progranulin

gene variant in Alzheimer's disease, *European Journal of Neurology 15*, 1111-1117.
107. Pereson, S., Wils, H., Kleinberger, G., McGowan, E., Vandewoestyne, M., Van Broeck, B., Joris, G., Cuijt, I., Deforce, D., Hutton, M., Van Broeckhoven, C., and Kumar-Singh, S. (2009) Progranulin expression correlates with dense-core amyloid plaque burden in Alzheimer disease mouse models, *The Journal of Pathology 219*, 173-181.
108. Eriksen, J. L., and Mackenzie, I. R. (2007) Progranulin: normal function and role in neurodegeneration, *J Neurochem*.
109. Neary, D., Snowden, J. S., Gustafson, L., Passant, U., Stuss, D., Black, S. a., Freedman, M., Kertesz, A., Robert, P., and Albert, M. (1998) Frontotemporal lobar degeneration A consensus on clinical diagnostic criteria, *Neurology 51*, 1546-1554.
110. McKhann, G. M., Albert, M. S., Grossman, M., Miller, B., Dickson, D., and Trojanowski, J. Q. (2001) Clinical and pathological diagnosis of frontotemporal dementia: report of the Work Group on Frontotemporal Dementia and Pick's Disease, *Archives of neurology 58*, 1803-1809.
111. Lomen-Hoerth, C., Anderson, T., and Miller, B. (2002) The overlap of amyotrophic lateral sclerosis and frontotemporal dementia, *Neurology 59*, 1077-1079.
112. Trojanowski, J. Q., and Dickson, D. (2001) Update on the neuropathological diagnosis of frontotemporal dementias, *Journal of Neuropathology & Experimental Neurology 60*, 1123-1126.
113. Lipton, A. M., White III, C. L., and Bigio, E. H. (2004) Frontotemporal lobar degeneration with motor neuron disease-type inclusions predominates in 76 cases of frontotemporal degeneration, *Acta neuropathologica 108*, 379-385.
114. Mackenzie, I. R., Shi, J., Shaw, C. L., DuPlessis, D., Neary, D., Snowden, J. S., and Mann, D. M. (2006) Dementia lacking distinctive histology (DLDH) revisited, *Acta neuropathologica 112*, 551-559.
115. Stevens, M., Van Duijn, C., Kamphorst, W., De Knijff, P., Heutink, P., Van Gool, W., Scheltens, P., Ravid, R., Oostra, B., and Niermeijer, M. (1998) Familial aggregation in frontotemporal dementia, *Neurology 50*, 1541-1545.
116. Chow, T. W., Miller, B. L., Hayashi, V. N., and Geschwind, D. H. (1999) Inheritance of frontotemporal dementia, *Archives of Neurology 56*, 817-822.
117. Rosso, S. M., Kaat, L. D., Baks, T., Joosse, M., de Koning, I., Pijnenburg, Y., de Jong, D., Dooijes, D., Kamphorst, W., and Ravid, R. (2003) Frontotemporal dementia in The Netherlands: patient characteristics and prevalence estimates from a population-based study, *Brain 126*, 2016-2022.
118. Le Ber, I., Van Der Zee, J., Hannequin, D., Gijselinck, I., Campion, D., Puel, M., Laquerrière, A., De Pooter, T., Camuzat, A., and Van den Broeck, M. (2007) Progranulin null mutations in both sporadic and familial frontotemporal dementia, *Human mutation 28*, 846-855.
119. Molgaard, C. A., Stanford, E. P., Morton, D. J., Ryden, L. A., Schubert, K. R., and Golbeck, A. L. (1990) Epidemiology of head trauma and neurocognitive impairment in a multi-ethnic population, *Neuroepidemiology 9*, 233-242.

120. Cruts, M., Gijselinck, I., van der Zee, J., Engelborghs, S., Wils, H., Pirici, D., Rademakers, R., Vandenberghe, R., Dermaut, B., Martin, J. J., van Duijn, C., Peeters, K., Sciot, R., Santens, P., De Pooter, T., Mattheijssens, M., Van den Broeck, M., Cuijt, I., Vennekens, K., De Deyn, P. P., Kumar-Singh, S., and Van Broeckhoven, C. (2006) Null mutations in progranulin cause ubiquitin-positive frontotemporal dementia linked to chromosome 17q21, *Nature 442*, 920-924.
121. Baker, C. A., and Manuelidis, L. (2003) Unique inflammatory RNA profiles of microglia in Creutzfeldt-Jakob disease, *Proc Natl Acad Sci U S A 100*, 675-679.
122. Ghidoni, R., Benussi, L., Glionna, M., Franzoni, M., and Binetti, G. (2008) Low plasma progranulin levels predict progranulin mutations in frontotemporal lobar degeneration, *Neurology 71*, 1235-1239.
123. Finch, N., Baker, M., Crook, R., Swanson, K., Kuntz, K., Surtees, R., Bisceglio, G., Rovelet-Lecrux, A., Boeve, B., and Petersen, R. C. (2009) Plasma progranulin levels predict progranulin mutation status in frontotemporal dementia patients and asymptomatic family members, *Brain*, awn352.
124. Coppola, G., Karydas, A., Rademakers, R., Wang, Q., Baker, M., Hutton, M., Miller, B. L., and Geschwind, D. H. (2008) Gene expression study on peripheral blood identifies progranulin mutations, *Annals of neurology 64*, 92-96.
125. Warraich, S. T., Yang, S., Nicholson, G. A., and Blair, I. P. (2010) TDP-43: a DNA and RNA binding protein with roles in neurodegenerative diseases, *The international journal of biochemistry & cell biology 42*, 1606-1609.
126. van der Zee, J., Le Ber, I., Maurer-Stroh, S., Engelborghs, S., Gijselinck, I., Camuzat, A., Brouwers, N., Vandenberghe, R., Sleegers, K., Hannequin, D., Dermaut, B., Schymkowitz, J., Campion, D., Santens, P., Martin, J. J., Lacomblez, L., De Pooter, T., Peeters, K., Mattheijssens, M., Vercelletto, M., Van den Broeck, M., Cruts, M., De Deyn, P. P., Rousseau, F., Brice, A., and Van Broeckhoven, C. (2007) Mutations other than null mutations producing a pathogenic loss of progranulin in frontotemporal dementia, *Hum Mutat 28*, 416.
127. Shankaran, S. S., Capell, A., Hruscha, A. T., Fellerer, K., Neumann, M., Schmid, B., and Haass, C. (2008) Missense mutations in the progranulin gene linked to frontotemporal lobar degeneration with ubiquitin-immunoreactive inclusions reduce progranulin production and secretion, *J Biol Chem 283*, 1744-1753.
128. Laird, A. S., Van Hoecke, A., De Muynck, L., Timmers, M., Van Den Bosch, L., Van Damme, P., and Robberecht, W. (2010) Progranulin is neurotrophic in vivo and protects against a mutant TDP-43 induced axonopathy, *PLoS One 5*, e13368.
129. Martens, L. H., Zhang, J., Barmada, S. J., Zhou, P., Kamiya, S., Sun, B., Min, S.-W., Gan, L., Finkbeiner, S., and Huang, E. J. (2012) Progranulin deficiency promotes neuroinflammation and neuron loss following toxin-induced injury, *The Journal of clinical investigation 122*, 3955-3959.
130. Tompa, P., Szász, C., and Buday, L. (2005) Structural disorder throws new light on moonlighting, *Trends in Biochemical Sciences 30*, 484-489.
131. Hogg, P. J. (2003) Disulfide bonds as switches for protein function, *Trends in Biochemical Sciences 28*, 210-214.
132. Thornton, J. (1981) Disulphide bridges in globular proteins, *Journal of molecular biology 151*, 261-287.

133. Pace, C. N., Grimsley, G., Thomson, J., and Barnett, B. (1988) Conformational stability and activity of ribonuclease T1 with zero, one, and two intact disulfide bonds, *Journal of Biological Chemistry 263*, 11820-11825.
134. Matsumura, M., Becktel, W. J., Levitt, M., and Matthews, B. W. (1989) Stabilization of phage T4 lysozyme by engineered disulfide bonds, *Proceedings of the National Academy of Sciences 86*, 6562-6566.
135. Denton, M. E., and Scheraga, H. A. (1991) Spectroscopic, immunochemical, and thermodynamic properties of carboxymethyl (Cys6, Cys127)-hen egg white lysozyme, *Journal of protein chemistry 10*, 213-232.
136. Taniyama, Y., Ogasahara, K., Yutani, K., and Kikuchi, M. (1992) Folding mechanism of mutant human lysozyme C77/95A with increased secretion efficiency in yeast, *Journal of Biological Chemistry 267*, 4619-4624.
137. HAMAGUCHI, K. (1979) The role of the intrachain disulfide bond in the conformation and stability of the constant fragment of the immunoglobulin light chain, *Journal of biochemistry 86*, 1433-1441.
138. Glockshuber, R., Schmidt, T., and Plueckthun, A. (1992) The disulfide bonds in antibody variable domains: effects on stability, folding in vitro, and functional expression in Escherichia coli, *Biochemistry 31*, 1270-1279.
139. Proba, K., Honegger, A., and Plückthun, A. (1997) A natural antibody missing a cysteine in V H: consequences for thermodynamic stability and folding, *Journal of molecular biology 265*, 161-172.
140. Castellino, F. J., and McCance, S. G. (2007) The Kringle Domains of Human Plasminogen, In *Ciba Foundation Symposium 212 - Plasminogen-Related Growth Factors*, pp 46-65, John Wiley & Sons, Ltd.
141. Speziale, M. V., and Detwiler, T. (1990) Free thiols of platelet thrombospondin. Evidence for disulfide isomerization, *Journal of Biological Chemistry 265*, 17859-17867.
142. Lay, A. J., Jiang, X.-M., Kisker, O., Flynn, E., Underwood, A., Condron, R., and Hogg, P. J. (2000) Phosphoglycerate kinase acts in tumour angiogenesis as a disulphide reductase, *nature 408*, 869-873.
143. Matthias, L. J., Yam, P. T., Jiang, X.-M., Vandegraaff, N., Li, P., Poumbourios, P., Donoghue, N., and Hogg, P. J. (2002) Disulfide exchange in domain 2 of CD4 is required for entry of HIV-1, *Nature immunology 3*, 727-732.
144. Trachootham, D., Lu, W., Ogasawara, M. A., Valle, N. R.-D., and Huang, P. (2008) Redox regulation of cell survival, *Antioxidants & redox signaling 10*, 1343-1374.
145. Romero, P., Obradovic, Z., Li, X., Garner, E. C., Brown, C. J., and Dunker, A. K. (2001) Sequence complexity of disordered protein, *Proteins: Structure, Function, and Bioinformatics 42*, 38-48.
146. Peng, K., Radivojac, P., Vucetic, S., Dunker, A. K., and Obradovic, Z. (2006) Length-dependent prediction of protein intrinsic disorder, *BMC Bioinformatics 7*, 1-17.
147. PENG, K., VUCETIC, S., RADIVOJAC, P., BROWN, C. J., DUNKER, A. K., and OBRADOVIC, Z. (2005) OPTIMIZING LONG INTRINSIC DISORDER

PREDICTORS WITH PROTEIN EVOLUTIONARY INFORMATION, *Journal of Bioinformatics and Computational Biology 03*, 35-60.
148. Xue, B., Dunbrack, R. L., Williams, R. W., Dunker, A. K., and Uversky, V. N. (2010) PONDR-FIT: A meta-predictor of intrinsically disordered amino acids, *Biochimica et Biophysica Acta (BBA) - Proteins and Proteomics 1804*, 996-1010.
149. Holehouse, A. S., Ahad, J., Das, R. K., and Pappu, R. V. (2015) CIDER: Classification of Intrinsically Disordered Ensemble Regions, *Biophysical Journal 108*, 228a.
150. Gasteiger, E., Hoogland, C., Gattiker, A., Duvaud, S. e., Wilkins, M., Appel, R., and Bairoch, A. (2005) Protein Identification and Analysis Tools on the ExPASy Server, In *The Proteomics Protocols Handbook* (Walker, J., Ed.), pp 571-607, Humana Press.
151. Csizmók, V., Szőllősi, E., Friedrich, P., and Tompa, P. (2006) A novel two-dimensional electrophoresis technique for the identification of intrinsically unstructured proteins, *Molecular & Cellular Proteomics 5*, 265-273.
152. Tompa, P., and Fersht, A. (2009) *Structure and Function of Intrinsically Disordered Proteins*, CRC Press.
153. Uversky, V. N., Li, J., and Fink, A. L. (2001) Trimethylamine-N-oxide-induced folding of α-synuclein, *FEBS Letters 509*, 31-35.
154. Boteva, R., Zlateva, T., Dorovska-Taran, V., Visser, A. J., Tsanev, R., and Salvato, B. (1996) Dissociation equilibrium of human recombinant interferon γ, *Biochemistry 35*, 14825-14830.
155. Lakowicz, J. R. (2007) *Principles of fluorescence spectroscopy*, Springer Science & Business Media.
156. Brzovic, Peter S., Heikaus, Clemens C., Kisselev, L., Vernon, R., Herbig, E., Pacheco, D., Warfield, L., Littlefield, P., Baker, D., Klevit, Rachel E., and Hahn, S. (2011) The Acidic Transcription Activator Gcn4 Binds the Mediator Subunit Gal11/Med15 Using a Simple Protein Interface Forming a Fuzzy Complex, *Molecular Cell 44*, 942-953.
157. Fuxreiter, M. (2012) Fuzziness: linking regulation to protein dynamics, *Molecular BioSystems 8*, 168-177.
158. Fuxreiter, M., and Tompa, P. (2012) Fuzzy Complexes: A More Stochastic View of Protein Function, In *Fuzziness* (Fuxreiter, M., and Tompa, P., Eds.), pp 1-14, Springer US.
159. Tompa, P., and Fuxreiter, M. (2008) Fuzzy complexes: polymorphism and structural disorder in protein–protein interactions, *Trends in Biochemical Sciences 33*, 2-8.
160. Libich, D. S., Ahmed, M. A. M., Zhong, L., Bamm, V. V., Ladizhansky, V., and Harauz, G. (2010) Fuzzy complexes of myelin basic protein: NMR spectroscopic investigations of a polymorphic organizational linker of the central nervous system, *Biochemistry and cell biology = Biochimie et biologie cellulaire 88*, 143-155.
161. Baldwin, A. S. (1996) THE NF-κB AND IκB PROTEINS: New Discoveries and Insights, *Annual Review of Immunology 14*, 649-681.

162. Hayden, M. S., and Ghosh, S. (2008) Shared principles in NF-κB signaling, *Cell 132*, 344-362.
163. Verma, I. M., Stevenson, J. K., Schwarz, E. M., Van Antwerp, D., and Miyamoto, S. (1995) Rel/NF-kappa B/I kappa B family: intimate tales of association and dissociation, *Genes & Development 9*, 2723-2735.
164. Fuxreiter, M., and Tompa, P. (2012) *Fuzziness: Structural Disorder in Protein Complexes*, Springer New York.
165. Uversky, V. N. (2013) A decade and a half of protein intrinsic disorder: Biology still waits for physics, *Protein Science : A Publication of the Protein Society 22*, 693-724.
166. Ghag, G., Wolf, L. M., Reed, R. G., Van Der Munnik, N. P., Mundoma, C., Moss, M. A., and Rangachari, V. (2016) Fully reduced granulin-B is intrinsically disordered and displays concentration-dependent dynamics, *Protein Engineering Design and Selection*.
167. Bessette, P. H., Åslund, F., Beckwith, J., and Georgiou, G. (1999) Efficient folding of proteins with multiple disulfide bonds in the Escherichia coli cytoplasm, *Proceedings of the National Academy of Sciences 96*, 13703-13708.
168. André, I., Linse, S., and Mulder, F. A. A. (2007) Residue-Specific pKa Determination of Lysine and Arginine Side Chains by Indirect 15N and 13C NMR Spectroscopy: Application to apo Calmodulin, *Journal of the American Chemical Society 129*, 15805-15813.
169. Poon, D. K. Y., Schubert, M., Au, J., Okon, M., Withers, S. G., and McIntosh, L. P. (2006) Unambiguous Determination of the Ionization State of a Glycoside Hydrolase Active Site Lysine by 1H−15N Heteronuclear Correlation Spectroscopy, *Journal of the American Chemical Society 128*, 15388-15389.
170. Henry, G. D., and Sykes, B. D. (1995) Determination of the rotational dynamics and pH dependence of the hydrogen exchange rates of the arginine guanidino group using NMR spectroscopy, *Journal of Biomolecular NMR 6*, 59-66.
171. Woody, R. W. (1992) Circular dichroism and conformation of unordered polypeptides, *Adv. Biophys. Chem 2*, 37-79.
172. Bovey, F., and Hood, F. (1967) Circular dichroism spectrum of poly-L-proline, *Biopolymers 5*, 325-326.
173. Adzhubei, A. A., Sternberg, M. J. E., and Makarov, A. A. (2013) Polyproline-II Helix in Proteins: Structure and Function, *Journal of Molecular Biology 425*, 2100-2132.
174. Creamer, T. P., and Campbell, M. N. (2002) Determinants of the polyproline II helix from modeling studies, *Advances in protein chemistry 62*, 263-282.
175. Hu, K.-N., Havlin, R. H., Yau, W.-M., and Tycko, R. (2009) Quantitative determination of site-specific conformational distributions in an unfolded protein by solid-state nuclear magnetic resonance, *Journal of molecular biology 392*, 1055-1073.
176. Syme, C. D., Blanch, E. W., Holt, C., Jakes, R., Goedert, M., Hecht, L., and Barron, L. D. (2002) A Raman optical activity study of rheomorphism in caseins, synucleins and tau, *European Journal of Biochemistry 269*, 148-156.

177. Woody, R. W. (2009) Circular dichroism spectrum of peptides in the poly (Pro) II conformation, *Journal of the American Chemical Society 131*, 8234-8245.
178. Stryer, L. (1965) The interaction of a naphthalene dye with apomyoglobin and apohemoglobin, *Journal of Molecular Biology 13*, 482-495.
179. Semisotnov, G., Rodionova, N., Razgulyaev, O., Uversky, V., Gripas, A., and Gilmanshin, R. (1991) Study of the "molten globule" intermediate state in protein folding by a hydrophobic fluorescent probe, *Biopolymers 31*, 119-128.
180. Reynolds, J. A., and Tanford, C. (1970) The gross conformation of protein-sodium dodecyl sulfate complexes, *Journal of Biological Chemistry 245*, 5161-5165.
181. Mattice, W. L., Riser, J. M., and Clark, D. S. (1976) Conformational properties of the complexes formed by proteins and sodium dodecyl sulfate, *Biochemistry 15*, 4264-4272.
182. Montserret, R., McLeish, M. J., Böckmann, A., Geourjon, C., and Penin, F. (2000) Involvement of electrostatic interactions in the mechanism of peptide folding induced by sodium dodecyl sulfate binding, *Biochemistry 39*, 8362-8373.
183. Moore, B. D., Rangachari, V., Tay, W. M., Milkovic, N. M., and Rosenberry, T. L. (2009) Biophysical Analyses of Synthetic Amyloid-β (1− 42) Aggregates before and after Covalent Cross-Linking. Implications for Deducing the Structure of Endogenous Amyloid-β Oligomers, *Biochemistry 48*, 11796-11806.
184. Otzen, D. E., and Oliveberg, M. (2002) Burst-phase expansion of native protein prior to global unfolding in SDS, *Journal of molecular biology 315*, 1231-1240.
185. Wang, J., Van Damme, P., Cruchaga, C., Gitcho, M. A., Vidal, J. M., Seijo-Martínez, M., Wang, L., Wu, J. Y., Robberecht, W., and Goate, A. (2010) Pathogenic cysteine mutations affect progranulin function and production of mature granulins, *Journal of neurochemistry 112*, 1305-1315.
186. Zhang, Y. (2008) I-TASSER server for protein 3D structure prediction, *BMC Bioinformatics 9*, 40.
187. Roy, A., Kucukural, A., and Zhang, Y. (2010) I-TASSER: a unified platform for automated protein structure and function prediction, *Nature protocols 5*, 725-738.
188. Montelione, G. T., Winkler, M. E., Burton, L. E., Rinderknecht, E., Sporn, M. B., and Wagner, G. (1989) Sequence-specific 1H-NMR assignments and identification of two small antiparallel beta-sheets in the solution structure of recombinant human transforming growth factor alpha, *Proceedings of the National Academy of Sciences 86*, 1519-1523.
189. Huang, H.-W., Mohan, S. K., and Yu, C. (2010) The NMR solution structure of human epidermal growth factor (hEGF) at physiological pH and its interactions with suramin, *Biochemical and Biophysical Research Communications 402*, 705-710.
190. Levine, H. (1993) Thioflavine T interaction with synthetic Alzheimer's disease β-amyloid peptides: Detection of amyloid aggregation in solution, *Protein Science 2*, 404-410.
191. Bitan, G., Lomakin, A., and Teplow, D. B. (2001) Amyloid β-Protein oligomerization prenucleation interactions revealed by photo-induced cross-

linking of unmodified proteins, *Journal of Biological Chemistry 276*, 35176-35184.
192. Lambert, M. P., Barlow, A., Chromy, B. A., Edwards, C., Freed, R., Liosatos, M., Morgan, T., Rozovsky, I., Trommer, B., and Viola, K. L. (1998) Diffusible, nonfibrillar ligands derived from Aβ1–42 are potent central nervous system neurotoxins, *Proceedings of the National Academy of Sciences 95*, 6448-6453.
193. Huang, T. J., Yang, D.-S., Fraser, P. E., and Chakrabartty, A. (2000) Alternate Aggregation Pathways of the Alzheimer β-Amyloid Peptide AN IN VITRO MODEL OF PREAMYLOID, *Journal of Biological Chemistry 275*, 36436-36440.
194. Jahn, T. R., and Radford, S. E. (2008) Folding versus aggregation: polypeptide conformations on competing pathways, *Archives of biochemistry and biophysics 469*, 100-117.
195. Gorman, P. M., Yip, C. M., Fraser, P. E., and Chakrabartty, A. (2003) Alternate aggregation pathways of the Alzheimer β-amyloid peptide: Aβ association kinetics at endosomal pH, *Journal of molecular biology 325*, 743-757.
196. Goldsbury, C., Frey, P., Olivieri, V., Aebi, U., and Müller, S. A. (2005) Multiple assembly pathways underlie amyloid-β fibril polymorphisms, *Journal of molecular biology 352*, 282-298.
197. Demeler, B. (2005) UltraScan: a comprehensive data analysis software package for analytical ultracentrifugation experiments, *Modern analytical ultracentrifugation: techniques and methods*, 210-229.
198. Schuck, P., and Demeler, B. (1999) Direct Sedimentation Analysis of Interference Optical Data in Analytical Ultracentrifugation, *Biophysical Journal 76*, 2288-2296.
199. Van Holde, K., and Weischet, W. O. (1978) Boundary analysis of sedimentation-velocity experiments with monodisperse and paucidisperse solutes, *Biopolymers 17*, 1387-1403.
200. Durchschlag, H. (1986) Specific Volumes of Biological Macromolecules and Some Other Molecules of Biological Interest, In *Thermodynamic Data for Biochemistry and Biotechnology* (Hinz, H.-J., Ed.), pp 45-128, Springer Berlin Heidelberg.
201. Schanda, P., and Brutscher, B. (2005) Very Fast Two-Dimensional NMR Spectroscopy for Real-Time Investigation of Dynamic Events in Proteins on the Time Scale of Seconds, *Journal of the American Chemical Society 127*, 8014-8015.
202. Abràmoff, M. D., Magalhães, P. J., and Ram, S. J. (2004) Image processing with ImageJ, *Biophotonics international 11*, 36-43.
203. Schneider, C. A., Rasband, W. S., and Eliceiri, K. W. (2012) NIH Image to ImageJ: 25 years of image analysis, *Nat Meth 9*, 671-675.